

# **Search for massive neutrinos in $\pi^+ \rightarrow e^+ \nu$ decay**

**Kaoru Yamada**

Department of Physics, Osaka University

February, 2010



## Abstract

Recently our understanding of neutrino physics was greatly developed with many experimental results. We know now that neutrinos have masses though they are really small. However then some question is worth asking. Why do they have such a small mass compared to other particles? Why are there no right-handed neutrinos?

Existence of massive neutrinos have possibility to answer these questions. However there are no evidence of massive neutrinos in any experiments up to now.

In this thesis, massive neutrinos search in  $\pi^+ \rightarrow e^+\nu$  decay is done in the PIENU experiment at the 500 MeV proton cyclotron in TRIUMF. We analyzed first physics data which were taken from May, 2009 to September, 2009. No evidence of massive neutrinos were observed and the upper limits of mixing parameter of massive neutrinos  $|U_{ei}|^2$  is evaluated in the mass region 90 MeV  $\sim$  130 MeV. The upper limits (90% C.L.) is about  $5 \times 10^{-7}$  and the result is about 1.5 time better than current experimental limit.



# Contents

<b>1</b>	<b>Introduction</b>	<b>1</b>
1.1	Neutrinos and their masses . . . . .	1
1.2	Massive neutrinos in $\pi^+ \rightarrow e^+\nu$ decay . . . . .	2
1.3	Outline of this thesis . . . . .	3
<b>2</b>	<b>The PIENU experiment</b>	<b>7</b>
2.1	Motivation of the PIENU experiment . . . . .	7
2.2	Experimental method for massive neutrino search in $\pi^+ \rightarrow e^+\nu$ decay . . . . .	7
2.3	Requirement of the experiment . . . . .	11
2.4	Design of the PIENU detector . . . . .	12
2.5	Monte Carlo study with the detector . . . . .	12
2.5.1	$\pi^+ \rightarrow \mu^+ \rightarrow e^+$ muon-decay-at-rest event ( $\mu$ DAR) . . . . .	13
2.5.2	$\pi^+ \rightarrow \mu^+ \rightarrow e^+$ muon-decay-in-flight event ( $\mu$ DIF) . . . . .	16
2.5.3	Low energy tail of $\pi^+ \rightarrow e^+\nu_e$ event . . . . .	16
2.5.4	Summary of Monte Carlo study . . . . .	16
2.6	History and future plan of the experiment . . . . .	18
<b>3</b>	<b>Description of the experiment</b>	<b>19</b>
3.1	Beamline . . . . .	19
3.2	Detector . . . . .	22
3.2.1	Overview of the detector . . . . .	22
3.2.2	Plastic scintillators . . . . .	23
3.2.3	Beam wire chambers (WC1&WC2) . . . . .	23
3.2.4	Wire Chamber 3 . . . . .	23
3.2.5	Silicon strip detectors . . . . .	26
3.2.6	NaI calorimeter . . . . .	27
3.2.7	CsI ring calorimeter . . . . .	27
3.2.8	Whole detector assembly . . . . .	28
3.3	Trigger diagram . . . . .	34
3.4	Data acquisition system . . . . .	35
3.4.1	Electronics . . . . .	35
3.4.2	Data acquisition system . . . . .	37
3.5	Variable extraction from the waveform . . . . .	37
3.5.1	COPPER 500-MHz FADC . . . . .	37
3.5.2	60-MHz FADC (VF48) . . . . .	39

<b>4</b>	<b>Pion decay event selection</b>	<b>41</b>
4.1	Data set for analysis and overview of the pion decay event section . . . . .	41
4.1.1	Data set for analysis . . . . .	41
4.1.2	Overview of the event selection . . . . .	41
4.2	Energy Calibration . . . . .	41
4.2.1	Scintillating counters . . . . .	41
4.2.2	NaI calorimeter . . . . .	42
4.2.3	Silicon detector . . . . .	42
4.2.4	Gain stability correction . . . . .	42
4.3	Pileup rejection . . . . .	44
4.3.1	Number of hit . . . . .	44
4.3.2	Charge ratio of narrow and wide time window . . . . .	44
4.3.3	Timing consistency of the detector . . . . .	44
4.3.4	Summary of pileup rejection . . . . .	45
4.4	Pre-pileup rejection . . . . .	46
4.5	Pion selection . . . . .	49
4.5.1	Energy deposit and time of flight . . . . .	49
4.5.2	Proton rejection . . . . .	49
4.5.3	Beam profile selection . . . . .	51
4.5.4	Summary of pion selection . . . . .	51
4.6	Summary of pion decay event selection . . . . .	51
<b>5</b>	<b><math>\pi^+ \rightarrow e^+ \nu</math> event selection</b>	<b>55</b>
5.1	Purpose of this section . . . . .	55
5.2	Tracking cut . . . . .	58
5.2.1	Incident angle cut . . . . .	58
5.2.2	Vertex cut . . . . .	58
5.3	Pulse shape cut . . . . .	60
5.3.1	Pulse fitting . . . . .	60
5.3.2	Likelihood definition for pulse shape cut . . . . .	63
5.3.3	Suppression capability to the pion decay at rest event . . . . .	63
5.3.4	Pulse shape cut after Total-Energy-Cut . . . . .	63
5.4	Cut optimization . . . . .	67
5.4.1	Total energy cut . . . . .	68
5.4.2	Tracking cut . . . . .	69
5.4.3	Rmin cut . . . . .	70
5.4.4	Zmin cut . . . . .	71
5.4.5	Pulse shape cut . . . . .	72
5.4.6	Summary of cut optimization . . . . .	73
5.4.7	Fiducial cut on WC3 . . . . .	74
5.5	Summary of $\pi^+ \rightarrow e^+ \nu$ decay selection . . . . .	75
<b>6</b>	<b>Spectrum fitting for massive neutrino search</b>	<b>77</b>
6.1	Component of the spectrum . . . . .	77
6.1.1	Positron energy spectrum shape of $\pi^+ \rightarrow \mu^+ \rightarrow e^+$ muon decay-at-rest ( $\mu$ DAR) . . . . .	77
6.1.2	Positron energy spectrum shape of $\pi^+ \rightarrow \mu^+ \rightarrow e^+$ muon decays-in-flight . . . . .	78

6.1.3	Positron energy spectrum shape of low energy tail of $\pi^+ \rightarrow e^+\nu_e$ decay . . . .	78
6.1.4	Positron energy spectrum shape of $\pi^+ \rightarrow e^+\nu_i$ decay . . . . .	80
6.2	Spectrum fitting . . . . .	87
6.2.1	Subtraction of $\pi^+ \rightarrow \mu^+ \rightarrow e^+$ muon decays-at-rest event ( $\mu$ DAR) . . . . .	87
6.2.2	Spectrum Fitting . . . . .	91
6.2.3	Raw upper limit estimation . . . . .	95
<b>7</b>	<b>Systematic corrections</b>	<b>97</b>
7.1	Subtracted $\mu$ DAR amplitude . . . . .	97
7.2	Purity of $\pi^+ \rightarrow e^+\nu_e$ decay . . . . .	97
7.3	Acceptance correction . . . . .	99
7.3.1	Summary of the cuts . . . . .	99
7.3.2	Monte Carlo estimation . . . . .	99
7.3.3	Validity of the Monte Carlo . . . . .	103
7.3.4	Summary of acceptance correction . . . . .	103
7.4	Upper limit estimation . . . . .	107
<b>8</b>	<b>Discussions</b>	<b>109</b>
<b>9</b>	<b>Conclusion</b>	<b>113</b>



# List of Figures

1.1	Tree diagram of $\pi^+ \rightarrow l^+ \nu_l$ decay . . . . .	2
1.2	Bound on $ U_{ei} ^2$ versus $m_i$ in the mass range 10 eV- 10 MeV . . . . .	4
1.3	Bound on $ U_{ei} ^2$ versus $m_i$ in the mass range 10 MeV- 100 GeV . . . . .	5
2.1	Basic detector concept . . . . .	8
2.2	Positron energy spectrum of two decay modes (MC) . . . . .	9
2.3	Decay time and Total-Energy of two decay modes . . . . .	10
2.4	Positron energy spectrum after Timing-Cut and Total-Energy-Cut (MC) . . . . .	10
2.5	Total-Energy spectrum in log scale after Timing-Cut (MC) . . . . .	11
2.6	Schematic view of the PIENU detector . . . . .	12
2.7	Schematic view of track of pion decay . . . . .	14
2.8	Total-Energy distribution(MC) . . . . .	14
2.9	Incident angle distribution after Total-Energy-Cut (MC) . . . . .	15
2.10	Vertex reconstruction information after Total-Energy-Cut and Incident-Angle-Cut (MC) . . . . .	15
2.11	Information of $\pi^+ \rightarrow \mu^+ \rightarrow e^+$ muon-decay-in-flight event . . . . .	17
2.12	Positron energy spectrum w/ and w/o CsI of $\pi^+ \rightarrow e^+ \nu_e$ decay . . . . .	18
3.1	Schematic view of M13 beam channel . . . . .	19
3.2	Beam profile at F3 . . . . .	20
3.3	Energy deposit and profile of the beam particle . . . . .	20
3.4	Picture of M13 beam channel . . . . .	21
3.5	Schematic view of the PIENU detector . . . . .	22
3.6	Picture of beam wire chamber . . . . .	24
3.7	Picture of wire chamber 3 mounted onto the flange of the NaI crystal enclosure . . . . .	25
3.8	Schematic of the silicon strip readout scheme . . . . .	26
3.9	Picture of the silicon strip detector . . . . .	27
3.10	Picture of the NaI calorimeter . . . . .	27
3.11	Picture of the CsI calorimeter . . . . .	29
3.12	CAD design of the PIENU detector . . . . .	30
3.13	Picture of the detector assembly 1 . . . . .	31
3.14	Picture of the detector assembly 2 . . . . .	32
3.15	Picture of M13 beam channel after detector installation . . . . .	33
3.16	Simplified trigger diagram . . . . .	35
3.17	Picture of the COPPER board and 500-MHz FADC daughter card . . . . .	36
3.18	Waveform data taken by the COPPER 500-MHz FADC system . . . . .	36
3.19	Web interface of the DAQ system . . . . .	38

3.20	Variable extraction from 500-MHz waveform . . . . .	38
3.21	Variable extraction from 500-MHz waveform . . . . .	39
4.1	Integrated charge of the scintillating counters with beam positron . . . . .	42
4.2	Integrated charge of the NaI calorimeter with beam positron . . . . .	43
4.3	Integrated charge of the silicon strip detector with beam positron . . . . .	43
4.4	Gain stability correction . . . . .	44
4.5	Number of hit in scintillating counters in the beam time window . . . . .	45
4.6	Charge ratio of narrow and wide time window in scintillating counters . . . . .	46
4.7	Timing difference between the hits in each PMTs of the scintillating counters . . . . .	47
4.8	Timing difference between the hits in each scintillating counter . . . . .	47
4.9	Time spectrum with pileup rejection . . . . .	48
4.10	Number of hit in B1 and T1 in the time window from $-6.5 \mu\text{s}$ to $-2.2 \mu\text{s}$ with respect to the triggered beam timing . . . . .	48
4.11	Time spectrum with pre-pileup rejection . . . . .	49
4.12	Energy deposit in B1 & B2 and TOF . . . . .	50
4.13	Energy deposit in the NaI calorimeter vs minimum energy deposit in downstream detectors . . . . .	51
4.14	Beam profile at WC1 . . . . .	52
4.15	Time spectrum with pion selection cuts . . . . .	52
4.16	Time spectrum with pion decay selection . . . . .	53
4.17	Time spectrum with and without pre-scale correction . . . . .	54
5.1	Positron energy and Total Energy in early time window . . . . .	56
5.2	Time spectrum of $\pi^+ \rightarrow e^+ \nu_e$ and $\pi \rightarrow \mu \rightarrow e$ . . . . .	56
5.3	Positron energy spectrum with Total-Energy-Cut . . . . .	56
5.4	Total-Energy spectrum and Positron energy spectrum with Total-Energy-Cut with the full data set . . . . .	58
5.5	Angle of the incoming particle to the target . . . . .	59
5.6	Decay vertex information from tracking . . . . .	60
5.7	Waveform of the target PMT . . . . .	61
5.8	Waveform template for the pulse fitting . . . . .	62
5.9	Variables extracted by pulse fitting . . . . .	64
5.10	Probability density functions of the variables which are extracted from pulse fitting . . . . .	65
5.11	Capability of PS-Cut to suppress $\pi^+ \rightarrow \mu^+ \rightarrow e^+$ DAR events . . . . .	66
5.12	Pulse-Shape-Likelihood distribution . . . . .	67
5.13	Optimization of Total-Energy-Cut . . . . .	68
5.14	Optimization of Incident-Angle-Cut . . . . .	69
5.15	Optimization of Rmin-Cut . . . . .	70
5.16	Optimization of Zmin-Cut . . . . .	71
5.17	Optimization of PS-Cut . . . . .	72
5.18	Positron energy spectrum with the suppression cuts . . . . .	73
5.19	Fiducial cut on WC3 . . . . .	74
5.20	Positron energy spectrum after background suppression for neutrino search. . . . .	75
6.1	Positron energy spectrum of $\pi^+ \rightarrow \mu^+ \rightarrow e^+$ muon decays-at-rest event . . . . .	78
6.2	Positron energy spectrum of $\pi^+ \rightarrow \mu^+ \rightarrow e^+$ muon decays-in-flight event . . . . .	79

6.3	Energy spectrum of 75 MeV/c beam positron . . . . .	79
6.4	Detector setup for beam positron data . . . . .	81
6.5	Positron energy distribution at different momenta . . . . .	82
6.6	Positron energy resolution as a function of energy . . . . .	83
6.7	Positron energy spectrum of $\pi^+ \rightarrow e^+ \nu_e$ decay . . . . .	83
6.8	Energy spectra of beam positrons with different momenta at $0^\circ$ . . . . .	84
6.9	Energy spectra of beam positrons with different momenta at $45^\circ$ . . . . .	85
6.10	Energy spectrum of the positrons with a random momentum direction (Signal MC). . . . .	86
6.11	Pulse-Shape-Likelihood distribution . . . . .	87
6.12	Time spectrum of events which have less than 52MeV in Suppressed-Spectrum . . . . .	89
6.13	Suppressed spectrum before and after $\mu$ DAR background subtraction . . . . .	90
6.14	Positron energy spectra with 5MeV step which are fitted with just an exponential function . . . . .	92
6.15	Positron energy spectra with 5MeV step which are fitted with $f_{exp+bump}(x)$ . . . . .	93
6.16	$\chi^2$ and probability of the spectrum fitting . . . . .	94
6.17	Bump amplitude from the spectrum fitting. . . . .	94
6.18	The Gaussian function to obtain an upper limit from the fitting result by the Bayes's method . . . . .	95
6.19	Raw upper limits (90% C.L.) of the branching ratio $\Gamma(\pi \rightarrow e \nu_i)/\Gamma(\pi \rightarrow e \nu_e)$ . . . . .	96
7.1	Raw upper limits (90% C.L.) of $\Gamma(\pi \rightarrow e \nu_i)\Gamma(\pi \rightarrow e \nu_e)$ by changing the subtracted $\mu$ DAR amplitude . . . . .	98
7.2	Time spectrum of the events which have more than 52 MeV in Suppressed-spectrum . . . . .	98
7.3	Relative acceptance of Fiducial-Cut compared to 70 MeV positron as a function of the positron energy . . . . .	100
7.4	Relative acceptance of CsI-Veto-Cut and Fiducial-Cut compared to 70 MeV positron as a function of the positron energy . . . . .	101
7.5	Acceptance with Total-Energy-Cut as a function of positron energy . . . . .	101
7.6	Acceptance with Rmin-Cut as a function of positron energy . . . . .	102
7.7	Acceptance with Zmin-Cut as a function of positron energy . . . . .	103
7.8	Acceptance study of the cuts with positrons from $\pi^+ \rightarrow \mu^+ \rightarrow e^+$ (DATA) . . . . .	104
7.9	Acceptance study of the cuts with positrons from $\pi^+ \rightarrow \mu^+ \rightarrow e^+$ (MC) . . . . .	105
7.10	Acceptance with the cuts as a function of positron energy . . . . .	106
7.11	Upper limit (90% C.L.) of the branching ratio $\Gamma(\pi \rightarrow e \nu_i)/\Gamma(\pi \rightarrow e \nu_e)$ . . . . .	107
7.12	Upper limit (90% C.L.) of the mixing parameter $ U_{ei} ^2$ . . . . .	108
8.1	Upper limit (90% C.L.) of the mixing parameter $ U_{ei} ^2$ . . . . .	110
8.2	Upper limit (90% C.L.) of the mixing parameter $ U_{ei} ^2$ . . . . .	111



# List of Tables

1.1	Summary of current upper limit on each neutrino mass . . . . .	1
2.1	History and future plan of the PIENU experiment . . . . .	18
3.1	Sizes of the schilling counters . . . . .	23
3.2	Rate of each trigger . . . . .	34
4.1	Summary of pileup cut . . . . .	45
4.2	Summary of pre-pileup cut . . . . .	46
4.3	Summary of pion selection cut . . . . .	51
4.4	Summary of pion decay event selection . . . . .	53
5.1	Summary of the cuts before $\pi^+ \rightarrow e^+ \nu$ event selection . . . . .	57
5.2	Summary of Suppression-Cut . . . . .	73
5.3	Summary of positron energy spectrum after background suppression . . . . .	75
7.1	Summary of the cuts . . . . .	99



# Chapter 1

## Introduction

### 1.1 Neutrinos and their masses

In 1930, W. Paul postulated the existence of neutrino to explain the observed continuous electron energy spectrum from nuclear  $\beta$ -decay.[1] In his hypothesis, a neutrino was required to be a neutral particle with spin 1/2 and a very tiny mass. The first experimental evidence of a neutrino induced interaction was found in search for the inverse  $\beta$ -decay,  $\nu_e p \rightarrow e^+ n$ [2]. Muon neutrino and tau neutrino were found in 1962 and in 1975 respectively [3] [4].

In the standard model, neutrinos are assumed to be massless leptons and the number of types of neutrinos is three ( $\nu_e, \nu_\mu, \nu_\tau$ ). There is also strong experimental constraints that the number of types of neutrino whose mass is less than 45 GeV should be three from the result of the LEP experiment [5]. However neutrinos do not need to be massless in the standard model. If neutrinos have finite masses, they can be represented in the masses eigenstate ( $\nu_1, \nu_2, \nu_3$ ) as well as in the flavor eigenstate as described below.

$$\nu_l = \sum_{i=1}^3 U_{li} \nu_i \quad (1.1)$$

$$l = e, \mu, \tau \quad (1.2)$$

Up to now, in spite of a number of experimental efforts to measure the masses of neutrino directly using decay kinematics of parent particles, no experiment has found a finite mass over the experimental errors. The upper limits on neutrino masses are summarized in Table 1.1.

Flavor of Neutrino	Experimental Technique	Upper Limit
$\nu_e$	${}^3_1\text{H}$ $\beta$ -decay kinematics	3 eV(95% C.L.)
$\nu_\mu$	$\pi$ decay kinematics	170 keV(95% C.L.)
$\nu_\tau$	$\tau$ decay kinematics	18.2 MeV(95% C.L.)

Table 1.1: Summary of current upper limit of neutrino masses. The values are evaluated by Particle Data Group[6].

Nevertheless, there is another way to know about neutrino masses. It is measurements of neutrino oscillation. Neutrino oscillation can occur only if neutrinos have masses. The difference of two mass

eigenstates,  $\Delta m_{ij}^2 = m_i^2 - m_j^2$ , can be obtained from the oscillation parameters. The latest experimental result is shown below.

- $1.4 \times 10^{-3} < \Delta m_{13}^2 < 3.3 \times 10^{-3}$ [7]
- $7.1 \times 10^{-5} < \Delta m_{12}^2 < 8.9 \times 10^{-5}$ [7]

From these results, we now know that neutrinos have finite masses. Then several questions are worth asking. Why are neutrino masses so small compared to other fermions? Why are there no right handed neutrinos? The "see-saw" mechanism is one of the theory which can answer these questions. In the see-saw mechanism, neutrinos are supposed as Majorana type particle and the right-handed neutrinos are quite heavy. And the heavy right-handed neutrino mass can introduce tiny masses of left-handed neutrinos through the equation below.

$$m_\nu \approx \frac{m_D^2}{M_R} \quad (1.3)$$

$m_D$  is typical Dirac mass and  $M_R$  is mass of the right-handed heavy neutrino. That is why a number of experiments is carried out to find massive neutrinos.

## 1.2 Massive neutrinos in $\pi^+ \rightarrow e^+ \nu$ decay

Tree diagram of charged pion decay  $\pi^+ \rightarrow l^+ \nu_l$  ( $l : e, \mu$ ) is shown in Fig.1.1.

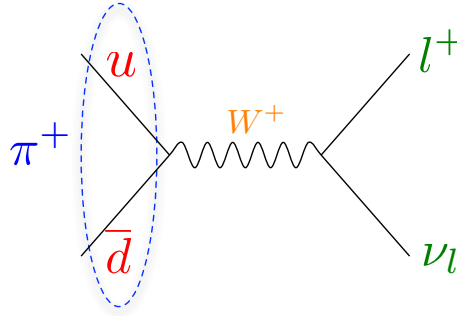


Figure 1.1: Tree diagram of  $\pi^+ \rightarrow l^+ \nu_l$  decay.

Pions decay to a charged lepton and a neutrino via W boson. Most pions decay to muon and a small fraction of pions decay to positron due to helicity suppression. The calculated value of the branching ratio  $R = \Gamma(\pi^+ \rightarrow e^+ \nu_e [\gamma]) / \Gamma(\pi^+ \rightarrow \mu^+ \nu_\mu [\gamma])$  is  $(1.2352 \pm 0.0001) \times 10^{-4}$ [10]. The decays are two body decay and therefore the neutrino mass and the kinematic energy of the charged lepton have the relation below.

$$m_\nu = \sqrt{m_\pi^2 + m_l^2 - 2m_\pi E_l} \quad (1.4)$$

If there are some massive neutrinos, it should also mix with the flavor eigenstates following the equation below.

$$\nu_l = \sum_{i=1}^{3+k} U_{li} \nu_i \quad (1.5)$$

Therefore the measurement of the kinematic energy of the charged lepton from the pion decay has sensitivity to massive neutrinos. From the kinematics,  $\pi^+ \rightarrow e^+\nu$  decay has a sensitivity to the massive neutrinos in the mass region from 0 MeV to 130 MeV and  $\pi^+ \rightarrow \mu^+\nu$  decay has a sensitivity to the massive neutrinos in the mass region from 0 MeV to 34 MeV neutrinos. In this thesis a search for massive neutrino in  $\pi^+ \rightarrow e^+\nu$  decay is done. The massive neutrino search in  $\pi^+ \rightarrow e^+\nu$  decay is done as measurement of the branching ratio  $\Gamma(\pi \rightarrow e\nu_i)/\Gamma(\pi \rightarrow e\nu_e)$ . The branching ratio has the following relation with mixing parameter where  $\rho_e$  is a kinematic factor.

$$\frac{\Gamma(\pi \rightarrow e\nu_i)}{\Gamma(\pi \rightarrow e\nu_e)} = |U_{ei}|^2 \rho_e \quad (1.6)$$

$$\rho_e = \frac{\sqrt{1 + \delta_e^2 + \delta_i^2 - 2(\delta_e + \delta_i + \delta_e\delta_i)(\delta_e + \delta_i - (\delta_e - \delta_i)^2)}}{\delta_e(1 - \delta_i)^2} \quad (1.7)$$

$$\delta_e = \frac{m_e^2}{m_\pi^2} \quad (1.8)$$

$$\delta_i = \frac{m_{\nu_i}^2}{m_\pi^2} \quad (1.9)$$

Up to now massive neutrinos has not found in this decay mode and also not in any other experiments which have sensitivity to other mass regions. The current laboratory experimental limit for the massive neutrinos which have mixing with  $\nu_e$  is shown in Fig.1.2 and Fig.1.3.[8] Fig.1.2 shows the mass range 10 eV- 10 MeV. Fig.1.3 shows the mass range 10 MeV- 100 GeV. The previous experimental result of the kinematic energy measurement of the positron from  $\pi^+ \rightarrow e^+\nu$  decay [13] is shown as a black line in Fig.1.3 is the 100 MeV region. In this region, the search in  $\pi^+ \rightarrow e^+\nu$  decay has good sensitivity after neutrino less double  $\beta$ -decay ( $0\nu\beta\beta$ ) experiment although  $0\nu\beta\beta$  is sensitive only to Majorana neutrinos. Actually, in this energy region from 10 eV - 100 GeV is not enough heavy to explain the mass of normal left-handed neutrinos with the equation (1.3). However some theory beyond the standard model expects massive neutrinos in this energy region.[7][9].

### 1.3 Outline of this thesis

The PIENU experiment is carried out at TRIUMF (Canada's National Laboratory for Particle and Nuclear Physics) from April 2009 to search massive neutrinos in  $\pi^+ \rightarrow e^+\nu$  decay and to measure the branching ratio of the charged pion decay  $R = \Gamma(\pi^+ \rightarrow e^+\nu_e[\gamma])/\Gamma(\pi^+ \rightarrow \mu^+\nu_\mu[\gamma])$ .

The experiment has just begun and the first physics data which is taken from May, 2009 to September, 2009 are analyzed to search massive neutrinos in this thesis.

First of all, basic method of the measurement and an overview of the PIENU experiment is described in Chapter 2. Then, the experimental components are explained in Chapter 3. Analysis to obtain positron energy spectrum of  $\pi^+ \rightarrow e^+\nu$  decay is described in Chapter 4 and Chapter 5. In Chapter 6, the spectrum fitting for neutrino search is done and some systematic correction to the fitting result is done in Chapter 7. Finally, the discussion and the future prospects are given in Chapter 8 and the conclusion of this thesis are mentioned in Chapter 9.

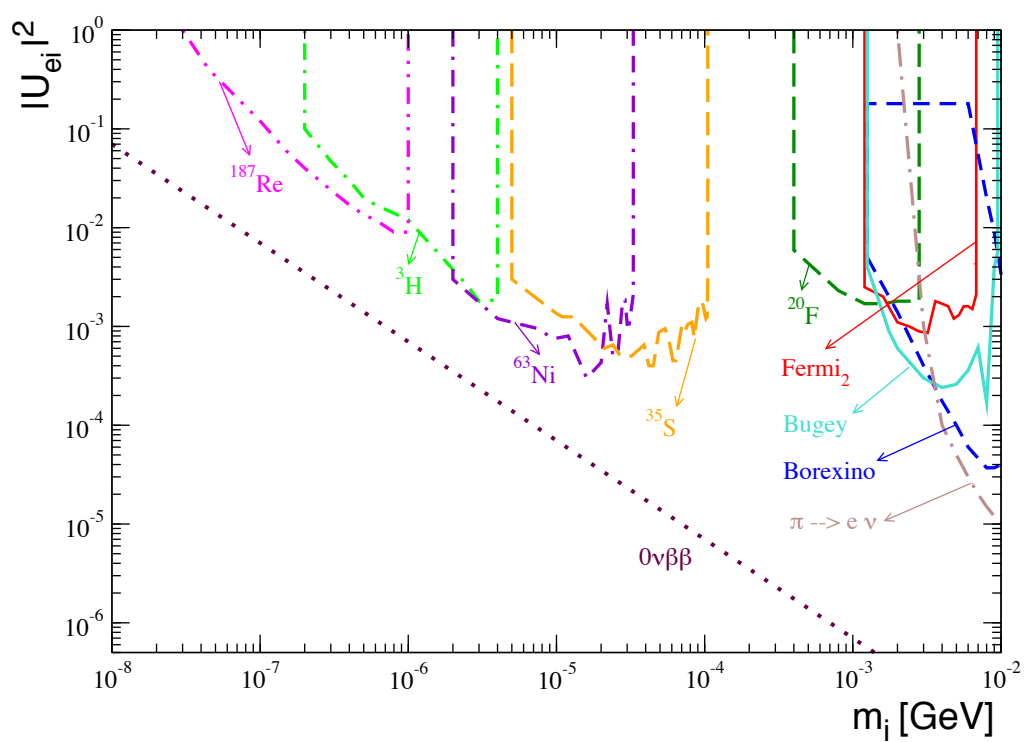


Figure 1.2: Bound on  $|U_{ei}|^2$  versus  $m_i$  in the mass range 10 eV- 10 MeV.

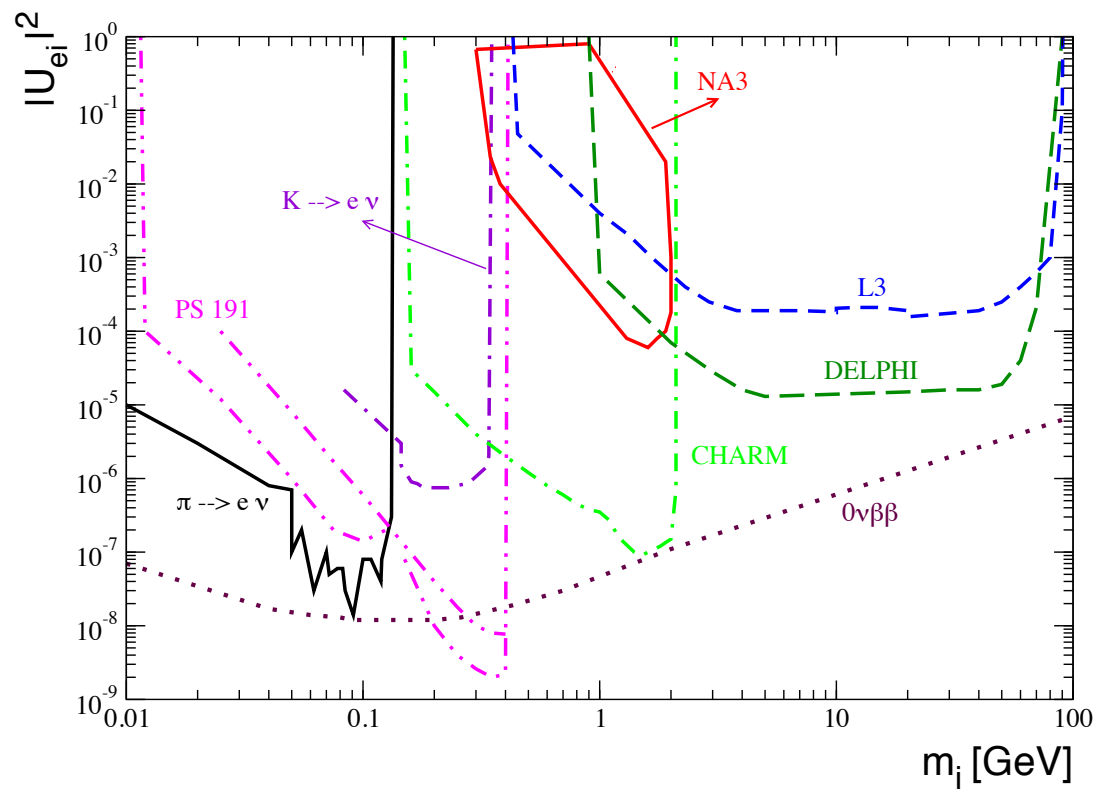


Figure 1.3: Bound on  $|U_{ei}|^2$  versus  $m_i$  in the mass range 10 MeV- 100 GeV.



## Chapter 2

# The PIENU experiment

The PIENU experiment started taking at TRIUMF from April, 2009. It aims to measure the branching ratio of the charged pion decay  $R = \Gamma(\pi^+ \rightarrow e^+\nu_e[\gamma])/\Gamma(\pi^+ \rightarrow \mu^+\nu_\mu[\gamma])$ . A search for massive neutrinos in  $\pi^+ \rightarrow e^+\nu$  decay is also performed. This chapter presents an overview of the PIENU experiment and the experimental method for massive neutrino search.

### 2.1 Motivation of the PIENU experiment

**Branching ratio measurement** The branching ratio of charged pion decay  $R = \Gamma(\pi^+ \rightarrow e^+\nu_e[\gamma])/\Gamma(\pi^+ \rightarrow \mu^+\nu_\mu[\gamma])$  is one of the most precisely calculated value in the standard model. The latest standard model prediction is  $(1.2352 \pm 0.0001) \times 10^{-4}$ [10]. Some new physic beyond the standard model expect deviation of the branching ratio at the same level than the accuracy of the standard mode prediction. However, the most precise experimental result is  $(1.230 \pm 0.004) \times 10^{-4}$ . [11][12] The precision of the measurement is 40 times worse than the standard model prediction. Therefore measurement with a comparable accuracy than the standard model may indicate new physics. The PIENU experiment aims to measure the branching ratio within 0.1% accuracy.

**Massive neutrino search** The  $\pi^+ \rightarrow e^+\nu$  decay is a 2-body decay and therefore the neutrino mass can be known form the positron energy. The motivation of massive neutrino search is described in § 1.1. The experimental result of massive neutrino search in  $\pi^+ \rightarrow e^+\nu$  decay is at  $10^{-2} \sim 10^{-3}$  level.[13]. The PIENU experiment aim to search massive neutrinos with about 10 times better sensitivity. This thesis describe about the massive neutrino search.

### 2.2 Experimental method for massive neutrino search in $\pi^+ \rightarrow e^+\nu$ decay

$\pi^+ \rightarrow e^+\nu$  decay is a two body decay. The neutrino mass and the decay positron energy have therefore the relation below:

$$m_\nu = \sqrt{m_\pi^2 + m_e^2 - 2m_\pi E_e} \quad (2.1)$$

Therefore a measurement of the positron energy from  $\pi^+ \rightarrow e^+\nu$  decay corresponds to measurement of the neutrino mass. From the latest  $\beta$  decay experimental result, the mass of  $\nu_e$  is less than 2.3 eV[14],

and the positron energy is 69.3 MeV. Thus existence of positron which has lower energy than 69.8 MeV indicates existence of a massive neutrino.

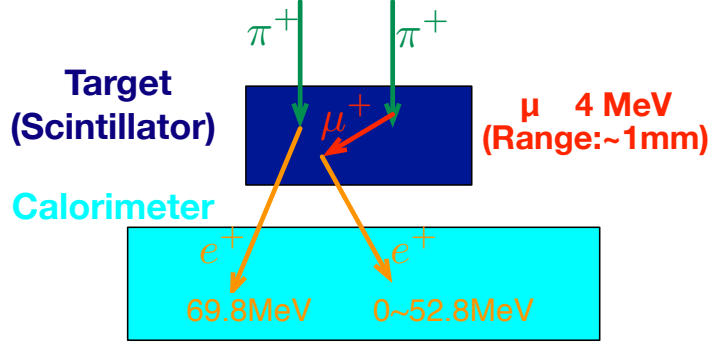


Figure 2.1: Basic detector concept

Fig.2.1 shows the basic detector concept for the  $\pi^+ \rightarrow e^+\nu$  decay measurement. Pions stop in the active target scintillator and decay to positrons. Decay positron energy is measured by a calorimeter. Pions also decay to muons which stop immediately in the target because its kinematic energy is 4.1 MeV and the range in plastic scintillator is about 1.3 mm. Hence the muons subsequently decay to positron and neutrino ( $\mu^+ \rightarrow e^+\bar{\nu}_\mu\nu_e$ ). Fig.2.2 shows the positron energy spectrum of two decay modes which are measured with calorimeter. The positrons from muon decay have broad energy distribution (0 ~ 52.8 MeV) because the decay is 3 body decay. Thus, even if the energy spectrum of positron from pion decay is measured, the spectrum includes not only positron from  $\pi^+ \rightarrow e^+\nu$  but also positrons from  $\pi^+ \rightarrow \mu^+\nu_\mu$ ,  $\mu^+ \rightarrow e^+\bar{\nu}_\mu\nu_e$  decay. In order to search massive neutrinos in the  $\pi^+ \rightarrow e^+\nu$  decays spectrum, positrons from  $\pi^+ \rightarrow \mu^+ \rightarrow e^+$  decay need to be suppressed. However, the pion branching ratio  $R = \Gamma(\pi^+ \rightarrow e^+\nu_e[\gamma])/\Gamma(\pi^+ \rightarrow \mu^+\nu_\mu[\gamma])$  is of the order of  $10^{-4}$  as described before. The suppression of  $\pi^+ \rightarrow \mu^+ \rightarrow e^+$  decay is the key-point of the measurement.

In order to suppress  $\pi^+ \rightarrow \mu^+ \rightarrow e^+$  decay, timing information and energy deposit information in the target is mainly used. The left histogram in Fig.2.3 shows the time difference between positron and pion obtained with a Monte Carlo simulation. The blue line shows  $\pi^+ \rightarrow e^+\nu_e$  decay and black line shows  $\pi^+ \rightarrow \mu^+ \rightarrow e^+$  decay. The positron time spectrum of each decay mode is described with the equations below.

$$F_{\pi e}(t) = A_{\pi e}e^{-t/\tau_\pi} \quad (2.2)$$

$$F_{\pi\mu e}(t) = A_{\pi\mu e}((e^{-t/\tau_\mu} - e^{-t/\tau_\pi})) \quad (2.3)$$

In the case of  $\pi^+ \rightarrow e^+\nu$  decay, the positron timing distribution is a simple exponential distribution with pion lifetime (26 ns). However in the case of  $\pi^+ \rightarrow \mu^+ \rightarrow e^+$  decay, the positron timing distribution increases with pion lifetime and decreases with muon lifetime (2.2  $\mu$ s). Therefore by selecting the early time region, the  $\pi^+ \rightarrow \mu^+ \rightarrow e^+$  decay is suppressed by a factor of 100. The cut is called Timing-Cut and 6 ns to 30 ns is used as typical Timing-Cut in this section.

The right histogram in Fig.2.3 shows the energy deposit in all the upstream detector (B1, B2, S1, S2) and the target which is called Total-Energy. The blue line shows  $\pi^+ \rightarrow e^+\nu$  decay and the black line shows  $\pi^+ \rightarrow \mu^+ \rightarrow e^+$  decay. In the case of  $\pi^+ \rightarrow e^+\nu$  decay, the energy deposit includes the kinematic energy of pion and the energy deposit of decay positron. However in addition to these, in the case of  $\pi^+ \rightarrow \mu^+ \rightarrow e^+$  decay, the energy deposit includes also the 4.1 MeV of the intermediate muon.

## 2.2. EXPERIMENTAL METHOD FOR MASSIVE NEUTRINO SEARCH IN $\pi^+ \rightarrow E^+\nu$ DECAY 9

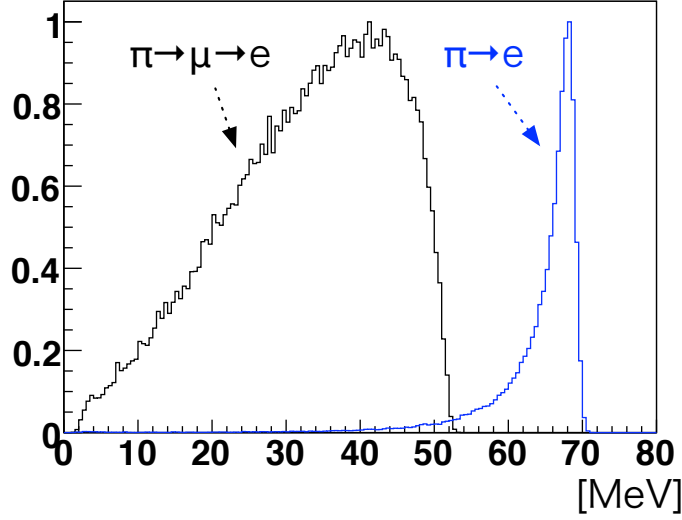


Figure 2.2: Positron energy spectrum (MC). Blue line shows  $\pi^+ \rightarrow e^+\nu_e$  decay and black line shows  $\pi^+ \rightarrow \mu^+ \rightarrow e^+$  decay. The amplitudes are normalized with the highest bins in the histograms.

The reason why Total-Energy is used instead of energy deposit in the target is to have better energy resolution of the pion energy deposit. Therefore by selecting the low energy region, the  $\pi^+ \rightarrow \mu^+ \rightarrow e^+$  decay is suppressed by a factor of  $10^3$ . The cut is called Total-Energy-Cut.

Fig.2.4 shows the positron energy spectrum after Timing-Cut and Total-Energy-Cut with Monte Carlo simulation. The black line shows the spectrum after Timing-Cut and the purple line shows the spectrum after Timing-Cut and Total-Energy-Cut. Before Total-Energy-Cut, there is a peak at 70 MeV, which is the positron from  $\pi^+ \rightarrow e^+\nu_e$  decay, and there is a continuous distribution from 0 to 52.8 MeV which is the positron from  $\pi^+ \rightarrow \mu^+ \rightarrow e^+$  decay. However after Total-Energy-Cut,  $\pi^+ \rightarrow \mu^+ \rightarrow e^+$  decay is suppressed and the amount is at the order of  $10^{-2}$  compared to  $\pi^+ \rightarrow e^+\nu_e$ .

Once the positron energy spectrum with a good suppression of  $\pi^+ \rightarrow \mu^+ \rightarrow e^+$  is obtained, massive neutrino search can be done with the spectrum. Basically the massive neutrino search corresponds to a bump search in the spectrum. If pion decay with a massive neutrino occurs, an additional peak should appear in the spectrum. The bump is searched by fitting of the spectrum and if a bump is found, the branching ratio  $\Gamma(\pi \rightarrow e\nu_i)/\Gamma(\pi \rightarrow e\nu_e)$  is evaluated with a normalization to the number of  $\pi^+ \rightarrow e^+\nu_e$  events. This is possible because the acceptance of  $\pi^+ \rightarrow e^+\nu_i$  decay and  $\pi^+ \rightarrow e^+\nu_e$  decay is almost the same. If no bump is found, upper limits for existence of massive neutrinos within a given mass range can be evaluated with the same procedure.

These are the basic methods for massive neutrino search in  $\pi^+ \rightarrow e^+\nu$  decay. In the next section, the key-points and requirements of the experiment are described.

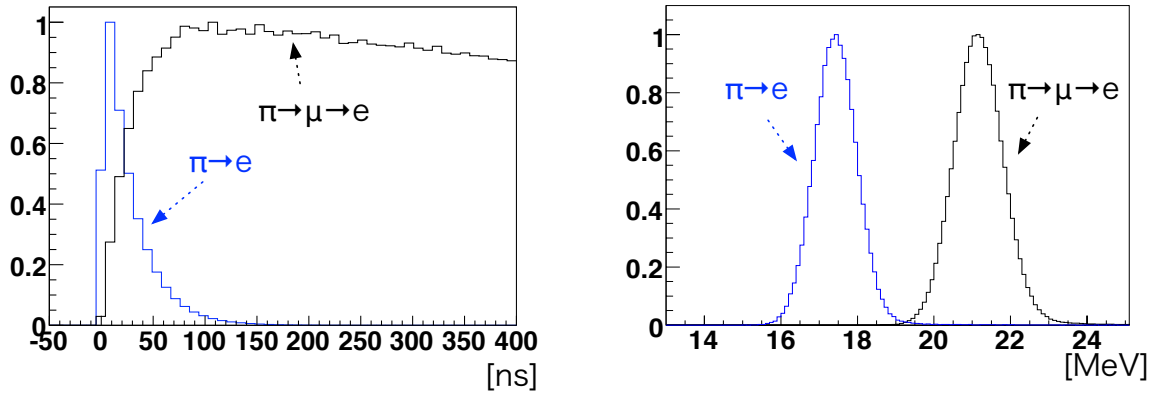


Figure 2.3: Decay time and Total-Energy of two decay modes. Blue line shows  $\pi^+ \rightarrow e^+ \nu$  decay and black line shows  $\pi^+ \rightarrow \mu^+ \rightarrow e^+$  decay. The amplitudes are normalized with the highest bins in the histograms.

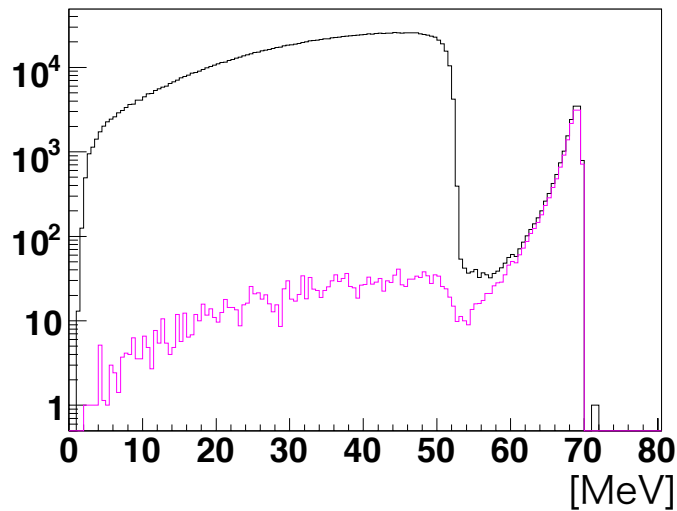


Figure 2.4: Positron energy spectrum after Timing-Cut and Total-Energy-Cut (MC). The histograms include  $\pi^+ \rightarrow e^+ \nu$  decay and  $\pi^+ \rightarrow \mu^+ \rightarrow e^+$  decay with the proper branching ratio. Black line shows after Timing-Cut and purple line shows after Timing-Cut and Total-Energy-Cut.

## 2.3 Requirement of the experiment

The sensitivity for massive neutrino search with positron energy spectrum depends on the amount of background events. The sensitivity can be described with the equation below:

$$S = \sqrt{N_{<52\text{MeV}}}/N_{>52\text{MeV}} \quad (2.4)$$

$N_{<52\text{MeV}}$  is the number of event below 52 MeV which corresponds to the number of event of background.  $\sqrt{N_{<52\text{MeV}}}$  is the statistical error and it corresponds to the sensitivity of the bump search.  $N_{>52\text{MeV}}$  is the number of event above 52MeV which corresponds to the number of  $\pi^+ \rightarrow e^+ \nu_e$  events which is used for normalization. Thus, the positron energy spectrum with lowest 'S' is needed for massive neutrino search.

In Fig.2.4, there are still some events below 52 MeV. The events includes two kind of events. One is  $\pi^+ \rightarrow \mu^+ \rightarrow e^+$  events which are not suppressed with the cuts described so far. Fig.2.5 shows Total-Energy with log scale. There are low energy tail in  $\pi^+ \rightarrow \mu^+ \rightarrow e^+$  spectrum which extends to the energy region of  $\pi^+ \rightarrow e^+$  decay. These are mainly due to the events in which pions decay in flight and muons stop in the target and decay to positron ( $\pi$ DIF). Some events in which pions decay at rest ( $\pi$ DAR) is also included but the amount is about 10 times smaller than  $\pi$ DIF events. From Monte Carlo study, it is known that tracking information of pions and positrons have capability to eliminate  $\pi$ DIF events.

The other type of events come from the low energy tail of  $\pi^+ \rightarrow e^+ \nu_e$  decay which is mainly due to shower leakage. Thus the detector should include a tracking device and a calorimeter which have lower shower leakage. The detector acceptance is also important to obtain higher statistics. The PIENU detector was designed to fulfill these requirements.

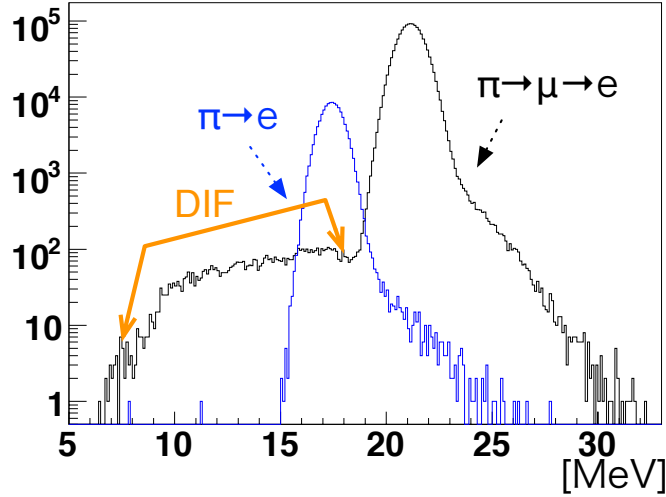


Figure 2.5: Total-Energy spectrum in log scale after Timing-Cut (MC). Black line shows  $\pi^+ \rightarrow \mu^+ \rightarrow e^+$  decay and Blue line shows  $\pi^+ \rightarrow e^+ \nu_e$  decay. Amplitude of each decay mode is set with the proper branching ratio. Low energy tail of  $\pi^+ \rightarrow \mu^+ \rightarrow e^+$  is mainly due to pion-decay-in-flight events ( $\pi$ DIF)

## 2.4 Design of the PIENU detector

Fig.2.6 shows a schematic view of the PIENU detector. The detector is made from 5 kind of sub-detectors, plastic scintillators (deep blue), wire chambers (green), silicon strip detectors (thin red box upstream and downstream of the target), NaI calorimeter (light blue) and CsI calorimeter (red boxes). Basically pions stop in the target scintillator and NaI calorimeter measure the energy of decay positrons. The tracks of beam pion and decay positron are measured by the wire chambers and the silicon strip detectors and this tracking information have the capability to eliminate  $\pi$ DIF events. The CsI calorimeter is present to detect the shower leakage escaping from the NaI calorimeter and  $\gamma$  rays from radiative pion decays. This can reduce the low energy tail of the positron from  $\pi^+ \rightarrow e^+ \nu_e$ . The acceptance of the detector is about 20% of  $4\pi$  steradians. Detail explanation about each detector competent is done in ??

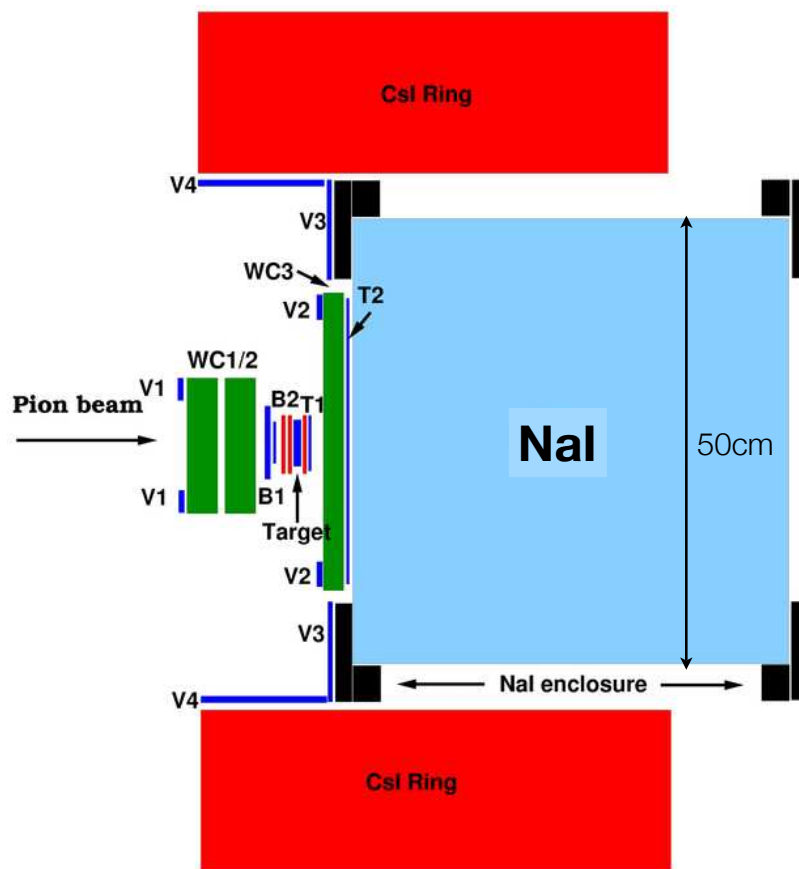


Figure 2.6: Schematic view of the PIENU detector

## 2.5 Monte Carlo study with the detector

As described in § 2.3, amount of the background in the positron energy spectrum decides the sensitivity of massive neutrino search. In this section, study of possible backgrounds with the detector is done with

a Monte Carlo simulation. However, this Monte Carlo study is not so realistic. In particular the detector geometry and the beam are not tuned to the actual experimental setup. Therefore the values which are written in this section are just rough indications to have rough understanding of the backgrounds. The possible dominant physics backgrounds can be categorized into 3 as described below. Amount of each background compare to  $\pi^+ \rightarrow e^+ \nu_e$  decay after Timing-Cut and Total-Energy-Cut are also written.

- $\pi^+ \rightarrow \mu^+ \rightarrow e^+$  muon-decay-at-rest ( $\mu DAR$ ):20%
- $\pi^+ \rightarrow \mu^+ \rightarrow e^+$  muon-decay-in-flight ( $\mu DIF$ ):2%
- Low energy tail of  $\pi^+ \rightarrow e^+ \nu_e$ :8%

The reasons why background from  $\pi^+ \rightarrow \mu^+ \rightarrow e^+$  is categorized into  $\mu DAR$  and  $\mu DIF$  is that in the case of  $\mu DIF$ , Timing-Cut and Total-Energy-Cut is not effective because muons and positrons have the same timing and muons don't deposit energy in the target. Useful variable for background suppression is and rough estimation of background are studied in this section.

### 2.5.1 $\pi^+ \rightarrow \mu^+ \rightarrow e^+$ muon-decay-at-rest event ( $\mu DAR$ )

$\pi^+ \rightarrow \mu^+ \rightarrow e^+$  muon-decay-at-rest ( $\mu DAR$ ) is the biggest background source and the amount is about 20% after Timing-Cut and Total-Energy-Cut. However tracking information have the capability to identify these events.

Fig.2.7 shows a schematic view of tracking device and tracks of pion decays. There are 3 pairs of tracking detector (Tr1, Tr2, Tr3). In the case of  $\pi^+ \rightarrow e^+ \nu$  decay, there are only two tracks which are pion track and decay positron track. In the case of  $\pi^+ \rightarrow \mu^+ \rightarrow e^+$  decay, the decay can be categorized into 3. One is pion decay-in-flight upstream of the target ( $\pi DIF-us$ ), this kind of event has the muon track before the target as shown Fig.2.7. The second one is pion decay-in-flight in the target but before stopping ( $\pi DIF-it$ ). The third one is pion decay-at-rest ( $\pi DAR$ ).  $\pi DIF-it$  and  $\pi DAR$  events have muon track in the target as shown Fig.2.7. Fig.2.8 shows Total-Energy in log scale after Timing-Cut. Blue line is  $\pi^+ \rightarrow e^+ \nu_e$  events, black line is  $\pi DAR$ , red line is  $\pi DIF-us$  and purple line is  $\pi DIF-it$ . From this histograms we can see that the events which are left after Total-Energy-Cut are mainly  $\pi DIF-us$  and  $\pi DIF-it$  events. Tracking information is used to suppress these kind of events as described below.

**Incident-Angle-Cut** Fig.2.9 shows the the angle of the track at Tr1 and track at Tr2 which is labelled as  $\theta$  in Fig.2.7.  $\pi DIF-us$  events in which muons stop in the target and Total-Energy is the same with  $\pi^+ \rightarrow e^+ \nu$  decay have angle of about  $30^\circ$  though other kind of events have about  $0^\circ$ . With this information  $\pi DIF-us$  can be rejected by a factor of about 5.  $\pi DIF-us$  in which pion decays after S2 detector cannot be rejected with this tracking information. The cut is called Incident-Angle-Cut.

**Vertex-Cut** In the case of  $\pi^+ \rightarrow e^+$  decay, there is only two tracks which are pion's and positron's. Therefore the vertex reconstruction with Tr2(S1&S2) and Tr3 (S3&WC3) is possible. The closest approach of upstream track and downstream track (Rmin) should be distributed around 0 and the Z (beam axis) position of the vertex (Zmin) should have a sharply distribution. However, the vertex reconstruction may be wrong if the events have an intermediate muon. Thus, vertex information can detect the  $\pi DIF$  events which occur after S2 and the normal  $\pi DAR$  events. Fig.2.10 shows Rmin and Zmin of the 2 decay modes after Total-Energy-Cut and Incident-Angle-Cut. It shows that both variable have the capability to suppress all kind of  $\pi^+ \rightarrow \mu \rightarrow e^+$  events by a factor of about 2~5. These cuts is called Rmin-Cut and Zmin-Cut.

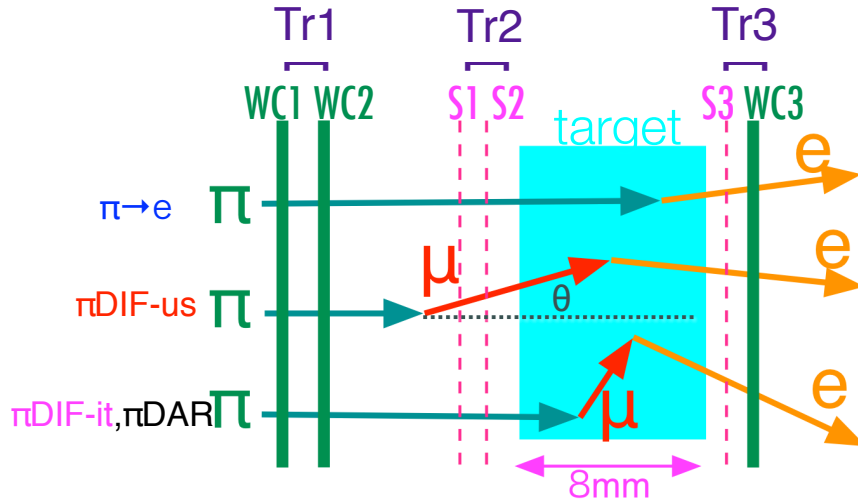
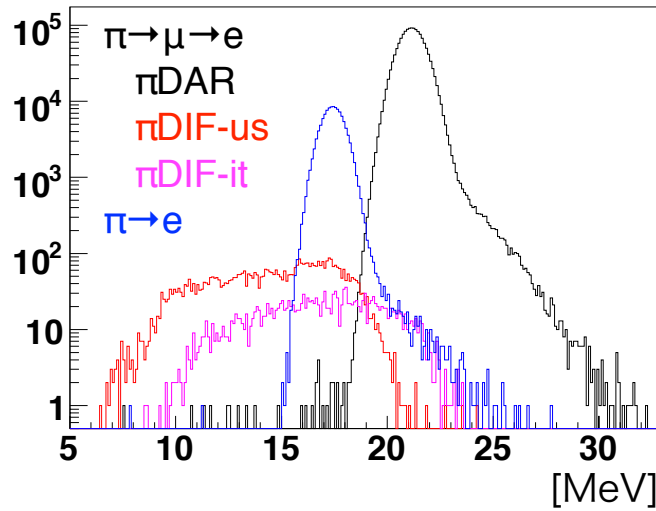


Figure 2.7: Schematic view of track of pion decay

Figure 2.8: Total-Energy distribution(MC) after timing cut(6-30ns) Blue line:  $\pi^+ \rightarrow e^+ \nu_e$ . Black line:  $\pi^+ \rightarrow \mu \rightarrow e^+ \pi$ DAR. Red line:  $\pi^+ \rightarrow \mu \rightarrow e^+ \pi$ DIF-us. Purple line:  $\pi^+ \rightarrow \mu \rightarrow e^+ \pi$ DIF-it.

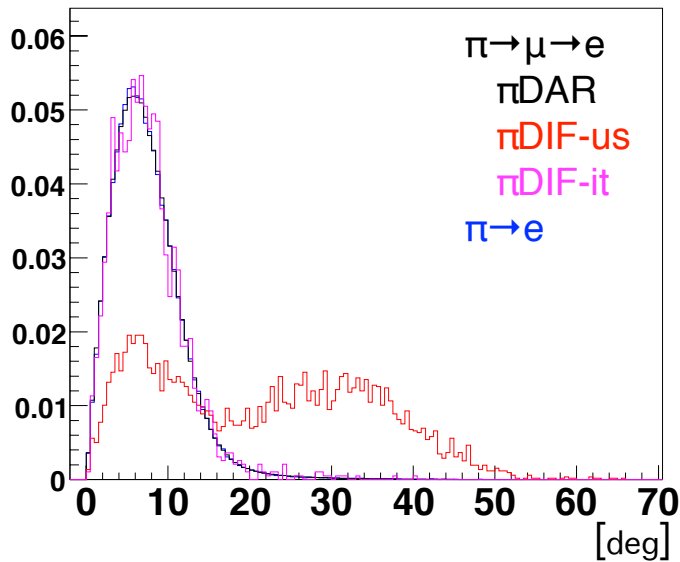


Figure 2.9: Incident angle distribution after Total-Energy-Cut (MC). Black line:  $\pi^+ \rightarrow \mu \rightarrow e^+ \pi$  DAR. Red line:  $\pi^+ \rightarrow \mu \rightarrow e^+ \pi$  DIF-us. Purple line:  $\pi^+ \rightarrow \mu \rightarrow e^+ \pi$  DIF-it. Blue line:  $\pi^+ \rightarrow e^+ \nu_e$ .

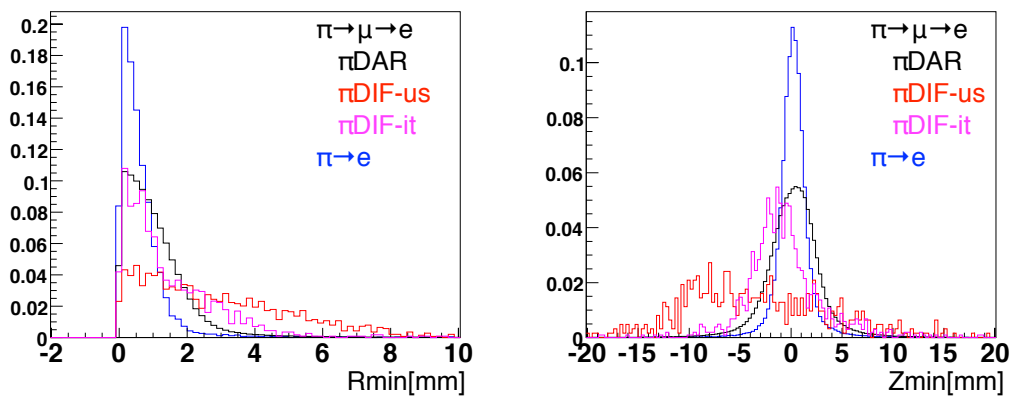


Figure 2.10: Vertex reconstruction information after Total-Energy-Cut and Incident-Angle-Cut (MC). Black line:  $\pi^+ \rightarrow \mu \rightarrow e^+ \pi$  DAR. Red line:  $\pi^+ \rightarrow \mu \rightarrow e^+ \pi$  DIF-us. Purple line:  $\pi^+ \rightarrow \mu \rightarrow e^+ \pi$  DIF-it. Blue line:  $\pi^+ \rightarrow e^+ \nu_e$ .

**Summary of tracking cut** The Monte Carlo study shows that the  $\pi^+ \rightarrow \mu^+ \rightarrow e^+$  muon-decay-at-rest ( $\mu DAR$ ) events left after tracking cut is about 4% compared to  $\pi^+ \rightarrow e^+ \nu$ .

### 2.5.2 $\pi^+ \rightarrow \mu^+ \rightarrow e^+$ muon-decay-in-flight event ( $\mu DIF$ )

The probability of muon-decays-in-flight ( $\mu DIF$ ) is very low. However, all the cut which are described before is not effective to  $\mu DIF$  events, because muons and positrons have the same timing and muons don't deposit energy in the target and the track of the muons is very short. The top left histogram in Fig.2.11 shows muon decay time of  $\mu DIF$  events. It takes about 18 ps before muons stop in the target. With these information and the fact muons from pion decay have 4.1 MeV kinematic energy ( $\beta=0.27$   $\gamma=1.039$ ), probability of muon-decays-in-flight ( $P_{DIF}$ ) is calculated as below:

$$P_{DIF} = 1 - \exp\left(\frac{-0.018/1.039}{2193}\right) = 7.90 \quad (2.5)$$

$$times 10^{-6} \quad (2.6)$$

The top right histogram in Fig.2.11 shows the kinematic energy distribution of the muons which decay-in-flight. If the energy is less than 3.3 MeV, which corresponds to 0.8 MeV energy deposit in the target, can be rejected with Total-Energy-Cut. From the histogram the efficiency of the events left after Total-Energy-Cut is about 30%. The ratio of the events left in the positron energy spectrum compared to  $\pi^+ \rightarrow e^+ \nu_e$  decay ( $R_{DIF}$ ) is calculated as below by using the cut efficiency and considering the branching ratio.

$$R_{DIF} = P_{DIF} \times 0.3 / (1.23 \times 10^{-4}) = 1.9\% \quad (2.7)$$

The bottom left histogram in Fig.2.11 shows positron energy spectrum of the  $\mu DIF$  events. Black line shows all the  $\mu DIF$  events and red line shows the  $\mu DIF$  events with muon energy cut which corresponds to Total-Energy-Cut. The spectrum has a bit different shape with  $\mu DAR$  events because there is energy boost due to the kinematic energy of the muon.

### 2.5.3 Low energy tail of $\pi^+ \rightarrow e^+ \nu_e$ event

Fig.2.12 shows the positron energy spectrum of  $\pi^+ \rightarrow e^+ \nu_e$  decay with and without adding energy deposit in the CsI calorimeter. The tail become smaller by adding the energy deposit in the CsI calorimeter. The tail less than 52 MeV is reduced from 8% to 2% with the CsI calorimeter.

### 2.5.4 Summary of Monte Carlo study

The background ratio compared to  $\pi^+ \rightarrow e^+ \nu_e$  after using tracking information and CsI energy deposit is below.

- $\pi^+ \rightarrow \mu^+ \rightarrow e^+$  muon-decay-at-rest ( $\mu DAR$ ): 4%
- $\pi^+ \rightarrow \mu^+ \rightarrow e^+$  muon-decay-in-flight ( $\mu DIF$ ): 2%
- low energy tail of  $\pi^+ \rightarrow e^+ \nu_e$ : 2%

In total, it is about 8% and it was 18% in the previous experiment in TRIUMF[13]. However, this Monte Carlo study is not so realistic. In particular the detector geometry and the beam are not tuned to the actual experimental setup. Therefore the amount of the background are just rough indications.

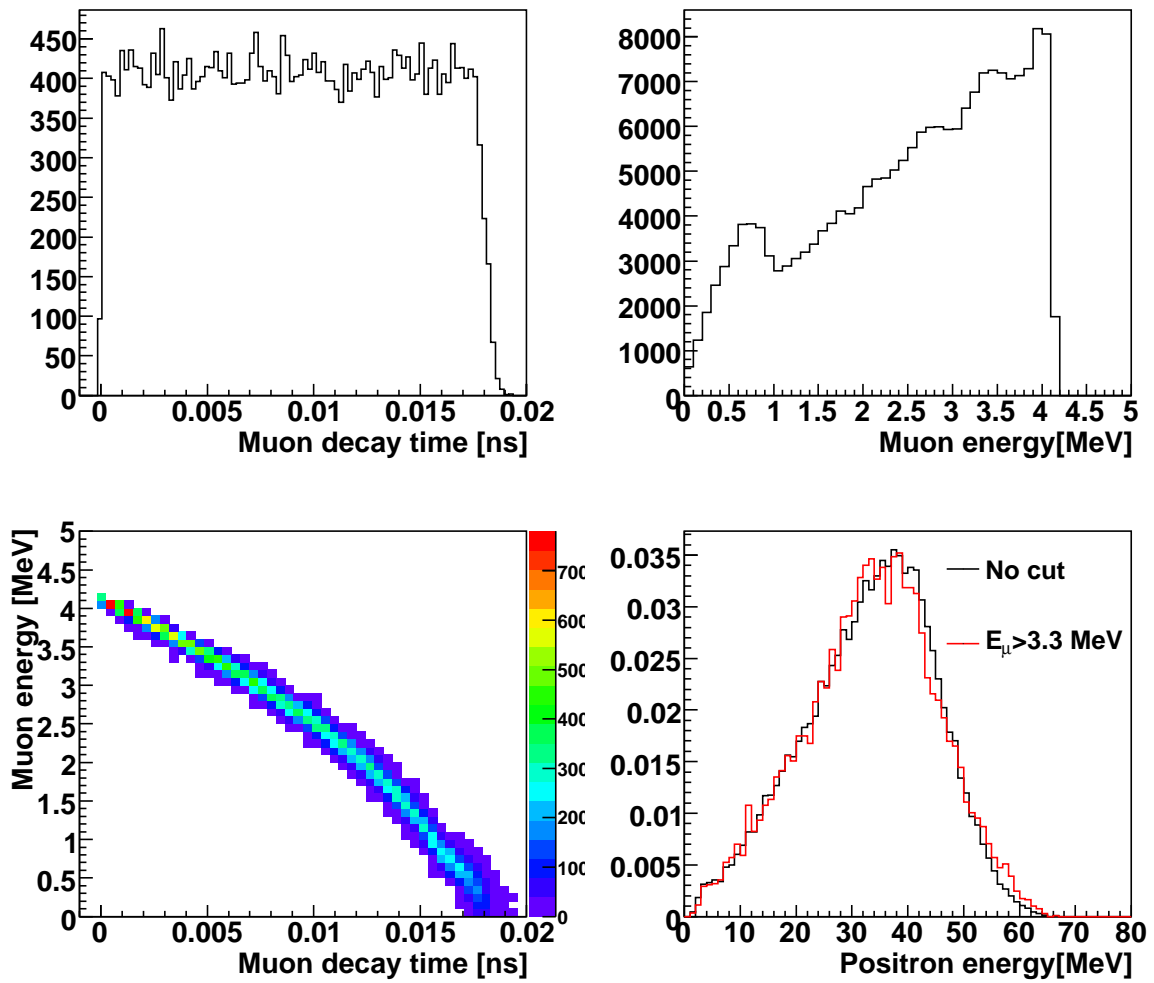


Figure 2.11: Information of  $\pi^+ \rightarrow \mu^+ \rightarrow e^+$  muon-decay-in-flight event. Top left: Muon decay time. Top right: Muon kinematic energy. Bottom left: Muon decay time V.S. muon kinematic energy. Bottom right: Positron energy spectrum.

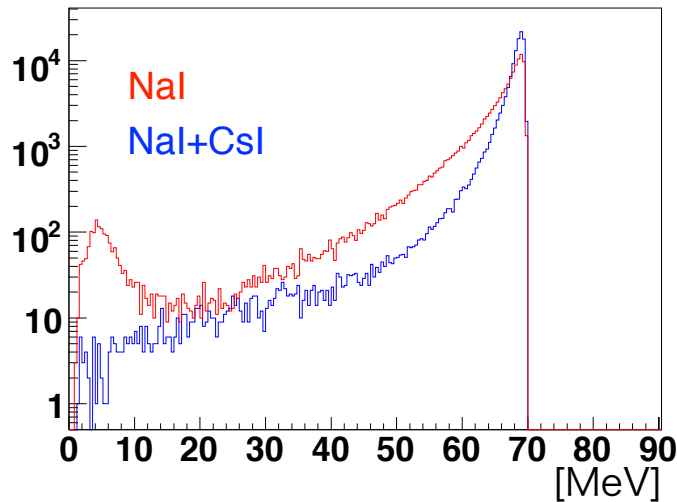


Figure 2.12: Positron energy spectrum w/ and w/o CsI Red line:Positron energy deposit in NaI Blue line:Positron energy deposit in NaI and CsI

## 2.6 History and future plan of the experiment

A brief history and future plan of the PIENU experiment is summarized in Table 2.1. The detector was completed in May, 2009 and first data taking is carried out from May to September in 2009 (RUN-I). In this thesis RUN-I data are analyzed which corresponds to 1 M  $\pi^+ \rightarrow e^+\nu_e$  event. Our statistical goal is more than 3M  $\pi^+ \rightarrow e^+\nu_e$  event. The data taking will continue till end of 2011 and in total about 7M  $\pi^+ \rightarrow e^+\nu_e$  event data will be obtained.

Year	Month	Events
History		
2006	Dec.	Proposal was approved by TRIUMF
2007		Detector design and some test were done
2008	Oct.	M13 beam channel extension was completed
2008	Oct-Nov	Test in M13 with all detector component was done
2009	May	The PIENU detector was completed
2009	May.-Sep.	Run-I (1M $\pi^+ \rightarrow e^+\nu_e$ )
2009	Oct.-Dec	Run-II (0.5M $\pi^+ \rightarrow e^+\nu_e$ )
Future Plan		
2010	Apr.-Dec.	Run-III (3M $\pi^+ \rightarrow e^+\nu_e$ )
2011	Apr.-Dec	Run-IV (3M $\pi^+ \rightarrow e^+\nu_e$ )

Table 2.1: History and future plan of the PIENU experiment

## Chapter 3

# Description of the experiment

### 3.1 Beamline

The experiment was performed in the M13 beam channel area at TRIUMF. A schematic view of the M13 beam line is shown in Fig.3.1. The primary proton beam hit T1 target and the secondary particles emitted from T1 target are extracted to the beam channel. The primary proton beam comes from the TRIUMF main cyclotron. The proton energy is 500 MeV at a beam current of  $100\mu\text{A}$ . The cyclotron RF periodicity is 23 MHz. T1 target is made of 1-cm thick Be block. The beginning of the secondary beam line is located at an angle of  $135^\circ$  from the proton beam line. The beam line is made from 3 dipole magnet (B1,B2,B3) and 10 quadrupole magnets (Q1~Q10). The secondary beam includes mainly pion, muon and positron. In order to suppress contamination of beam positron, an energy-loss technique is used in this beam line.[15]

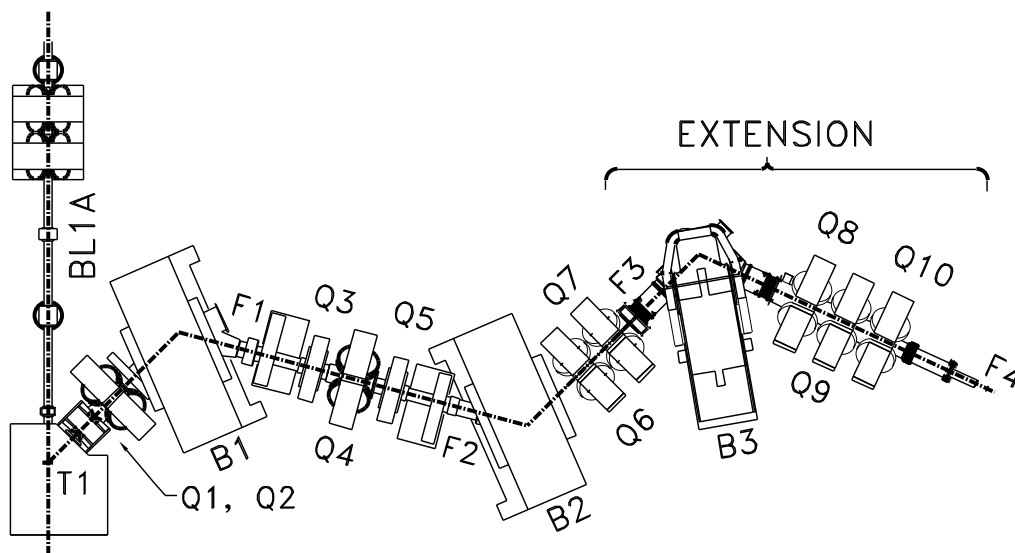


Figure 3.1: Schematic view of M13 beam channel. Downstream of F3 has been upgraded for the PIENU experiment.

B1 magnet selects the beam momentum at 77 MeV/c and F1 slit define the momentum bite of the beam. A thin foil is inserted at the absorber wheel near F1 and a momentum spread between pions and positrons results due to the energy loss difference. After B2 magnet the horizontal distribution of pions and positrons is different due to the momentum spread. Fig.3.2 shows the X position measured by the wire chamber at F3. There is 5 cm difference between pions and positrons. A collimator is placed at F3 to stop only positrons. The last bend at B3 magnet get rid of some background emitted from the collimator. The left histogram in Fig.3.3 shows the energy deposit measured by a plastic scintillator. There are 3 peaks which corresponds to positrons, muons and pions respectively. The pion purity in the beam is more than 80%. In the normal data taking condition, the pion rate is 60 kHz with a momentum of 75MeV/c. The momentum bite is less than 1.5%(FWHM) and the profile is about 10 mm as shown in the right histogram in Fig3.3. Downstream of F3 has been upgraded for the PIENU experiment. Fig.3.4 shows the picture of M13 beam channel before and after the upgrade.

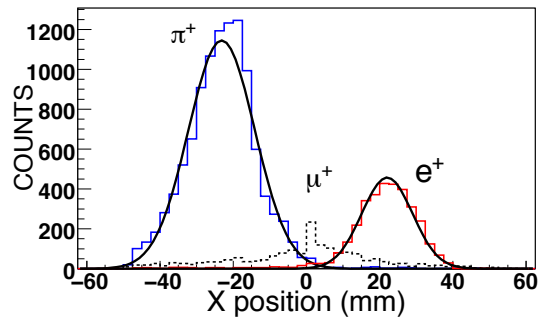


Figure 3.2: Beam profile at F3. Blue is pions. Red line is positron. Dashed line is muons.

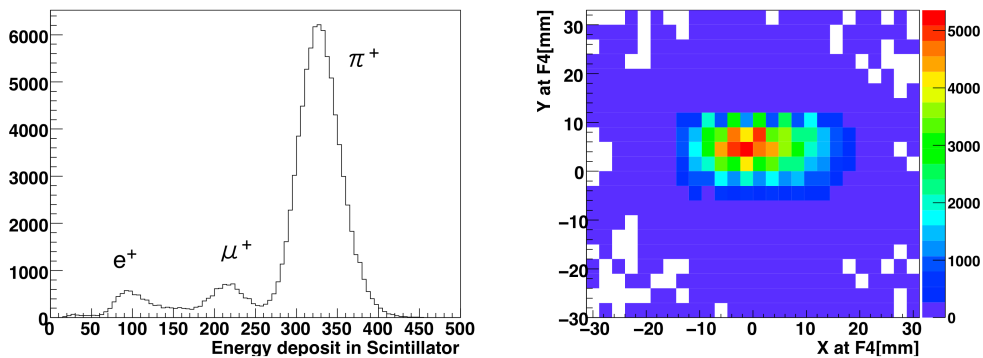


Figure 3.3: Right: Energy deposit in a scintillator of the beam particle. Left: Beam profile at F3 measured by the wire chamber.

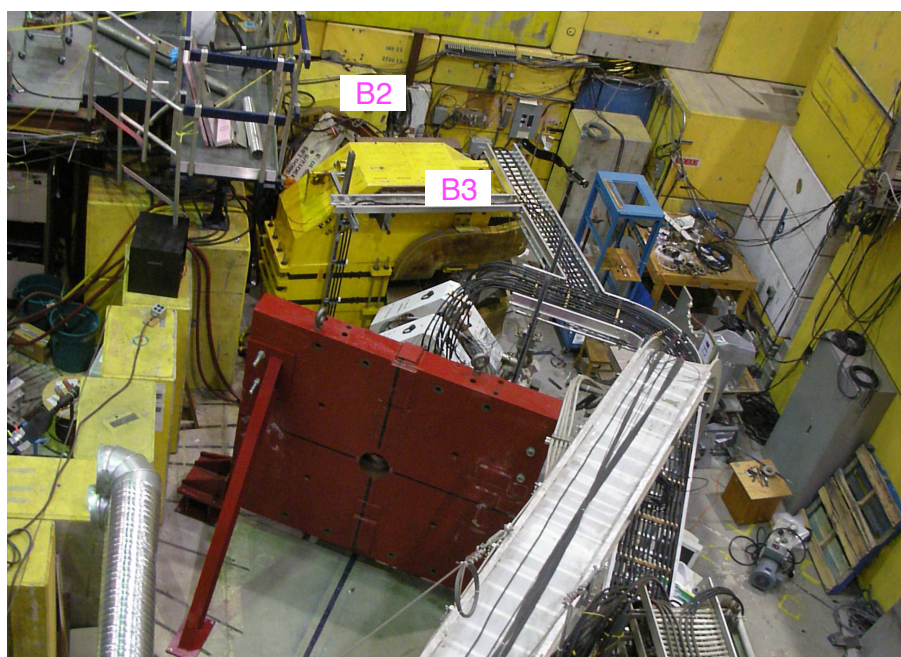
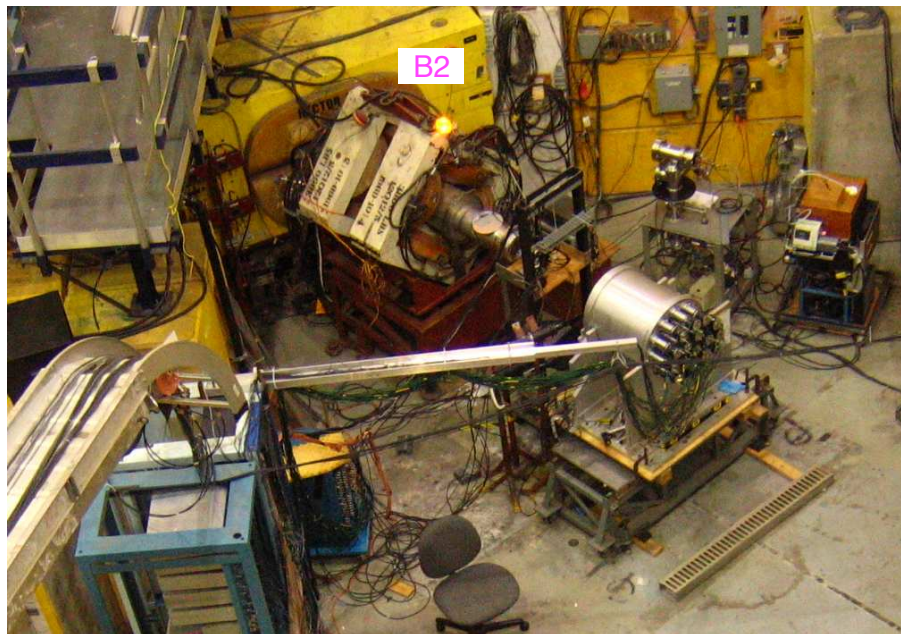


Figure 3.4: Picture of M13 beam channel. Top picture is before the upgrade and bottom one is after the upgrade.

## 3.2 Detector

### 3.2.1 Overview of the detector

As explained in §.2.4 the basis of the detector is an active pion stopping target and a calorimeter to measure the energy of the decay positrons. Fig.3.5 shows a schematic view of the PIENU detector. The detector is made from 5 kind of sub-detectors, plastic scintillator (deep blue), wire chamber (green), silicon strip detector (thin red box), NaI calorimeter (light blue) and CsI calorimeter (red boxes). Tracks of beam pion and decay positron is measured by the wire chambers and the silicon strip detectors. The CsI calorimeter detect the shower leakage from the NaI calorimeter and  $\gamma$  rays from radiative pion decays to reduce the low energy low energy tail of the positron from  $\pi^+ \rightarrow e^+ \nu_e$  decay. The acceptance of the detector is about 20% of  $4\pi$  steradians. Detailed explanation about each detector components is done in this section.

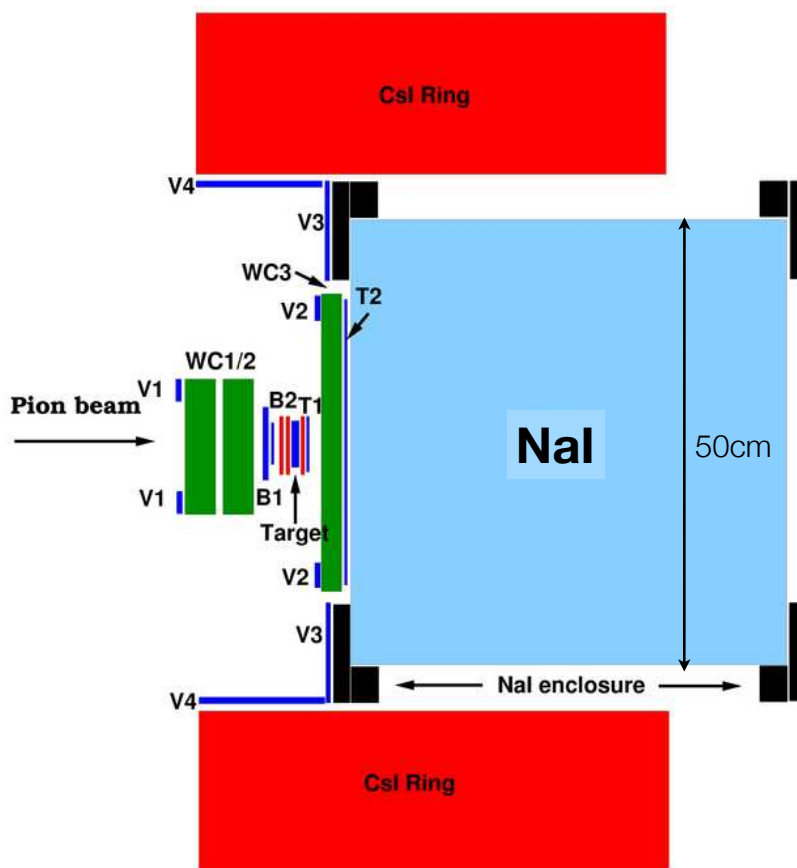


Figure 3.5: Schematic view of the PIENU detector

### 3.2.2 Plastic scintillators

As shown in Fig.3.5, there are 4 kind of scintillating counter. The most important one is the target where pions stop. There are 2 beam counter (B1, B2) in front of the target. The beam counters define the pion timing and the energy deposit in these is used for particle identification. B2 counter is 45 mm and smaller than the target and defines the beam profile at the target in order to avoid the escape of the decay muon from the target. 2 telescope counters are located downstream of the target (T1, T2). Telescope counters define the positron timing. There are 4 veto counters (V1,V2,V3,V4). V4 doesn't exist in the current detector. Veto counters are not used in the analysis of this thesis. Sizes of the scintillating counters are shown in Table.3.1. All the scintillating counter except veto counters and T2 counter are square and read by 4 PMTs. All the veto counters are annular. T2 is round and read out by wave-length-shifting-fiber with 4 PMTs. Target and T1 are rotated 45°. All the PMT signals are read out by 500-MHz FADC. The efficiency of all beam counters, telescope counters and the target is more than 99% for beam positrons.

Name	X(R-in)[mm]	Y(R-out)[mm]	Z[mm]	PMTs
B1	100	100	6.35	4
B2	45	45	3.175	4
Target	70	70	8.0	4
T1	80	80	3.175	4
T2	(0)	(165.375)	6.35	4
V1	(40)	(52)	3.175	1
V2	(107.95)	(150.65)	6.35	1
V3	(177.8)	(241.3)	6.35	1

Table 3.1: Sizes of the scintillating counters

### 3.2.3 Beam wire chambers (WC1&WC2)

WC1 and WC2 are used for beam particle tracking. Each wire chamber consist of three wire planes rotated at 120° with respect to one another. Each planes have an active diameter of each plane is 10.6 cm and consists of 40 read out wires. The read out wire pitch is 2.4 mm. The chamber is a proportional chamber and the position resolution is decided by the wire pitch. WC1 and WC2 is actually integrated as one chamber which has 6 planes. The chamber is mounted directly to the beam pipe immediately after the beam-pipe window. The chamber is filled with the standard CF4-Isobutane mixture (80% : 20%) at atmospheric pressure. Signals after discriminator which have only timing information are read out by multi-hit TDCs. The efficiency of the chamber is more than 99% for beam positron. Fig.3.6 shows the picture of the beam wire chamber. The left picture was taken before putting the wire plane were installed and the right picture is the chamber mounted onto the beam pipe.

### 3.2.4 Wire Chamber 3

WC3 is used for the tracking of decay positrons. The chamber consists of three wire planes rotated at 120° with respect to one another. The active diameter of each plane is 24.72 cm and it has 48 read out wires. The read out wire pitch is 4.8 mm. WC3 is a proportional chamber as well and the position

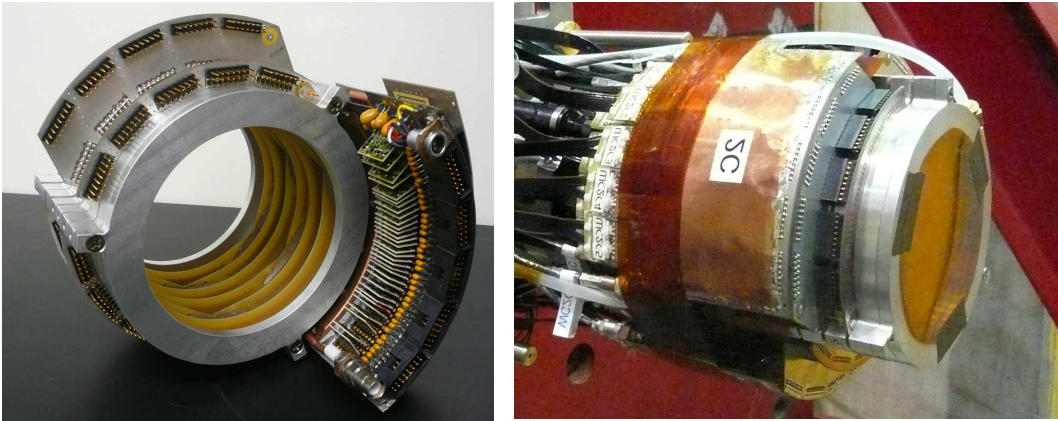


Figure 3.6: Picture of beam wire chamber. The left picture was taken before putting the wire plane were installed and the right picture is the chamber mounted onto the beam pipe.

resolution is decided by the wire pitch. WC3 is mounted onto the flange of the NaI crystal enclosure. The gas is also CF<sub>4</sub>-Isobutan. Signals after discriminator which has only timing information are read out by multi-hit TDCs. The efficiency of the chamber is more than 99% for beam positron. Fig.3.7 is the picture of WC3 mounted onto the flange of the NaI crystal enclosure.

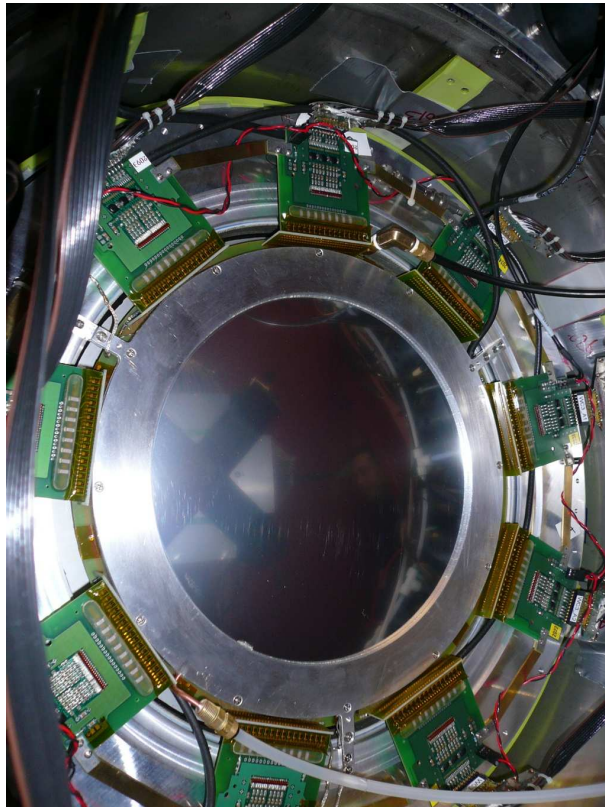


Figure 3.7: Picture of wire chamber 3 mounted onto the flange of the NaI crystal enclosure.

### 3.2.5 Silicon strip detectors

There are 3 sets of silicon strip detector (S1,S2,S3). S1 and S2 are located in front of the target and S3 is located immediately after the target. These are for tracking of incoming and outgoing particle from the target. One set of the silicon strip detector has 2 plane (X and Y). One plane has a Si sensor which is a single-sided AC-coupled micro-strip detector with an active area of approximately  $61 \text{ mm} \times 61 \text{ mm} \times 285 \mu\text{m}$  and a strip pitch of  $80 \mu\text{m}$ . The required resolution for the PIENU experiment is  $300 \mu\text{s}$  and therefore four Si strip are bonded to one readout line. For further reduction of readout channels, the lines are interconnected with capacitors and only each fourth line is connected to an amplifier as shown in Fig.3.8. 48 channels are readout with this procedure. The capacitive network forms a charge division line where reconstruction of ionization amplitude and position is made by proper weighting of signals from two of 48 channels. The raw signal of all channels are readout by 60MHz FADC. In order to reduce the data size with online, the hardware threshold is set to suppress the data which have no hit. The charge division method works well without data suppression and the efficiency is more than 99% for beam positrons. However with data suppression, the efficiency drops to about 90% for beam positrons because the charge is divided into two strip and become too low to discriminate against the noise. This happens because the hardware threshold is applied to each strip not to the sum of the 2 channels. The efficiency for pion is more than 99% because the energy deposit of pions is large enough. The readout module will be updated to improve the efficiency. Fig.3.9 is the picture of the silicon strip detector. The left picture is before the mounting out the support structure and the right picture is after the integration of 2 plane as one set of detector.

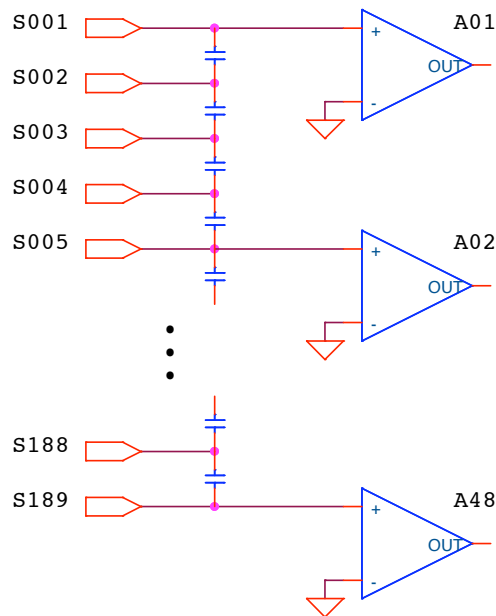


Figure 3.8: Schematic of the silicon strip readout scheme. The lines are interconnected with capacitors and only each fourth line is connected to an amplifier.

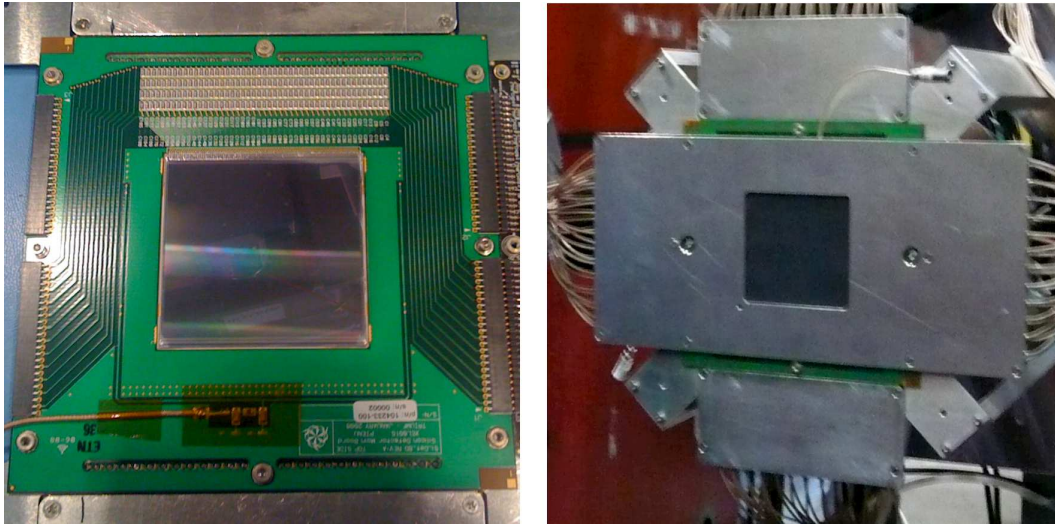


Figure 3.9: Picture of a silicon strip detector. Left picture shows before the mounting out the support structure. Right picture shows after the integration of 2 plane as one set of detector.

### 3.2.6 NaI calorimeter

The NaI calorimeter is used for the positron energy measurement. The crystal has the shape of a cylinder 48cm in diameter and 48 cm in length. The crystal is enclosed in an aluminum enclosure and have 19 circular windows at the rear end. The thickness of the front aluminium plate is 0.5mm. All PMTs are readout by 30MHz FADC. Fig.3.10 shows the picture of the NaI crystal.

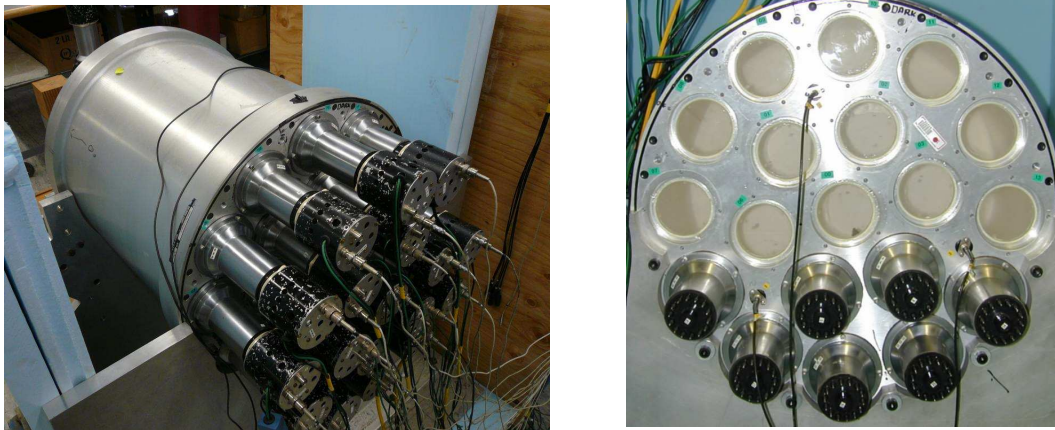


Figure 3.10: Picture of the NaI calorimeter.

### 3.2.7 CsI ring calorimeter

The CsI ring calorimeter is used to detect shower leakage escaping from the NaI calorimeter and  $\gamma$  rays from radiative pion decays. The calorimeter consists of 97 CsI crystals and each crystal is readout with a PMT. The picture of the crystal is shown in Fig.3.11. The crystal is about 8.5 cm  $\times$  9 cm  $\times$  25 cm.

The bottom picture in Fig.3.11 shows the crystals mounted on support structure. The NaI crystal is at the center of the CsI ring calorimeter. All PMT signals are readout by 60MHz FADC with a certain threshold for data suppression.

### 3.2.8 Whole detector assembly

Fig.3.12 shows a CAD design of the complete detector assembly. The detector is divided into 2 portions. One is called PIENU-1 which is attached to the beam-pipe and another one is PIENU-2 which is cylinder. PIENU-1 consists of WC1, WC2, V1, B1, B2, S1, S2, Target, S3, T1. PIENU-2 consists of WC3, T2, V2, V3, CsI, NaI. Fig.3.13 shows the picture of PIENU-1 and PIENU-2. PIENU-2 is be set as close as possible to PIENU-1 The top picture in Fig.3.14 shows the whole detector in which PIENU-2 is located as close as possible to PIENU-1. The bottom picture of Fig.3.14 shows the picture of the detector and the beamline from the side. Fig.3.15 is the picture of the M13 beam channel taken from the top.

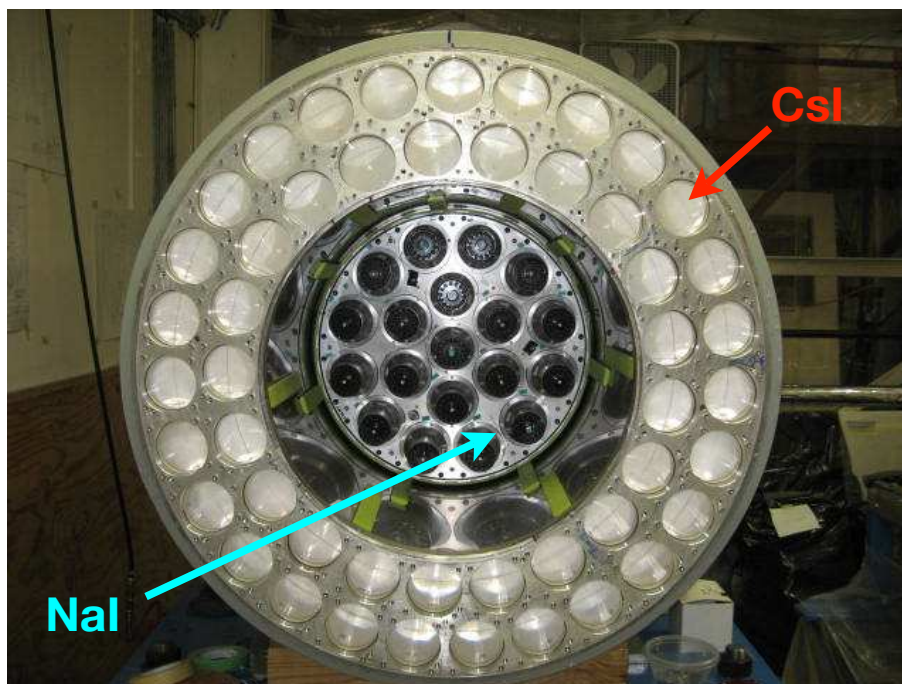
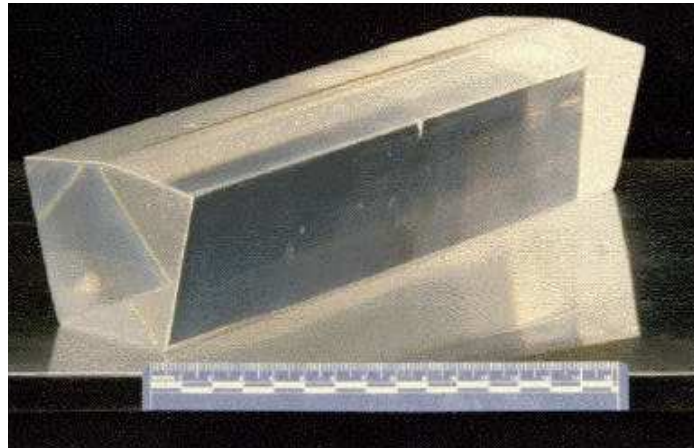


Figure 3.11: Picture of the CsI calorimeter. Top picture shows a single CsI crystal. Bottom picture shows whole calorimeter which include 97 CsI crystals and the NaI crystal.

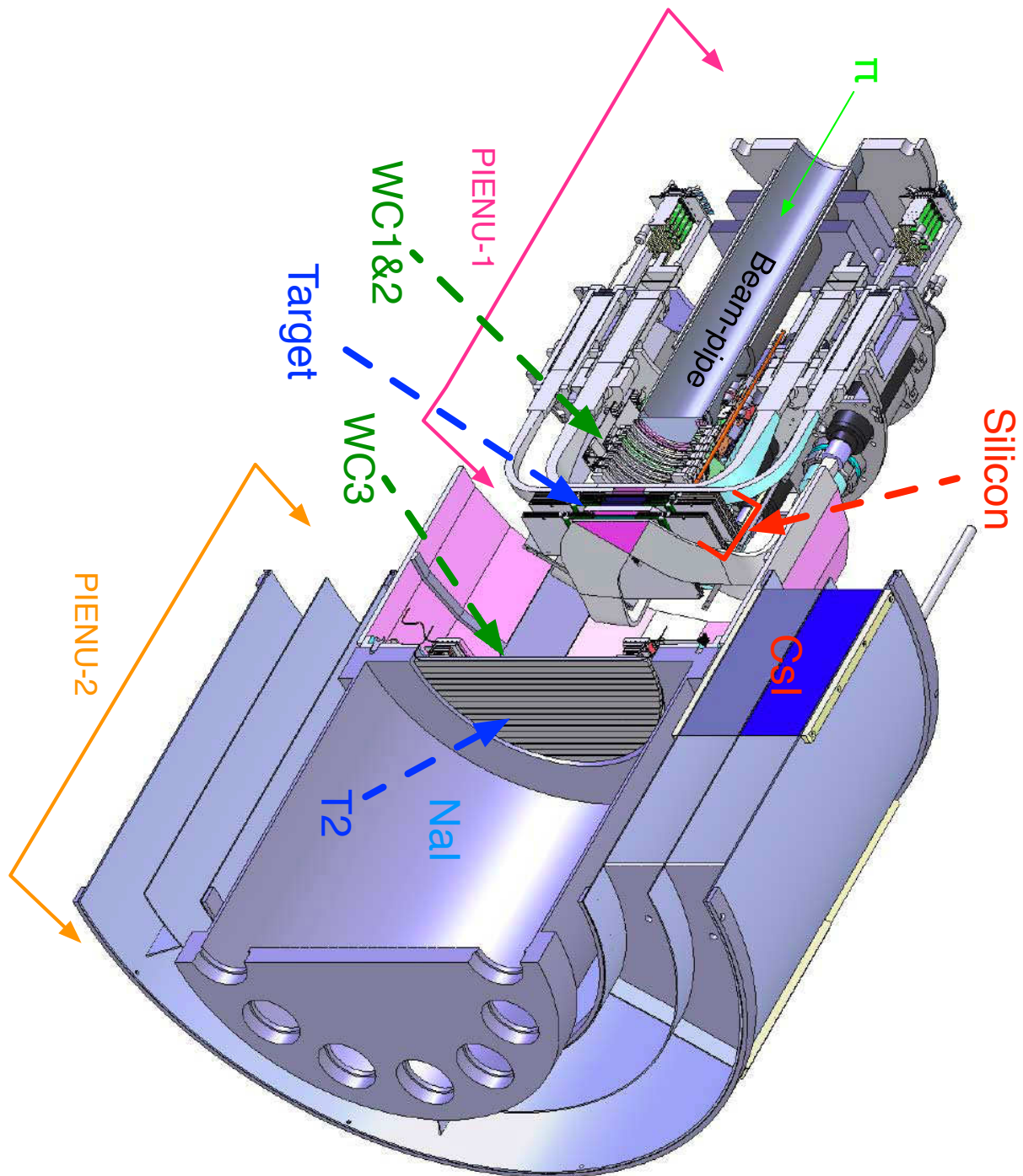


Figure 3.12: CAD design of the PIENU detector

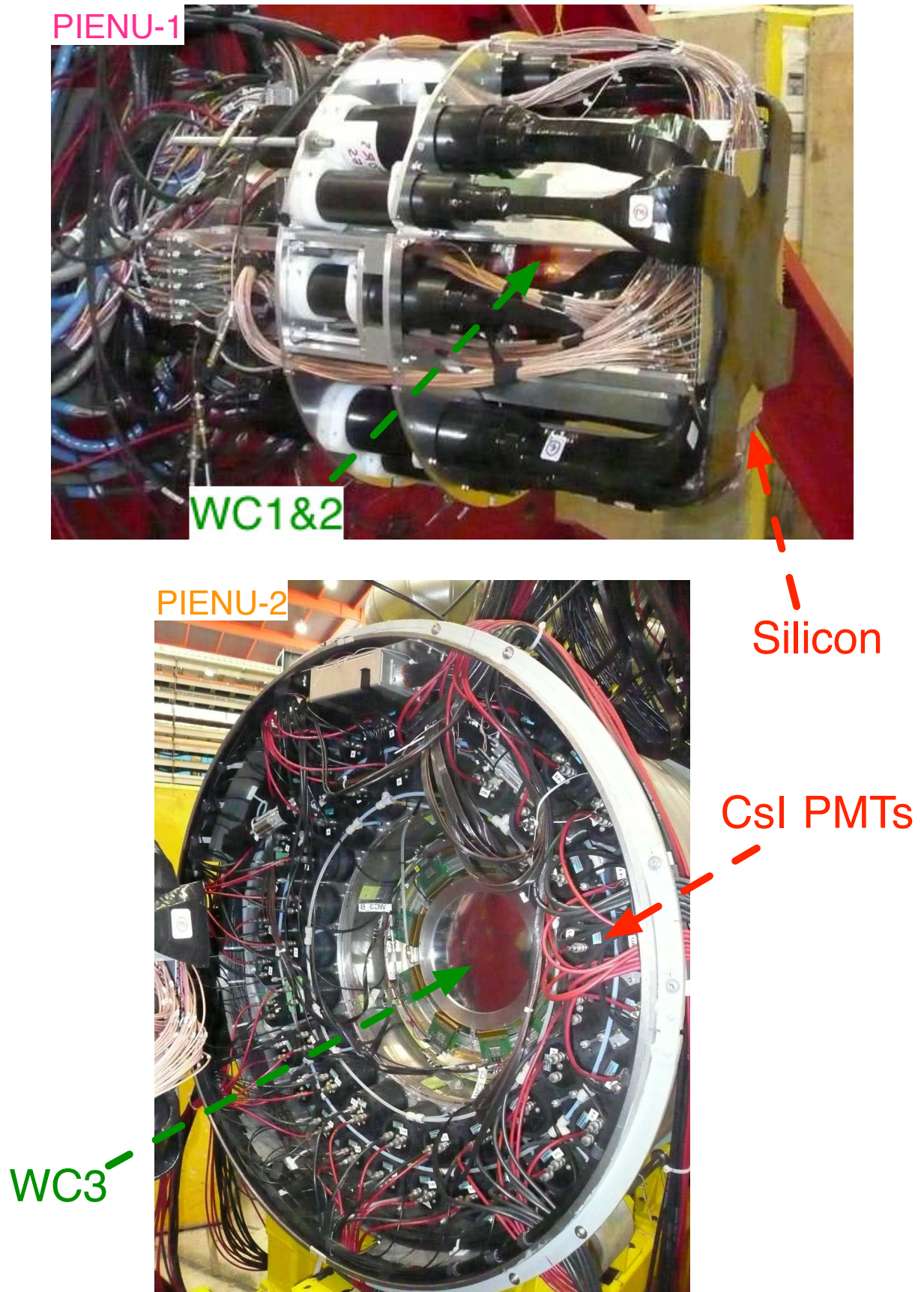


Figure 3.13: Picture of the detector assembly 1.

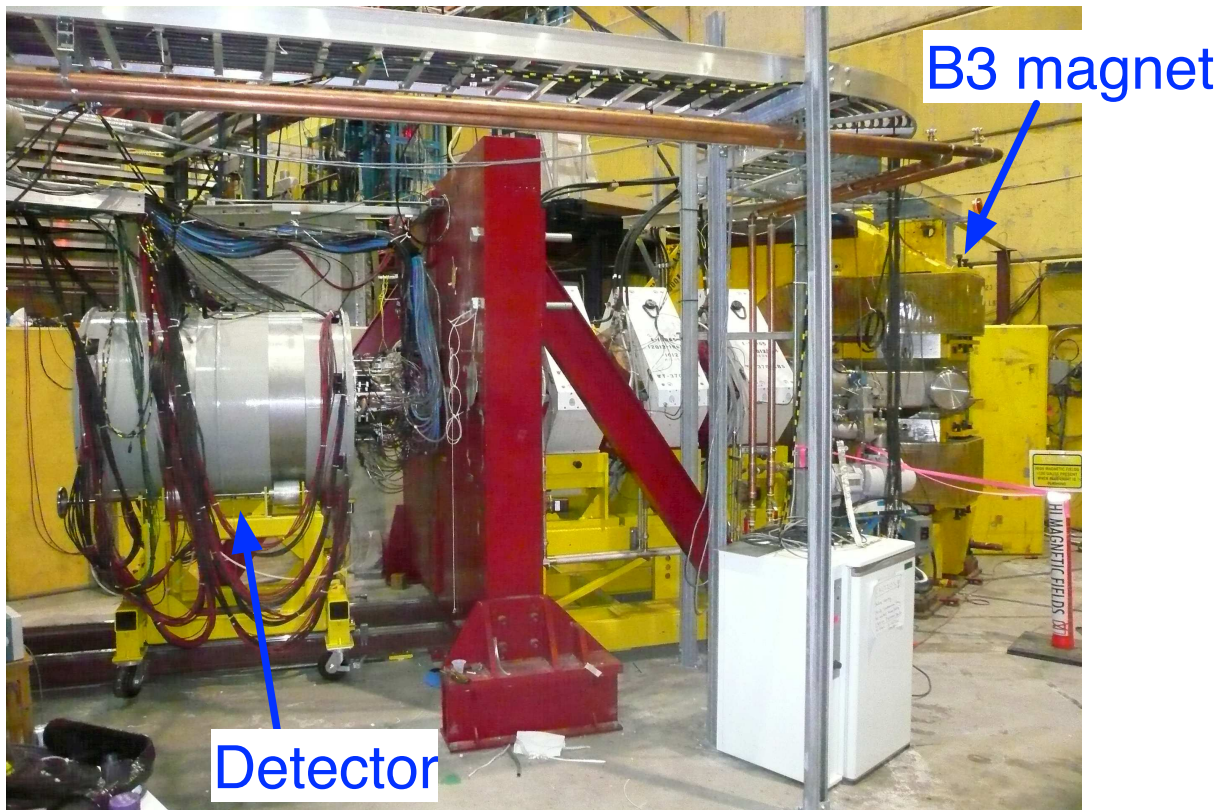
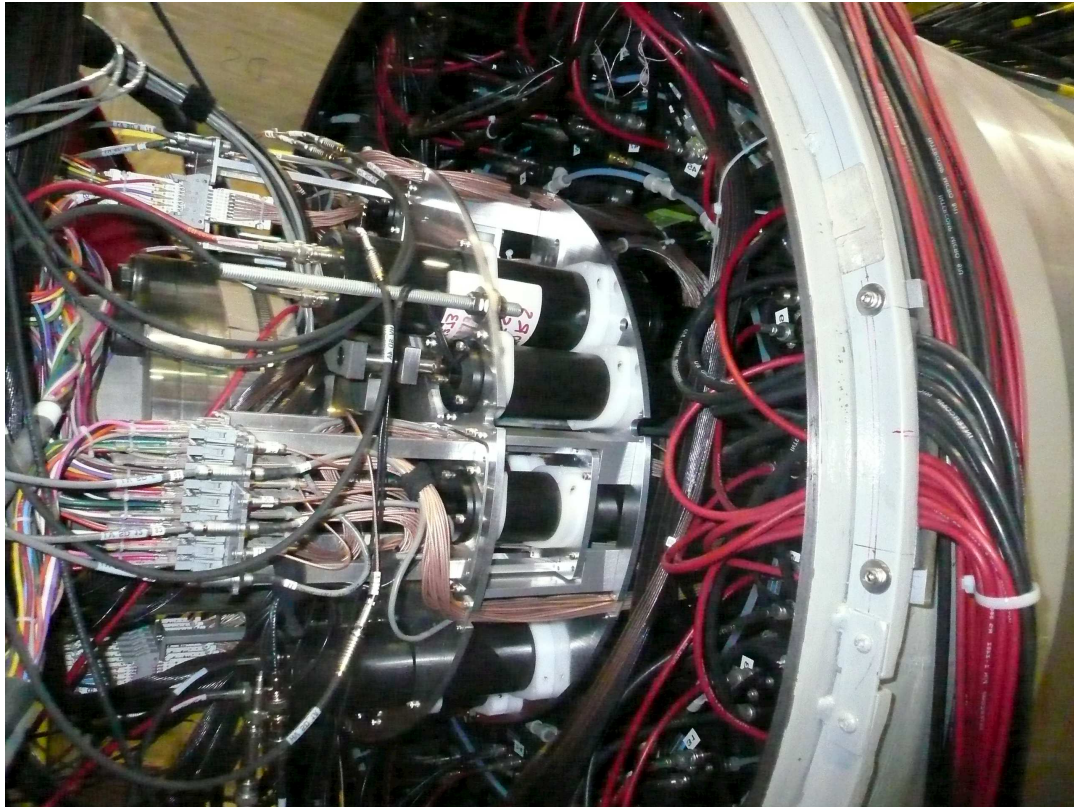


Figure 3.14: Picture of the detector assembly 2



Figure 3.15: Picture of M13 beam channel after detector installation

### 3.3 Trigger diagram

The events needed for the experiment are all  $\pi^+ \rightarrow e^+$  decays and some portion of  $\pi^+ \rightarrow \mu^+ \rightarrow e^+$  decays. In order to realize this, a trigger logic for data taking was built with NIM modules. Fig.3.16 shows the simplified trigger diagram. A coincidence of B1, B2 and Target defines the pion timing and a coincidence of T1 and T2 defines the positron timing. A coincidence of a pion and a positron signal within a time window of -300 ns to 500 ns respect to the pion, make the basis of the trigger. The discriminator threshold of B1 counter is set so as to reject beam positrons and muons. Four kind of triggers are made from the pion and positron coincidence.

- **Early-Trigger**  
The events in which the positron comes within the early time window(2-40 ns) are selected as Early-Trigger.
- **NaI-High-Trigger**  
The events which have high energy deposit in the NaI calorimeter are selected as NaI-High-Trigger.
- **CsI-Hit-Trigger**  
The events which have some hit in CsI crystal are selected as CsI-Hit-Trigger.
- **Pre-scale-Trigger**  
All the events which have the coincidence of a pion and positron are prescaled by a factor of 16 and make Pre-scale-Trigger.

Early-Trigger, NaI-High-Trigger and CsI-Hit-Trigger are for  $\pi^+ \rightarrow e^+$  decays which occur with pion lifetime (26 ns), have high energy deposit in the NaI calorimeter and may have shower leak hit in the CsI calorimeter. Pre-scale trigger is for  $\pi^+ \rightarrow \mu^+ \rightarrow e^+$  decays which has  $10^4$  more events than  $\pi^+ \rightarrow e^+$  decay. The threshold for NaI-High-Trigger is set to 45 MeV and the threshold for CsI-Hit-Trigger is about 5MeV. In addition to these triggers for pion decay, there is also a trigger for beam positron which is mainly used for calibration.

- **Beam-Positron-Trigger**  
Beam positron is pre-scaled by factor of 32 and make Beam-Positron-Trigger.

The rates of the triggers are shown in Table.3.2. It is possible that more than one triggers are issued at the same time. Total trigger rate is about 800 Hz.

Early-Trigger	160Hz
NaI-High-Trigger	170Hz
CsI-Hit-Trigger	270Hz
Pre-scale-Trigger	240Hz
Beam-Positron-Trigger	5Hz

Table 3.2: Rate of each trigger.

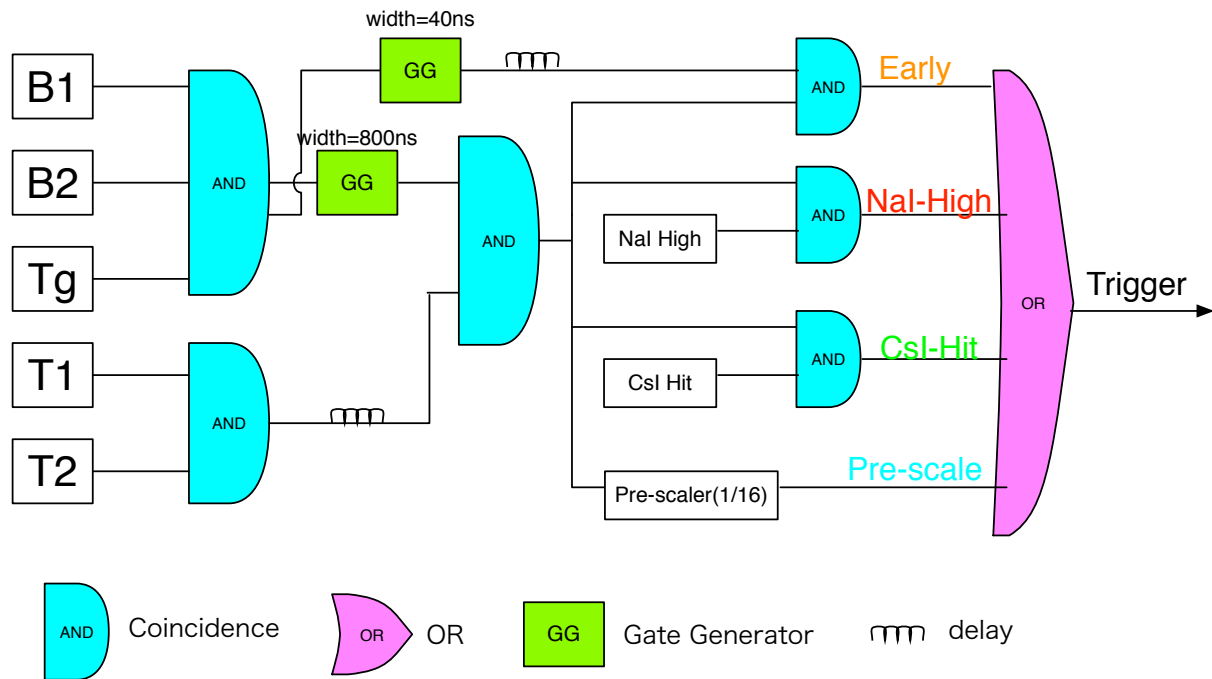


Figure 3.16: Simplified trigger diagram

## 3.4 Data acquisition system

### 3.4.1 Electronics

**COPPER 500-MHz FADC** All the scintillating counter's PMTs are readout by 500-MHz waveform digitizer (FADC). The FADC system is based on the COPPER platform.[16]

The COmmon Pipelined Platform for Electronics Readout (COPPER) was developed by KEK mainly for Belle and experiments at the J-PARC facility. The left picture in Fig.3.17 shows the main board of COPPER. The main board of COPPER is a 9U-size VME board with local extensions specific to COPPER called KEK-VME specification. Each main board has four slots to install front-end modules (FINESSE) for signal digitization, and three PCI mezzanine card (PMC) slots for on-board data processing, triggering and other purposes. The major advantage of the COPPER system is its on-board data processing capability. It can be equipped with a processor board running Linux. Data obtained from the FINESSE modules are transferred to the on-board processor via a high-speed (80 MB/s) internal bus. Data can be processed before they are transmitted to a host computer outside the main board.

The right picture in Fig.3.17 shows the FADC FINESSE module. There are two channels of analog inputs on a single module. Two 250-MHz FADC devices (Fairchild SPT7721SI) are driven in alternating phases in order to realize 500-MHz sampling. This device has a resolution of 8 bits and a dynamic range of 500 mV. According to the specification sheet, the effective number of bits (ENOB) is about 6.5 bits. The non-linearity of the FADC is less than 1%. The dynamic range of the module can be adjusted from a range of -1000~ 0 mV to a range of 0 ~ +1000 mV by an external circuit.

For the PIENU experiment the dynamic range is set -50mV ~ 950 mV and the time window is set -7.8  $\mu$ s to 0 ns with respect to the trigger signal. This wide time window is to detect pre-pile up

particles. Online data reduction is done with the on-board processor. Only FADC sample points which is bigger than a certain threshold (there is some margin before and after the sample which cross the threshold) is sent to the host computer as data. Fig.3.18 shows a waveform of a PMT signal which is taken by the COPPER 500-MHz FADC system. Black circle point and red triangle point shows the data from 2 ADCs. In addition to the scintillating counter's PMT, some other signal are readout with COPPER and in total 32 channels are readout which correspond to 16 FADC FINESSE and 4 COPPER main boards.

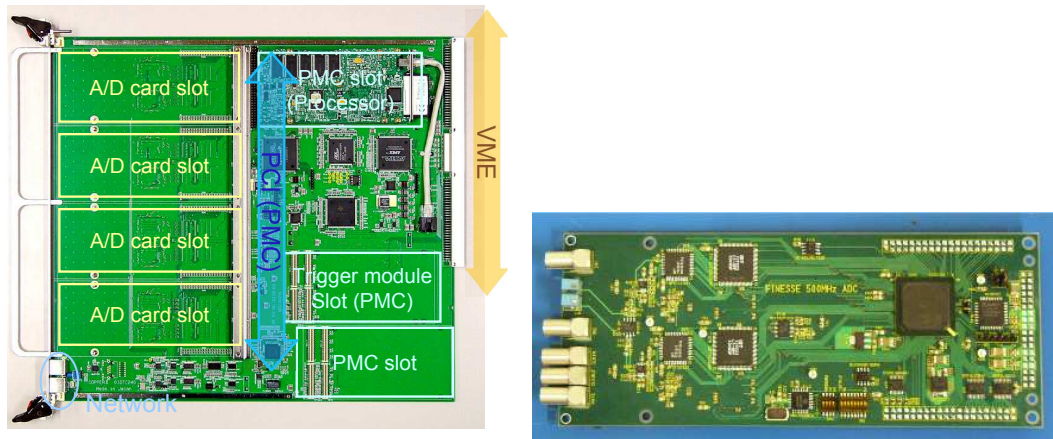


Figure 3.17: Left picture is the COPPER board. Right picture is the 500-MHz FADC daughter card

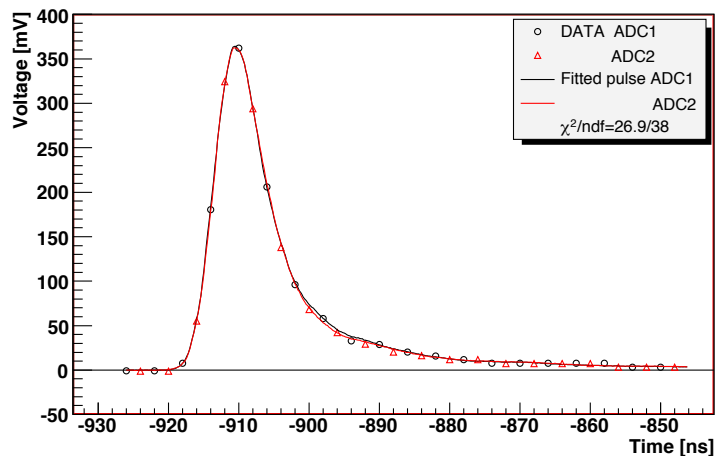


Figure 3.18: Waveform data taken by the COPPER 500-MHz FADC system

**60-MHz FADC (VF48)** All the PMTs of the NaI and CsI calorimeter and all the strips of the silicon strip detector are readout by 60-MHz FADC modules called VF48. This single width VME 6-U module was designed at the University of Montreal in 2004 and is used in various TRIUMF experiments.[18] This device has a resolution of 10 bits and a dynamic range of 250 mV. One board can readout 48 channels and data suppression can be used. The data suppression is implemented with the following

way: If two subsequent samples have pulse height difference higher than a given threshold within a given time window, the full waveform is recorded. If the threshold is not passed, no data is recorded. In total 404 channels (NaI:19, CsI:97, Silicon:288) are readout with 10 VF48 modules. For the NaI calorimeter PMTs, the clock frequency is changed to 30MHz and 40 samples (1300 ns) are recorded. For the CsI calorimeter PMTs, data suppression is used with a threshold of 5 mV and the time window is also 40 samples (664 ns). For the silicon strip detector, data suppression is used with a threshold of 4 mV for S1 and S2 and 3mV for S3 and a time window is 70 samples (1162 ns).

**Multi-hit TDC (VT48)** All the wires of wire chambers and all the logic signal after discriminator module of PMT's signal and some trigger logic signal are readout by multi-hit TDC module called VT48. This single width VME 6-U module was designed at TRIUMF in 2006.[19] The AMT3-chip which is developed for ATLAS[20] is used as a TDC chip on VT48. This device has a resolution of 0.625 ns with 25-MHz on-board clock. One board can readout 48 channels. The time window is set -8.0  $\mu$ s to 0 ns respect to the trigger signal. In total, 11 VT48 modules are used in the experiment.

### 3.4.2 Data acquisition system

The MIDAS data acquisition system is used for the experiment.[21] There are two VME-6U crate for VT48s and VF48s and there is one VME-master module which has a processor with Linux in each crate. There is another VME-9U crate with local extensions specific to COPPER called KEK-VME specification. Four COPPER boards are used and each board have a processor with Linux. In total there are 6 processor with Linux and on each processor the program to transfer the data to the host computer which is called 'Frontend' is running. There is a main MIDAS server computer which collect all the data from each 'Frontend'. The system is controlled by the main MIDAS server with a web interface. Fig.3.19 shows the web interface. Some 'Frontend' which measure slow control variables (high voltage, temperature, etc) are also connected to the main MIDAS server. The program which makes online histograms and the program which check the quality of the data is running continuously and connected to the MIDAS server. All the information and errors from each 'Frontend' are issued on the web page.

## 3.5 Variable extraction from the waveform

### 3.5.1 COPPER 500-MHz FADC

The energy deposit information and timing information is extracted from raw waveform data. The energy deposit information is extracted as a integrated charge of the waveform and the timing information is extracted as the timing of the peak of the waveform. Fig.3.20 shows the definition of these variables. At first, the peak search is done. The definition of the peak is the sample point which is higher than it's neighboring sample points with an absolute pulse height higher than 12 mV. The timing and pulse height of the peak are saved as 'T' and 'PH'. The integrated charge within a narrow (-20 ~ +20 ns) and wide (-20 ~ +80 ns) gate is save as 'Q' and 'Qw'. More than one peak can be found in the waveform and each variable is saved as an array of number of hit. The 'Q' variable is used in the analysis as energy deposit in scintillating counters except Target The 'Qw' variable is used as energy deposit for Target to include the energy deposit of all the decay particles.

MIDAS experiment "pienu"			Thu Nov 19 16:34:12 2009 Refr:60		
Stop Pause ODB CNAF Messages ELog Alarms Programs History Config Help					
monitor					
<a href="#">VME0_settings</a> <a href="#">VME1_settings</a> <a href="#">B1_Setpt</a> <a href="#">B2_Setpt</a> <a href="#">B3_Setpt</a> <a href="#">Shifts</a> <a href="#">Cameras</a> <a href="#">Histos</a> <a href="#">Operators</a> <a href="#">Runlog</a> <a href="#">HV_PIENU</a>					
Run # 25407	Running	Alarms: On	Restart: Yes	Data dir: /home/pienu/online/data	
Start: Thu Nov 19 15:27:03 2009			Running time: 1h07m09s		
Equipment	FE Node	Events	Event rate[/s]	Data rate[MB/s]	Analyzed
Vme0	feVme0@lxdaq07.triumf.ca	83548	8.2	0.045	N/A
Vme1	feVme1@lxdaq06.triumf.ca	83557	8.7	0.097	N/A
Copper1	feCopper01@copper1	83543	8.3	0.004	N/A
Copper2	feCopper02@copper2	83543	8.3	0.005	N/A
Copper3	feCopper03@copper3	83543	8.3	0.004	N/A
Copper4	feCopper04@copper4	83543	8.3	0.007	N/A
EB	Ebuilder@pienu01.triumf.ca	83553	9.9	0.171	N/A
PostAmp	PostAmp@pienu01.triumf.ca	0	0.0	0.000	N/A
u_Beam	fe3hp@pienu01.triumf.ca	0	0.0	0.000	N/A
NMR	fenmr@pienu01.triumf.ca	0	0.0	0.000	N/A
Epics	feepics@pienu01.triumf.ca	0	0.0	0.000	N/A
M13DVM	fem13dvm@pienu01.triumf.ca	0	0.0	0.000	N/A
GASDVM	fegasdvm@pienu01.triumf.ca	0	0.0	0.000	N/A
ScalerN	feScalerN@laddvme03.triumf.ca	0	0.0	0.000	N/A
LRS1440	FeLrs1440@pienusc.triumf.ca	0	0.0	0.000	N/A
RunLog	feRunLog@pienu01.triumf.ca	0	0.0	0.000	N/A
QOD	feqod@pienu02.triumf.ca	0	0.0	0.000	N/A

Figure 3.19: Web interface of the DAQ system

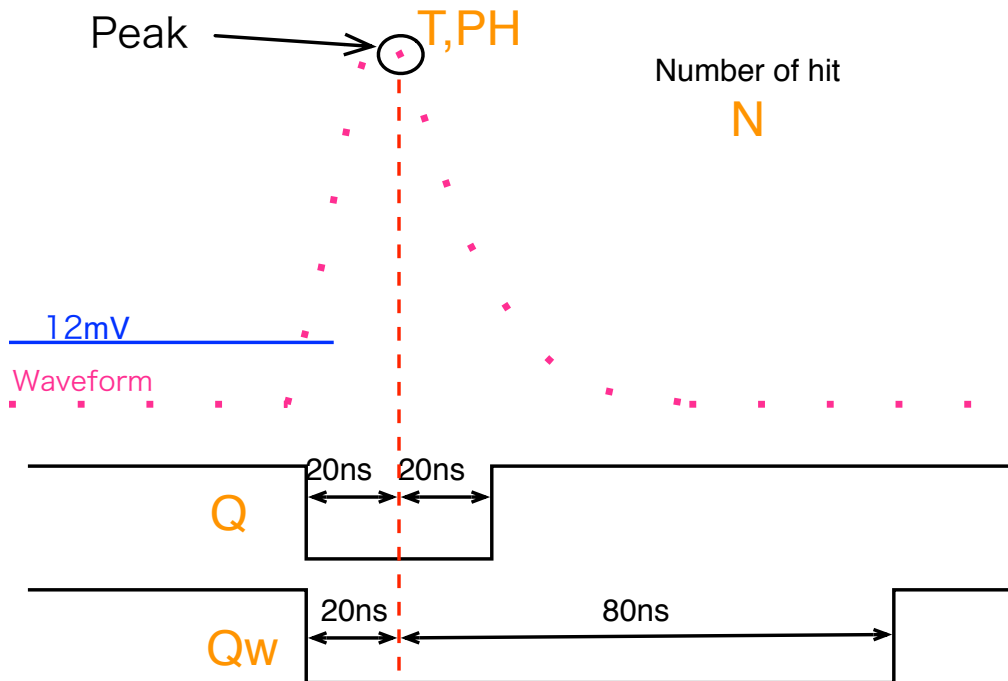


Figure 3.20: Variable extraction from 500-MHz waveform

### 3.5.2 60-MHz FADC (VF48)

Almost the same procedure as 500-MHz FADC is used for the waveform of the 60-MHz FADC. Fig.3.21 shows the definition of the variables. The only difference is the time window which is  $\pm 5$  sample points and the threshold of the hit (NaI:2.5 mV, CsI:10mV, Silicon:1.5 mV). For the NaI crystal PMT's signals, there are different integrated charge variable with fixed timing gate(36 sample) 'Qf'. The timing is fixed from the trigger which have timing of T1 counter and therefore positron timing. The fixed gate charge information 'Qf' is used as energy deposit in the NaI calorimeter in the analysis for this thesis.

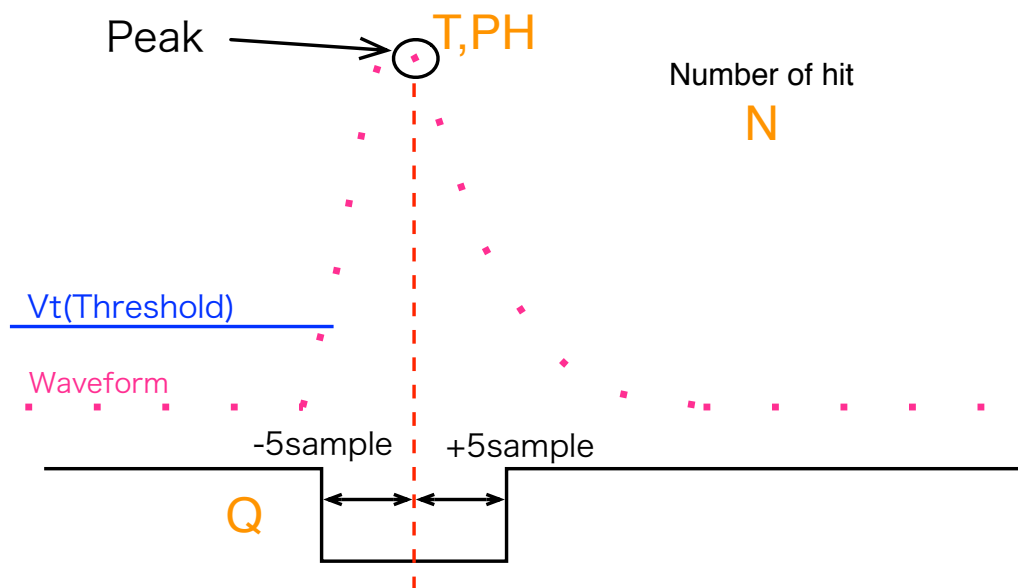


Figure 3.21: Variable extraction from 60-MHz waveform



## Chapter 4

# Pion decay event selection

### 4.1 Data set for analysis and overview of the pion decay event section

#### 4.1.1 Data set for analysis

The data which is taken between June and September, 2009 are used for the analysis of this thesis. The data consists of about 6000 separate runs and each run includes about 380k events. The DAQ rate was about 0.6kHz and each run is 10 minutes long.

#### 4.1.2 Overview of the event selection

In order to get clean pion decay event, some selections are done. First of all, the events which have pileup are rejected to select the events which have only one beam particle coming into the target and only one particle going out of the target toward the telescope counters. Then particle identification by energy deposit and time of flight (TOF) are done after energy calibration of the detectors. Pion decay events are selected with these selections. These event selections are defined on a single run. In order to analyze the full data set, the stability correction of the PMTs gain is done

### 4.2 Energy Calibration

In order to define the cuts with energy deposit in MeV unit and to sum up the energy in each detector, the energy calibration of the scintillating counters, the NaI calorimeter and the silicon strip detectors are done by using 75MeV/c beam positrons.

#### 4.2.1 Scintillating counters

Fig.4.1 shows the charge sum of 4 PMTs of each counter with beam positron. Each PMT's charge is normalized to the charge of the first PMT of the counter. The calibration factor to convert ADC value to MeV is obtained by assuming that the mean value of the histograms is the mean energy deposit of the minimum ionization particle.  $1.93\text{MeV}\cdot\text{cm}^2/\text{g}$  is used as mean energy deposit of minimum ionization particle.[6]

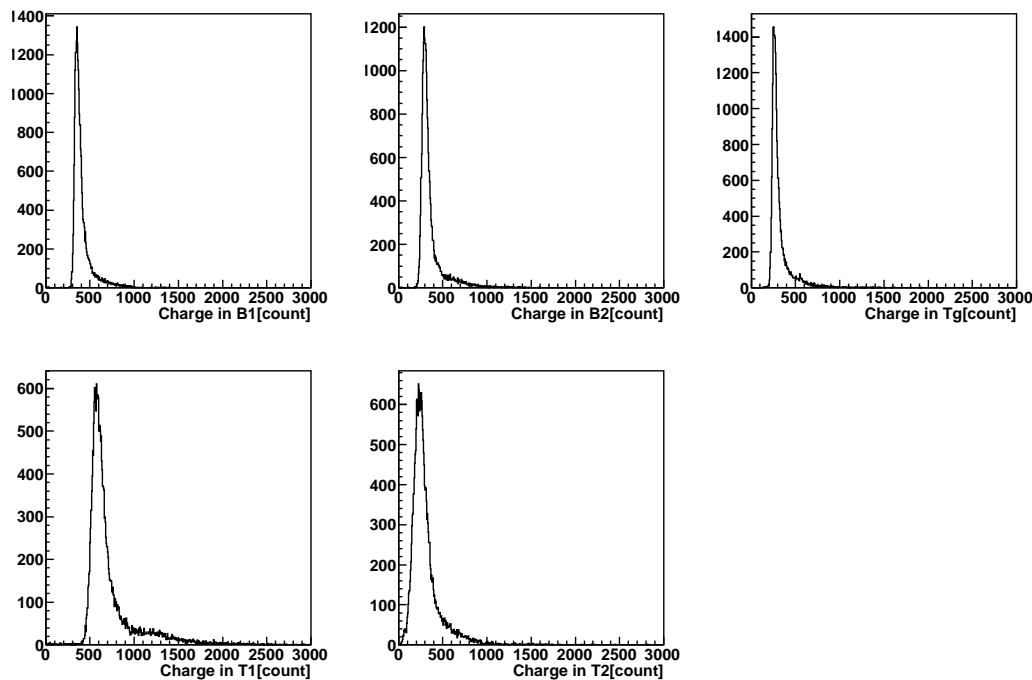


Figure 4.1: Integrated charge of the scintillating counters with beam positron.

#### 4.2.2 NaI calorimeter

Fig.4.2 shows the charge sum of 19 PMTs of the NaI calorimeter with beam positron. Each PMT's charge is normalized to the charge of the first PMT of the calorimeter. The calibration factor to convert ADC value to MeV is obtained by assuming that the peak value of the histograms is 68.4 MeV which is 75 MeV minus the energy deposit in other detectors and some dead material.

#### 4.2.3 Silicon detector

Fig.4.3 shows the charge of 6 silicon planes with beam positron. The calibration factor to convert ADC value to MeV is obtained with the same procedure with the scintillating counters.

#### 4.2.4 Gain stability correction

In order to use the same gain calibration factor for all the runs, the gain stability correction is done. One of the peak in the energy spectrum of each detector is fitted with a Gaussian to obtain the mean value. The stability correction factors are defined as the ratio between the mean value of each run and the that of the reference run. Fig.4.4 shows the energy deposit of B1 and the NaI calorimeter. The spectrum of B1 is after pion selection and the spectrum of NaI calorimeter is with beam positron. The blue line is after stability correction. We can see that the distributions become sharp with the correction.

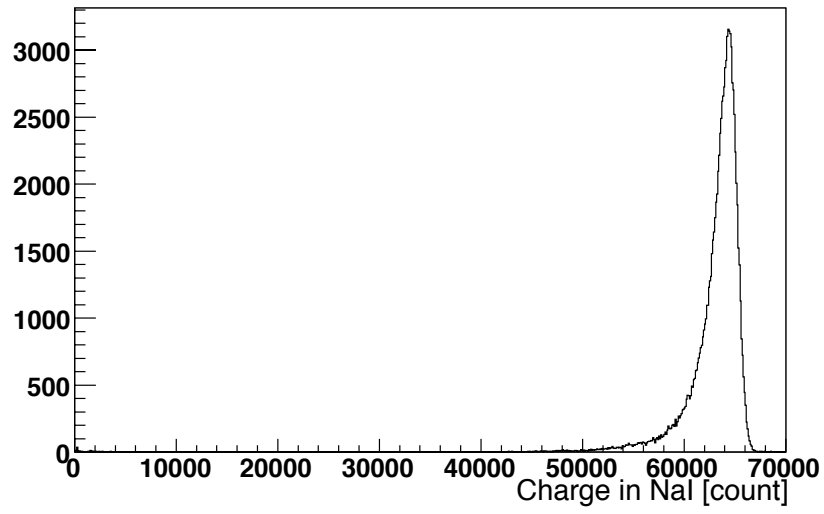


Figure 4.2: Integrated charge of the NaI calorimeter with beam positron.

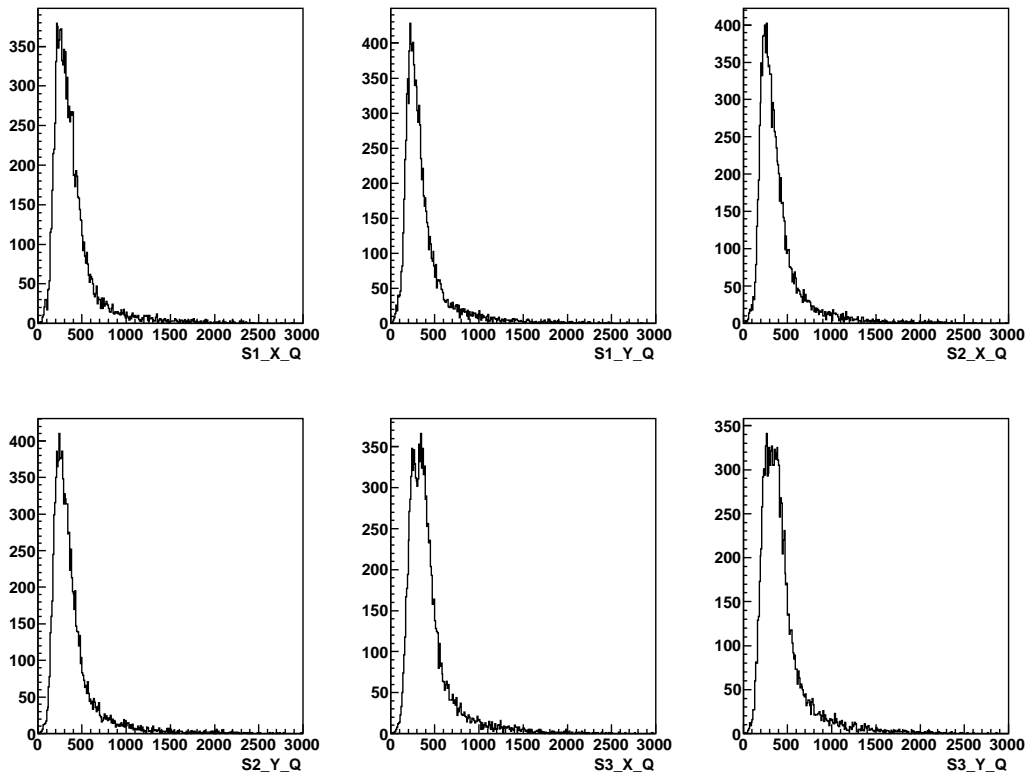


Figure 4.3: Integrated charge of the silicon strip detector with beam positron

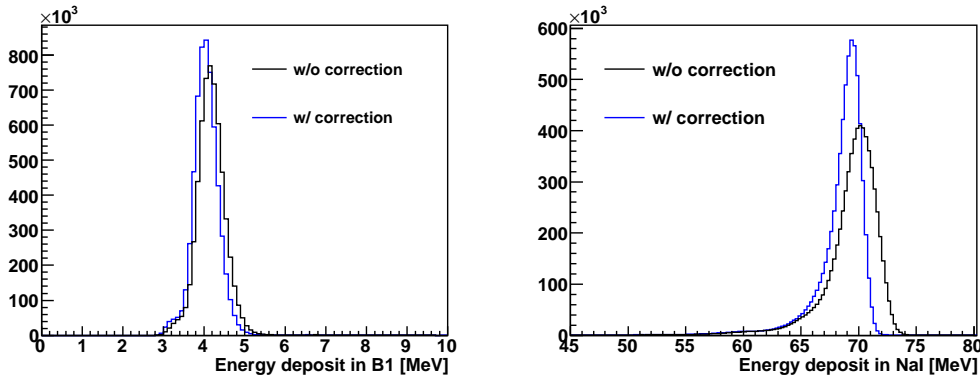


Figure 4.4: Gain stability correction. Left : Energy deposit in B1 with pion selection. Right: Energy deposit in NaI calorimeter with beam positron. The blue line is after gain stability correction.

### 4.3 Pileup rejection

The events which have only one beam particle coming into target and only one particle going out of the target toward the telescope counters should be selected. In order to select that kind of event, the number of hit and the timing consistency of each detectors are used. In this section, the plots shown are after applying the cuts which are defined in the section before.

#### 4.3.1 Number of hit

Fig.4.5 shows the number of hit in the scintillating counters in the beam time window which is  $-2.2\mu\text{s}$  to  $+1.3\mu\text{s}$  with respect to the beam timing. Number of hit is defined by picking up the bump in waveform of each PMT signal as shown in §3.5. For B1, B2 and T1, the event which has only one hit should be selected but sometimes the signals have a second bump even if there is only one real hit due to the fluctuation of the PMT signal. To avoid killing this fake 2 hits events, the events in which one of the 4 PMTs of the counter have only one hit are selected. For the target, there should be 2 hits or 3 hits because it has beam particle and decay particles. One of the 4PMTs has less than 4 hits is used as a cut for the target.

#### 4.3.2 Charge ratio of narrow and wide time window

Fig.4.6 shows the charge ratio of narrow and wide time window in the scintillating counters. Narrow time window is  $-20\text{ ns}$  to  $+20\text{ ns}$  with respect to the peak, and wide gate is  $-20\text{ ns}$  to  $80\text{ns}$ . [§3.5] The ratio should distribute around the certain value if there is no pileup. The cuts are define as the red dashed line in the histograms in Fig.4.6.

#### 4.3.3 Timing consistency of the detector

Events which have only one incoming beam particle and only one going particle from the target are selected with the cuts defined before. Then the timing consistency of each hit should be confirmed. Fig.4.7 shows the time difference between each PMTs of one scintillating counter. They have a quite sharp peak and the cuts are defined as the dashed red line. Fig.4.8 shows the time difference between

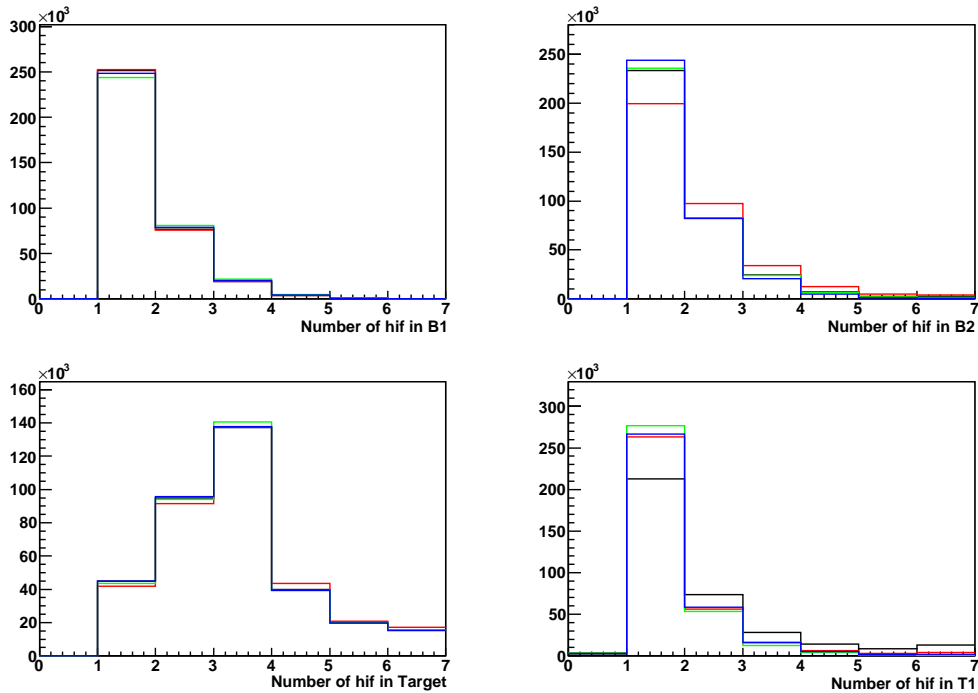


Figure 4.5: Number of hit in the scintillating counter (B1,B2,Tg,T1) in the beam time window. The colors show 4 PMTs for each counter.

each scintillating counter. The left histogram shows difference between B2 and B1 and the right histogram shows time difference of first hit in the target and B1. The cuts are defined as the dashed red lines.

#### 4.3.4 Summary of pileup rejection

In order to reject pileup events, 3 types of cuts are defined and Table.4.1 shows the efficiency of each cut.

Cut	Efficiency	Total efficiency
Number-Of-Hit-Cut	65.4%	65.4%
Q/Qw-Ratio-Cut	99.5%	65.1%
Timing-Consistence-Cut	96.1%	62.6%

Table 4.1: Summary of pileup cut

Fig.4.9 show the time difference between T1 and B1. Before pileup rejection, there are bumps due to beam pileups which have cyclotron RF periodicity (43ns). After the pileup rejection, there are sharp peak at 0ns which is due to fly through beam particle events and the distribution from 0 ns to 500 ns is due to the pion decay chain event  $\pi^+ \rightarrow \mu^+ \rightarrow e^+$  which increase with pion life time and decrease with muon life time. The events which are out of the 2ns  $\sim$  40 ns window are prescaled by factor of 16.[§3.3]

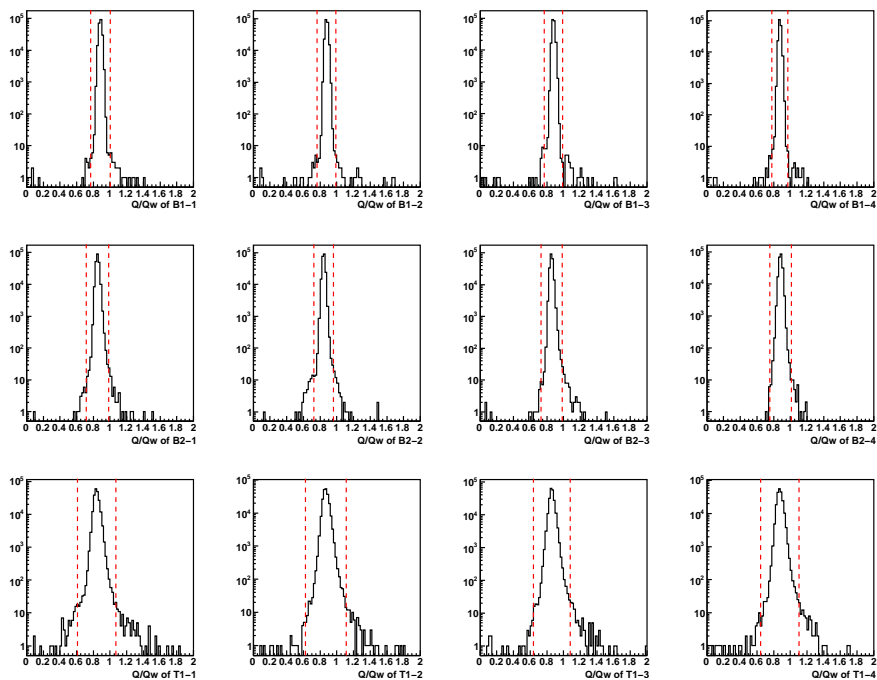


Figure 4.6: Charge ratio of narrow and wide time window in scintillating counters. Red dashed line represent the cut

## 4.4 Pre-pileup rejection

In Fig.4.9 there are some events before 0 ns. This is due to decay positron from muons which stopped before the triggered beam timing. In the target and T1, there are a lot of muons which stay without decaying (Old-Muon). If the Old-Muon decay to positron within the coincidence time window of the triggered beam particle [§3.3], the positron make fake pion decay events. In order to reduce these kind of events the events which have hits before beam timing are rejected. This reduce the number of Old-Muon which stay in the target. Fig.4.10 shows the number of hit in B1 and T1 in the time window from  $-6.5 \mu\text{s}$  to  $-2.2 \mu\text{s}$  with respect to the triggered beam timing. The events which have hit in the time window are rejected. Fig.4.11 shows the time spectrum with the Pre-pileup rejection. The efficiency of the cut is summarized below.

Cut	Efficiency	Total efficiency
Pre-Pileup-Cut	76.7%	48.0%

Table 4.2: Summary of pre-pileup cut

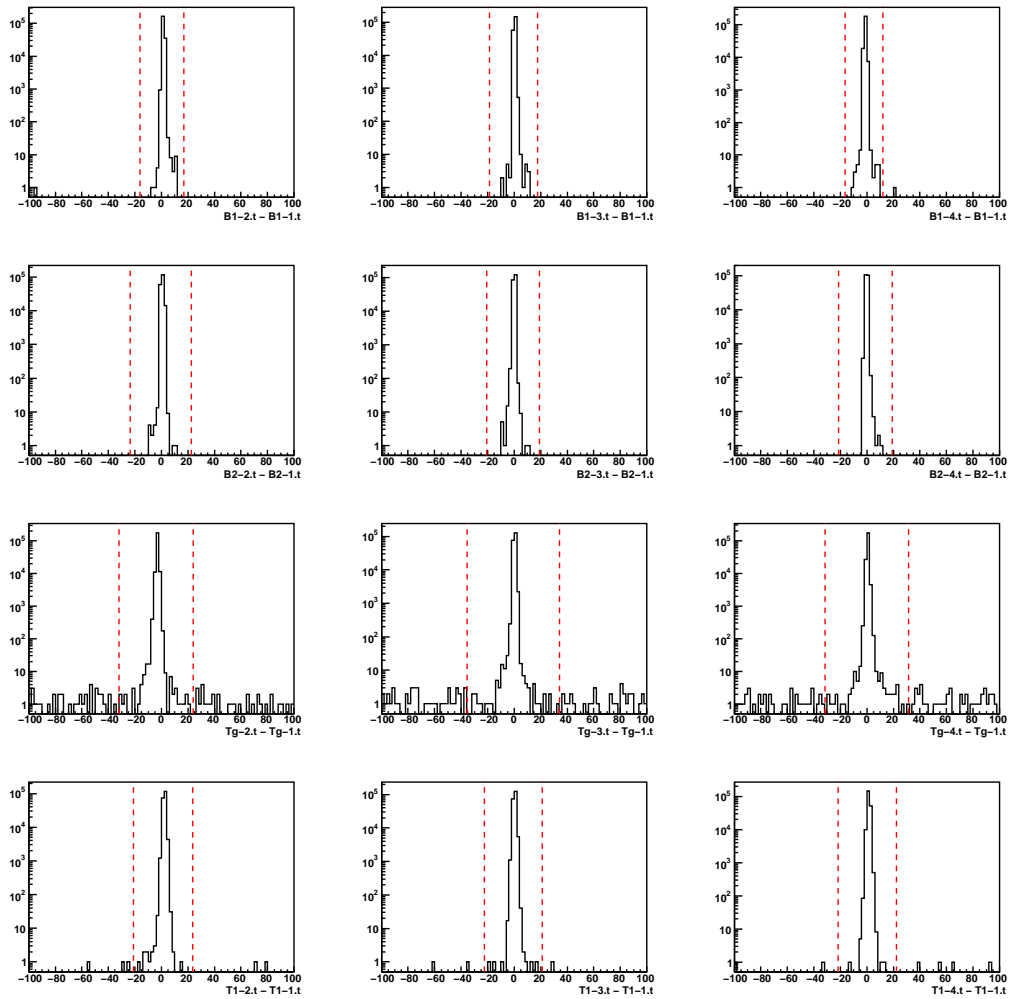


Figure 4.7: Timing difference between the hit in each PMTs of scintillating counters B1, B2, Target and T1.

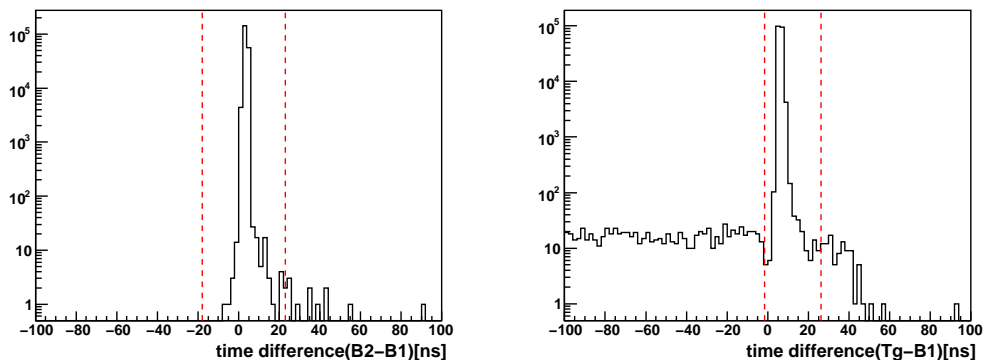


Figure 4.8: Timing difference between the hits in each scintillating counter. Left:Time difference between B2 and B1. Right:Time difference between first hit in target and B1 hit.

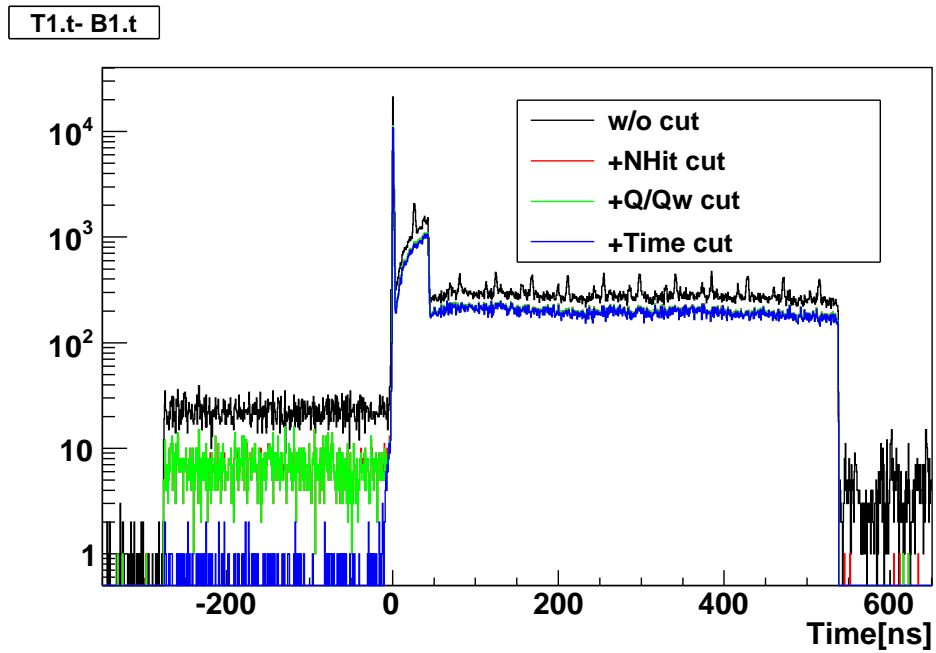


Figure 4.9: Timing spectrum with pileup rejection. Black:without cut. Red:with number of hit cut. Green:with charge ration cut. Blue:Timing consistency cut. Efficiency with all the pileup cuts is 57%

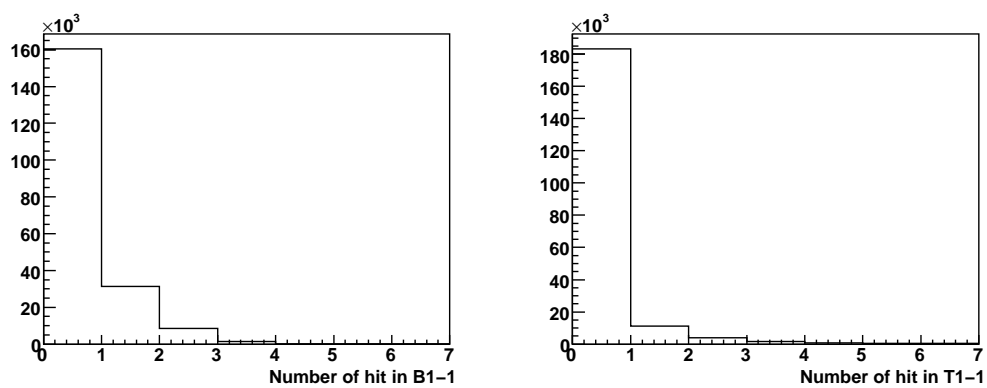


Figure 4.10: Number of hit in B1 and T1 in the time window from  $-6.5 \mu\text{s}$  to  $-2.2 \mu\text{s}$  with respect to the triggered beam timing.

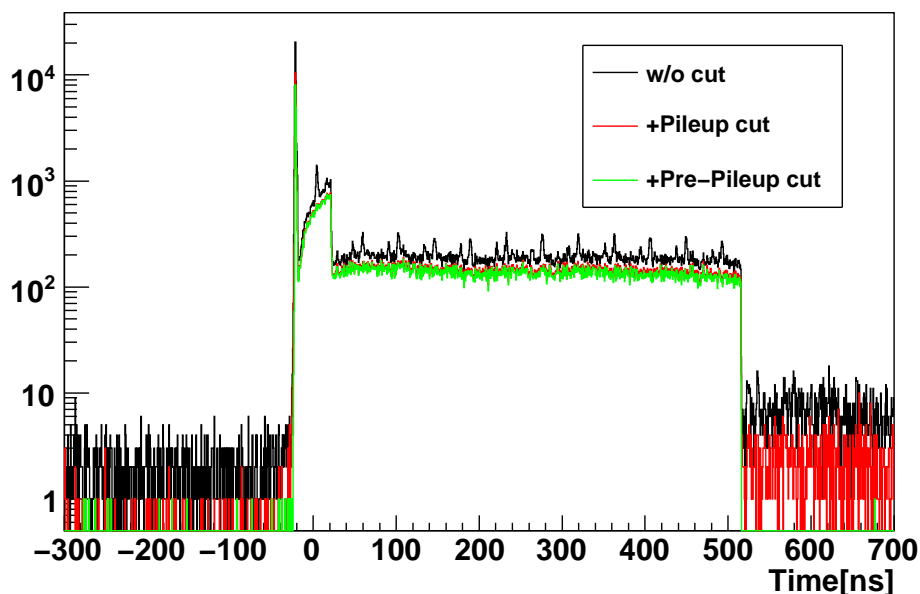


Figure 4.11: Timing spectrum with pre-pileup rejection. Black:without cut. Red:with pileup rejection. Green:with pileup and pre-pileup rejection.

## 4.5 Pion selection

### 4.5.1 Energy deposit and time of flight

Fig.4.12 shows the energy deposit in the beam counters and the time of flight (TOF). The top left figure shows the energy deposit in B2 counter. The first peak of the histogram is due to muons and the second peak is due to pions. The bottom left figure shows the scatter plot between B1 and B2 energy deposit. There is a strong correlation and the red box shows the cut for pion selection. The events which have less than 3MeV in B1 are cut by hardware trigger.[§3.3]

The top right figure shows the TOF which is time difference between cyclotron RF and the B1 hit. The time difference is taken modulo with 43.3ns because the RF has 43.3ns periodicity. There are 3 peak, however it is impossible to know which peak is which particle because this TOF is a modulo. The bottom right figure shows a 2-dimensional histogram of the TOF versus the energy deposit in B2. From the plot, it is clear that first peak in the TOF is pion, the second peak is positron and the third peak is muon. The red box in the plot shows the cut for pion selection. The blue line in TOF 1-dimensional histogram shows the events after the energy deposit cut. This shows that contamination of beam positron and muon after the pion selection cut is less than 0.01%

### 4.5.2 Proton rejection

Most of the beam pions which hit the target, stop and decay to muons or positrons through weak interaction. However, some of them have strong interaction with the nucleus and kick out a proton. The proton could have a broad energy distribution and may become a source of background. However, this proton have a large energy deposit in detectors which are downstream of the target while positrons

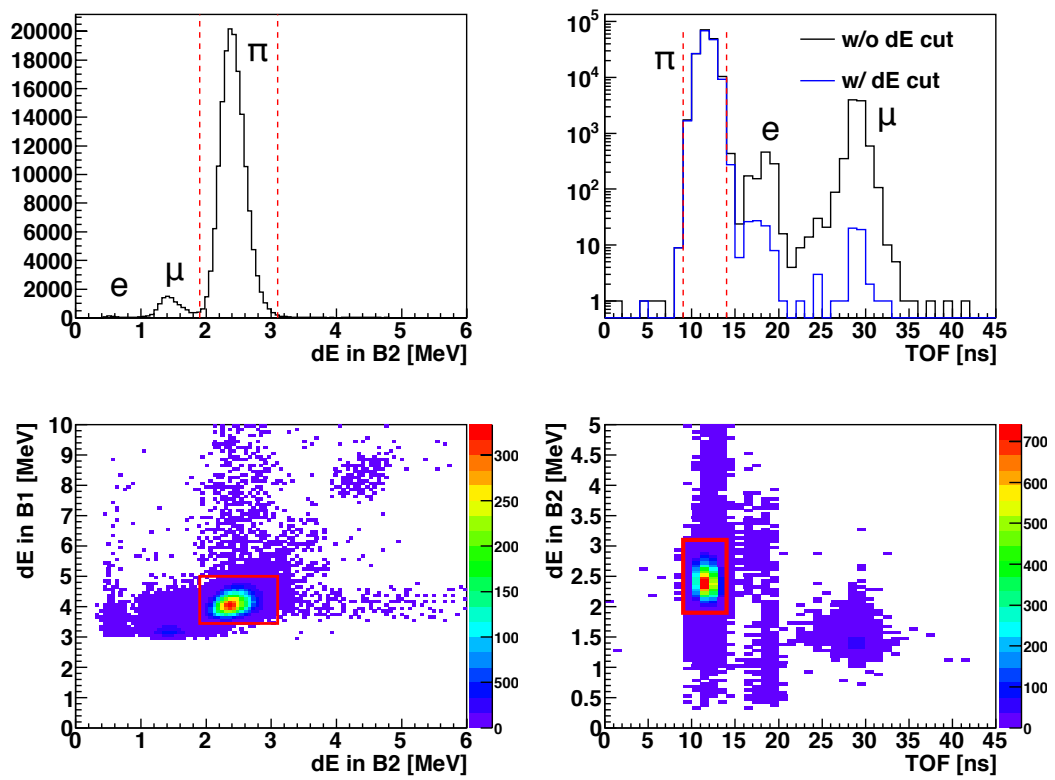


Figure 4.12: Energy deposit in B1 &amp; B2 and TOF.

from pion decay have a small energy deposit. Fig.4.13 shows a 2-dimensional histogram of the energy deposit in the NaI crystal and the minimum  $dE/dX$  in the downstream detectors S3-X,S3-Y,T1 and T2. There is a band due to proton above the dashed red line. The line is the cut for proton rejection.

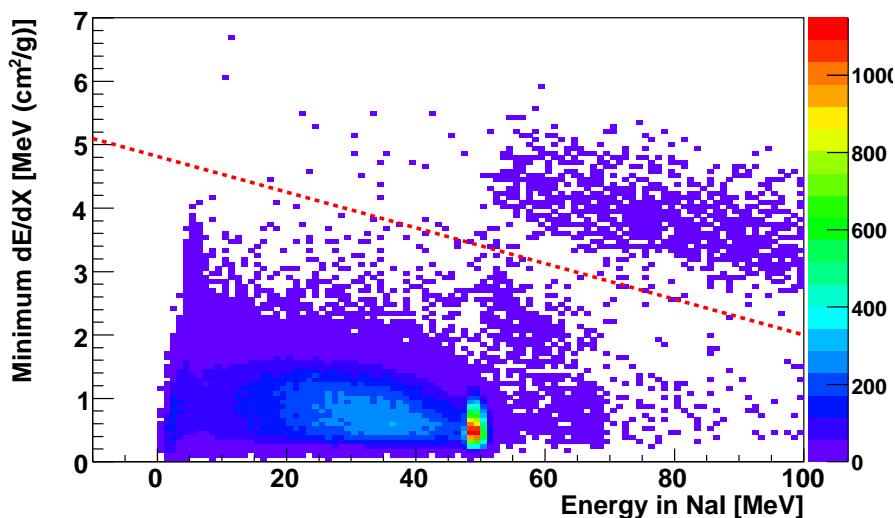


Figure 4.13: Energy deposit in the NaI calorimeter vs minimum energy deposit in downstream detectors. The red dashed line shows the cut for proton rejection.

### 4.5.3 Beam profile selection

Fig.4.14 shows the beam profile at WC1. The red box shows the cut.

### 4.5.4 Summary of pion selection

Fig.4.15 shows time spectrum with pion selection cuts. Almost all the events which are not pion are prompt events ( $t=0$ ). With pion selection cut, the prompt event reduced by a factor 10. the efficiency of the pion selection cuts are below.

Cut	Efficiency	Total efficiency
dE-TOF-Cut	91.0%	43.7%
Proton-Cut	99.1%	43.3%
Beam-Profile-Cut	96.5%	41.8%

Table 4.3: Summary of pion selection cut

## 4.6 Summary of pion decay event selection

Fig.4.16 shows the time spectrum with pion decay selection cuts which were defined in this section. The cuts are summarized below.

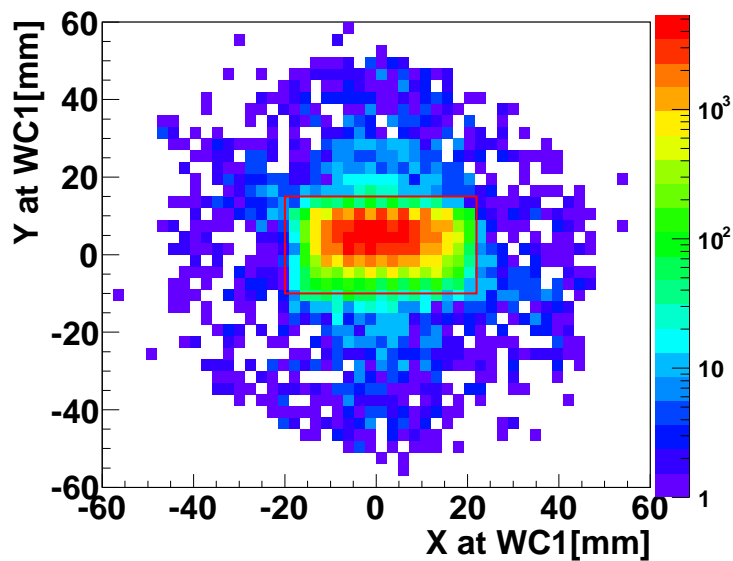


Figure 4.14: Beam profile at WC1. Red box shows the cut.

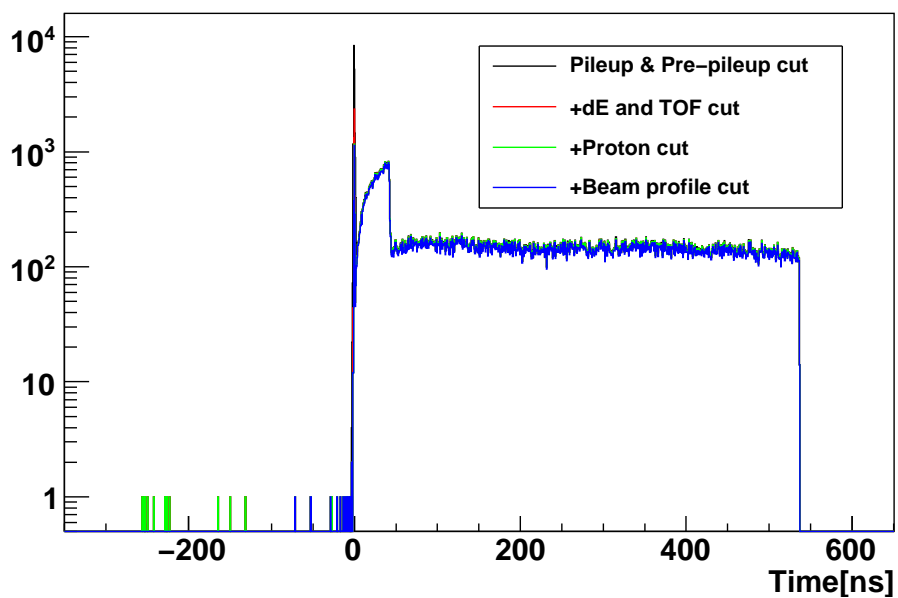


Figure 4.15: Time spectrum with pion selection cuts. Black:Pileup & Pre=pileup Cut. Red:+energy deposit & TOF cut. Green:Proton cut. Blue:Beam profile cut.

Cut	Efficiency	Total efficiency
Pileup-Cut		
Number-Of-Hit-Cut	65.4%	65.4%
Q/Qw-Ratio-Cut	99.5%	65.1%
Timing-Consistence-Cut	96.1%	62.6%
Pre-Pileup-Cut	76.7%	48.0%
Pion-Selection-Cut		
dE-TOF-Cut	91.0%	43.7%
Proton-Cut	99.1%	43.3%
Beam-Profile-Cut	96.5%	41.8%

Table 4.4: Summary of pion decay event selection.

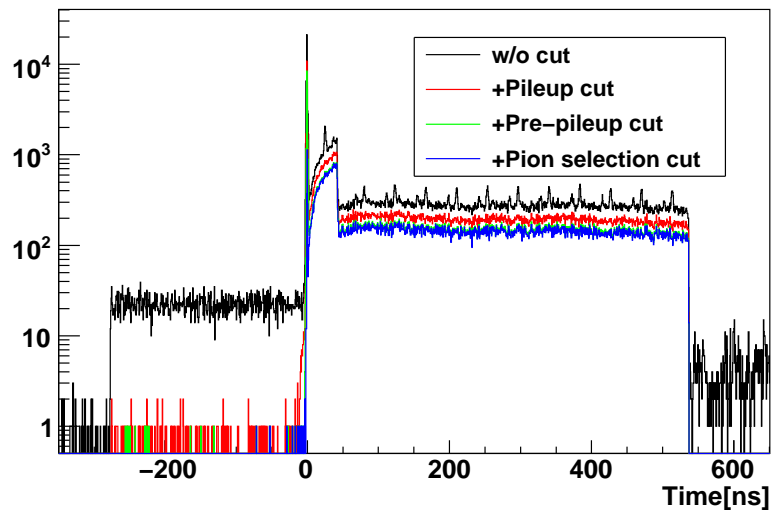


Figure 4.16: Time spectrum with pion decay selection. Black:no cut Red:+Pileup cut. Green:Pre-pileup cut, Blue: Pion selection cut.

Fig.4.17 shows the time spectrum after the pion decay event selection. The red line shows the spectrum in which prescaled factor [§3.3] are taken into account. Almost all the events are  $\pi^+ \rightarrow \mu^+ \rightarrow e^+$  decay chain which increase with pion life time and decrease with muon life time. And it includes some tiny bit of  $\pi^+ \rightarrow e^+ \nu$  decay. In the next chapter,  $\pi^+ \rightarrow e^+ \nu$  decay events are extracted from these events.

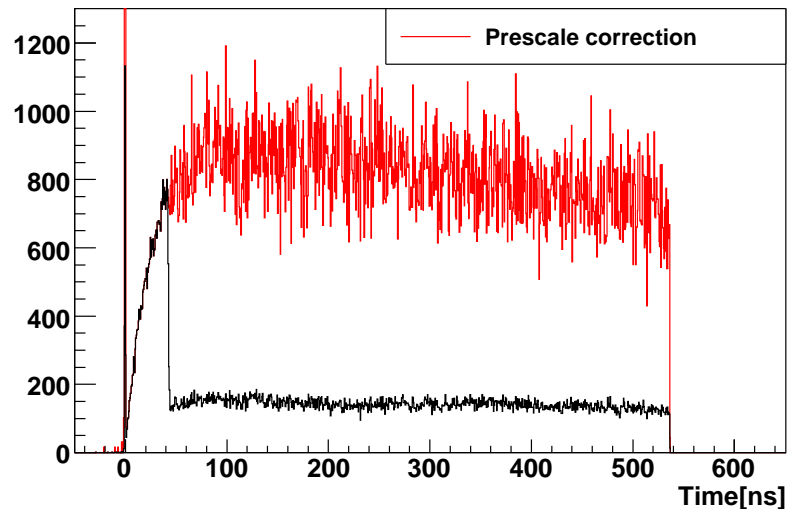


Figure 4.17: Time spectrum with and without pre-scale correction

## Chapter 5

# $\pi^+ \rightarrow e^+ \nu$ event selection

### 5.1 Purpose of this section

The pion decay events are selected as described in Chapter 4 and these pions mostly decay with the 2 processes,  $\pi^+ \rightarrow e^+ \nu_e$  and  $\pi^+ \rightarrow \mu^+ \rightarrow e^+$  as described in §2.2. In order to search massive neutrinos with the positron energy spectrum of the  $\pi^+ \rightarrow e^+ \nu$  decay,  $\pi^+ \rightarrow \mu^+ \rightarrow e^+$  decay events need to be suppressed.

The left histogram in Fig5.1 shows the positron energy spectrum in the NaI crystal within the early time window (2ns-33ns) The energy deposit includes energy deposit in T1, T2 and S3. The positrons from  $\pi^+ \rightarrow e^+ \nu_e$  decay have a monochromatic energy of 70 MeV while the positrons from  $\pi^+ \rightarrow \mu^+ \rightarrow e^+$  decay have a broad distribution from 0 to 53 MeV The red dashed line is the threshold to separate these decay mode. The time spectra in Fig.5.2 are produced with this threshold. The left figure in Fig5.2 shows the time spectrum of the events which have more than 52MeV in the NaI calorimeter. These events are mainly  $\pi^+ \rightarrow e^+ \nu_e$  decay. Right figure in Fig5.2 shows the time spectrum of the events which have less than 52MeV in the NaI calorimeter. These events are mainly  $\pi^+ \rightarrow \mu^+ \rightarrow e^+$  decay.

The purpose of this chapter is to make a positron energy spectrum of  $\pi^+ \rightarrow e^+ \nu$  with high  $\pi^+ \rightarrow \mu^+ \rightarrow e^+$  suppression. In order to obtain the best sensitivity in massive neutrino search, the variable 'S' should be minimize as described in §2.3

$$S = \sqrt{N_{<52MeV}/N_{>52MeV}} \quad (5.1)$$

$N_{<52MeV}$  is the number of events below 52MeV which corresponds to the number of background events.  $N_{>52MeV}$  is the number of event above 52MeV which corresponds to the number of  $\pi^+ \rightarrow e^+ \nu_e$  events. The time window is set from 2 ns to 33 ns to minimize 'S' from now on. In order to suppress  $\pi^+ \rightarrow \mu^+ \rightarrow e^+$  decay event without using the positron energy, the energy deposit in the target is used.  $\pi^+ \rightarrow \mu^+ \rightarrow e^+$  decay events have a extra 4.1 MeV energy deposit due to muons. The right figure in 5.1 shows the energy deposit in the target with the early time window (2 ns-33 ns) The energy deposit includes energy deposit in B1, B2, S1 and S2 and this variable is called 'Total-Energy'. [§2.2] There is a peak due to  $\pi^+ \rightarrow e^+ \nu$  decay at 15.6 MeV. Fig.5.3 shows the positron energy spectrum after applying the Total-Energy cut which is shown as blue dashed line in Fig.5.1.  $\pi^+ \rightarrow \mu^+ \rightarrow e^+$  events are suppressed by 2 orders of magnitude. However, there are still some  $\pi^+ \rightarrow \mu^+ \rightarrow e^+$  event left.

The events which are left in the spectrum consists of 2 kind of events.

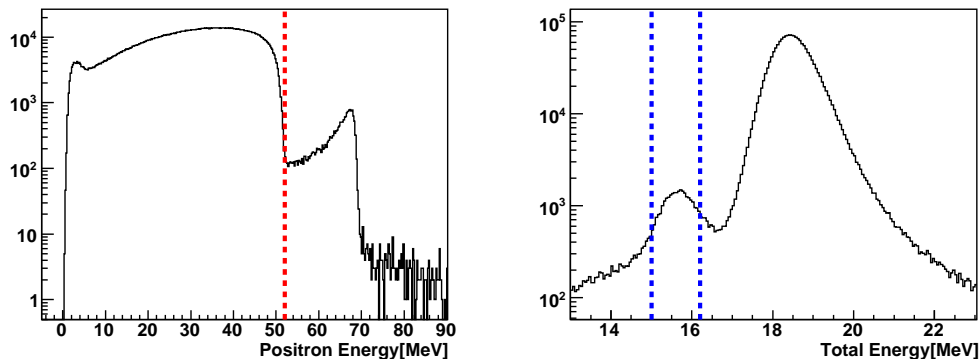


Figure 5.1: Left: Positron energy spectrum with the NaI calorimeter in the early time window (2 ns-33 ns). Right: Total-Energy in the early time window (2 ns-33 ns).

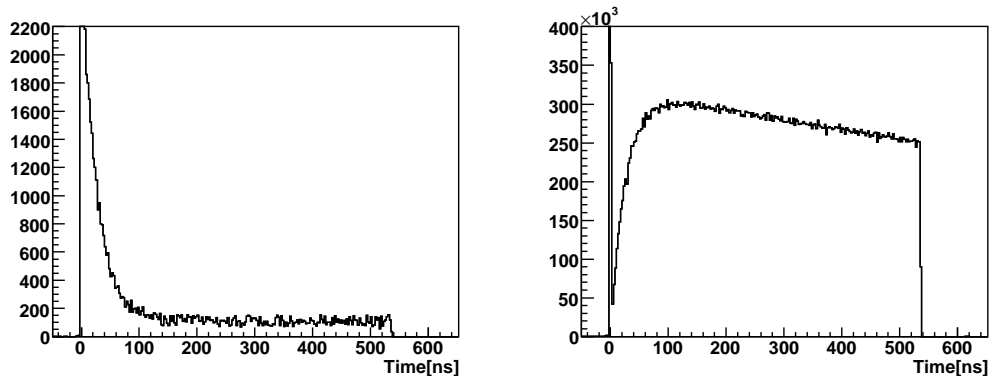


Figure 5.2: Left: Time spectrum of the events above 52 MeV in Fig.5.1. Right: Time spectrum of the events below 52 MeV in Fig.5.1.

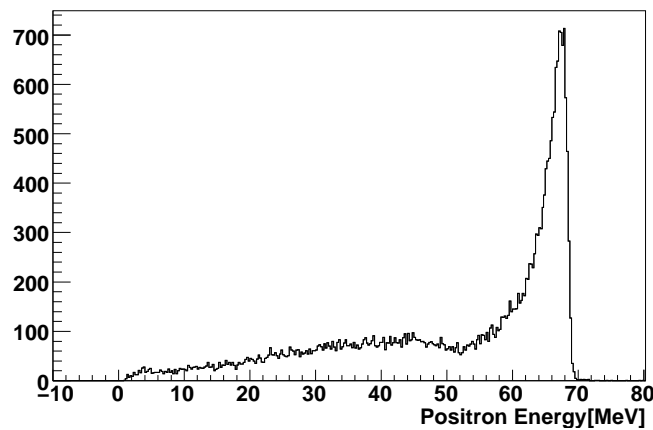


Figure 5.3: Positron energy spectrum with Total-Energy-Cut

- $\pi^+ \rightarrow \mu^+ \rightarrow e^+$  decay which are not suppressed by the cut.
- low energy tail of  $\pi^+ \rightarrow e^+\nu_e$  decay

In order to get more suppression of  $\pi^+ \rightarrow \mu^+ \rightarrow e^+$  events, tracking cut and pulse shape cut will be used. Before selecting  $\pi^+ \rightarrow e^+\nu$  events, some cuts are applied in addition to the pion decay selection cut in Chapter 4. One is the selection of the events which have at least one hit in S3 to be able to use tracking information although the efficiency of the S3 is about 90% for beam positrons. [§??] CsI Veto and WC3 fiducial cut (radius at WC3 < 80mm) are also applied to reduce the low energy tail of  $\pi^+ \rightarrow e^+\nu_e$ . Below is a summary of the cuts which is used in the analysis from now on.

Cut	Efficiency	Total efficiency
Pileup-Cut		
Number-Of-Hit-Cut	65.4%	65.4%
Q/Qw-Ratio-Cut	99.5%	65.1%
Timing-Consistence-Cut	96.1%	62.6%
Pre-Pileup-Cut	76.7%	48.0%
Pion-Selection-Cut		
dE-TOF-Cut	91.0%	43.7%
Proton-Cut	99.1%	43.3%
Beam-Profile-Cut	96.5%	41.8%
Early-Time-Window-Cut	14%	5.9%
S3-Hit-Cut	90%	5.3%
CsI-Veto-Cut	89%	4.7%
Fiducial-Cut	81%	3.8%

Table 5.1: Summary of the cuts before  $\pi^+ \rightarrow e^+\nu$  event selection.

In order to estimate the  $\pi^+ \rightarrow \mu^+ \rightarrow e^+$  suppression capability of each cut,  $\pi^+ \rightarrow e^+\nu_e$  events sample and  $\pi^+ \rightarrow \mu^+ \rightarrow e^+$  events sample is produced with positron energy information. More than 52 MeV is used for  $\pi^+ \rightarrow e^+\nu_e$  events selection and less than 30 MeV is used for  $\pi^+ \rightarrow \mu^+ \rightarrow e^+$  events selection. The reason why the threshold for  $\pi^+ \rightarrow \mu^+ \rightarrow e^+$  sample is set to 30 MeV is to reduce the low energy tail of  $\pi^+ \rightarrow e^+\nu$  events.

The left figure in Fig.5.4 shows Total-Energy of  $\pi^+ \rightarrow e^+$  and  $\pi^+ \rightarrow \mu^+ \rightarrow e^+$  sample with full statistics. There are a lot of  $\pi^+ \rightarrow \mu^+ \rightarrow e^+$  events in the  $\pi^+ \rightarrow e^+$  peak region. The right figure in Fig.5.4 is the positron energy with the Total-Energy-Cut shown as dashed purple line in the left histogram in Fig.5.4. The cut is defined to keep 90% of  $\pi^+ \rightarrow e^+\nu_e$  events. In this figure,  $N_{<52MeV}/N_{>52MeV} = 40\%$ . In this section, the cuts for  $\pi^+ \rightarrow \mu^+ \rightarrow e^+$  suppression optimized to minimize 'S' are described. Total-Energy-Cut which is shown in the left figure in Fig.5.4 is applied for the suppression cut study from now on.

- Total-Energy-Cut      14.9 MeV < Total-Energy < 16.3 MeV

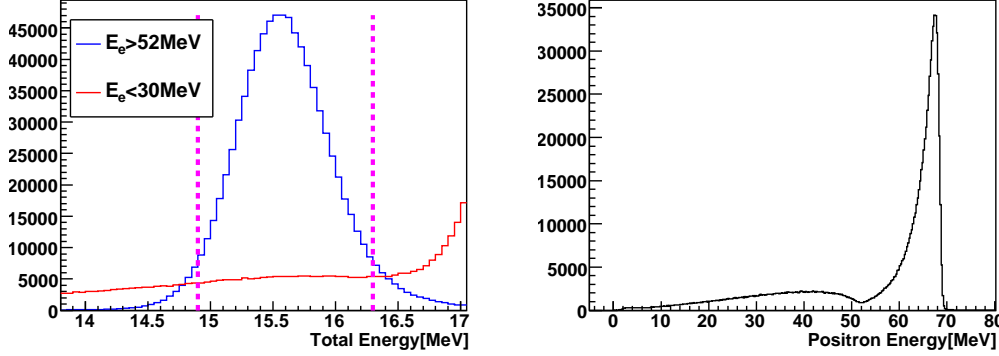


Figure 5.4: Left: Total-Energy spectrum. Right: Positron energy spectrum with Total-Energy-Cut

## 5.2 Tracking cut

### 5.2.1 Incident angle cut

The biggest source of  $\pi^+ \rightarrow \mu^+ \rightarrow e^+$  events left after Total-Energy-Cut, seems to be pion-decay-in-flight event in which the pion decay to muon before the target and the muon stop in the target and decay to positron ( $\pi$ DIF-us). [§2.5] The muon energy deposit in target can be the same as the pion energy deposit in  $\pi^+ \rightarrow e^+\nu$  decay. However, the muon which can stopped in the target and have the same energy as pion has an angle about  $30^\circ$ . That is why the angle of the incident particle in the target can discriminate  $\pi$ DIF-us events and  $\pi^+ \rightarrow e^+\nu$  decay. The incident angle is calculated from the X-Y information of S1 and S2 detector with the equation below.

$$Angle = \tan^{-1}\left(\sqrt{(X_{s2} - X_{s1})^2 + (Y_{s2} - Y_{s1})^2} / (Z_{s2} - Z_{s1})\right) \quad (5.2)$$

Fig.5.5 shows the angle of the incoming particle to the target which is obtained with S1 and S2 detector. The blue line shows  $\pi^+ \rightarrow e^+\nu$  decay sample and the red line shows  $\pi^+ \rightarrow \mu^+ \rightarrow e^+$  decay sample.  $\pi^+ \rightarrow \mu^+ \rightarrow e^+$  events have a bump around  $30^\circ$ . These are the events in which pion decay before the S2 detector.  $\pi^+ \rightarrow \mu^+ \rightarrow e^+$  events in which pion decays after S2 detector cannot be suppressed with this cut. The dashed purple line shows the cut which keep 90% of  $\pi^+ \rightarrow e^+\nu$  events.

### 5.2.2 Vertex cut

In order to get more suppression of  $\pi^+ \rightarrow \mu^+ \rightarrow e^+$  events, the decay vertex reconstruction is done with the beam tracks obtained by S1 & S2 and the positron tracks obtained by S3 & WC3. In  $\pi^+ \rightarrow e^+\nu$  decay case, the vertex reconstruction should work because there is no intermediate particle between the beam pion and the decay positron. However, the vertex reconstruction may have wrong results if the events have intermediate muons. Thus, the vertex information can detect  $\pi^+ \rightarrow \mu^+ \rightarrow e^+$  events which occur after S2. The minimum distance (Rmin) of 2 tracks and the Z position (beam axis) at the point (Zmin) is calculated from the X-Y information from tracking detectors with equations below.  $A_i$  and  $B_i$  are the parameter of the pion tracks and  $C_i$  and  $D_i$  are the parameter of the positron tracks. Fig.5.6 shows Rmin and Zmin of 2 decay mode samples. The dashed purple line shows the cut which keep 90% of  $\pi^+ \rightarrow e^+\nu$  events.

$$x = A_1 \cdot z + B_1 \quad (5.3)$$

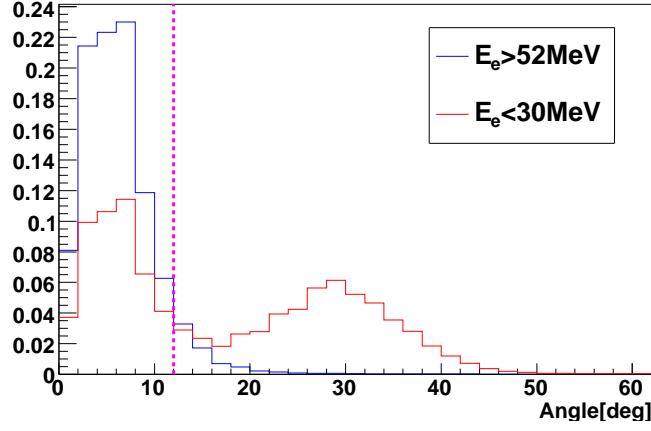


Figure 5.5: Angle of the incoming particle to the target. Blue line shows  $\pi^+ \rightarrow e^+$  sample. Red line shows  $\pi^+ \rightarrow \mu^+ \rightarrow e^+$  sample

$$y = A_2 \cdot z + B_2 \quad (5.4)$$

$$A_1 = (X_{s2} - X_{s1}) / (Z_{s2} - Z_{s1}) \quad (5.5)$$

$$B_1 = X_{s1} - A_1 \cdot Z_{s1} \quad (5.6)$$

$$A_2 = (Y_{s2} - Y_{s1}) / (Z_{s2} - Z_{s1}) \quad (5.7)$$

$$B_2 = Y_{s1} - A_2 \cdot Z_{s1} \quad (5.8)$$

$$x = C_1 \cdot z + D_1 \quad (5.9)$$

$$y = C_2 \cdot z + D_2 \quad (5.10)$$

$$C_1 = (X_{wc3} - X_{s3}) / (Z_{wc3} - Z_{s3}) \quad (5.11)$$

$$D_1 = X_{s3} - C_1 \cdot Z_{s3} \quad (5.12)$$

$$C_2 = (Y_{wc3} - Y_{s3}) / (Z_{wc3} - Z_{s3}) \quad (5.13)$$

$$D_2 = Y_{s3} - C_2 \cdot Z_{s3} \quad (5.14)$$

$$dX = X_1 - X_2 \quad (X = A, B, C, D) \quad (5.15)$$

$$Zmin = -1 \cdot \frac{dA \cdot dB + dC \cdot dD}{dA^2 + dC^2} \quad (5.16)$$

$$Rmin = (dA^2 + dC^2)Zmin^2 + 2(dAdB + dCdD)Zmin + dB^2 + dD^2 \quad (5.17)$$

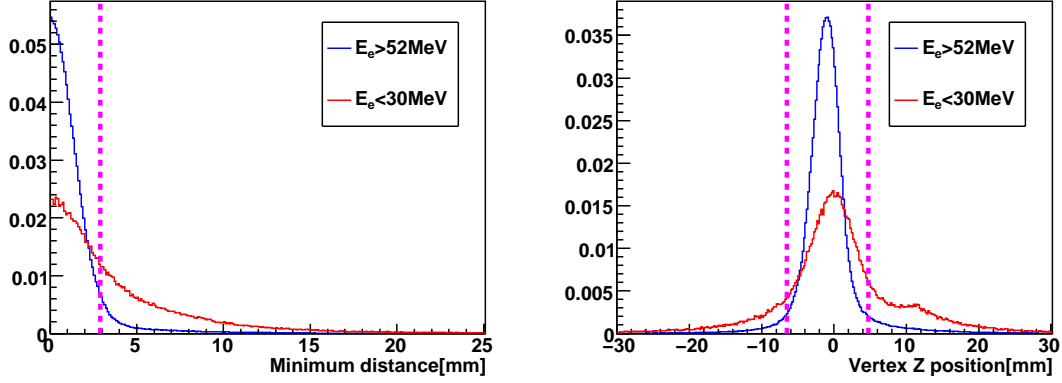


Figure 5.6: Decay vertex information from tracking. Left: Minimum distance of vertex (Rmin). Right: Z-position of the vertex (Zmin). Blue line is  $\pi^+ \rightarrow e^+\nu$  sample and Red line is  $\pi^+ \rightarrow \mu^+ \rightarrow e^+$  sample

### 5.3 Pulse shape cut

$\pi^+ \rightarrow \mu^+ \rightarrow e^+$  decay events have 3 pulses in the target PMT while  $\pi^+ \rightarrow e^+\nu$  decay events have only 2 pulses. Thus, by analyzing the shape of the target PMT signal waveforms which are read out by 500-MHz FADC [3.4.1], one can discriminate  $\pi^+ \rightarrow e^+\nu$  decay and  $\pi^+ \rightarrow \mu^+ \rightarrow e^+$  decay. DIF events cannot be identified with the pulse shape because the DIF events have only 2 pulses like  $\pi^+ \rightarrow e^+\nu$  decay events. To distinguish whether there are 2 pulses or 3 pulses, a fitting assuming double pulses is done on the target PMT signal. And the variables extracted from the fitting are used to identify the decay modes.

#### 5.3.1 Pulse fitting

Fig.5.7 shows the typical waveform of the target scintillator. In the waveform there is 2 kind of points, the circle points are the data from the first ADC and the triangle points are the data from the second ADC in the channel [§3.4.1]. The top figure is from  $\pi^+ \rightarrow e^+$  sample and the bottom figure is from  $\pi^+ \rightarrow \mu^+ \rightarrow e^+$ . In order to fit these waveforms, templates are prepared from the data. The top figure in Fig.5.8 shows the 2-dimensional histogram in which the waveform data are filled after normalization with the integrated charge and the time offset correction with TDC information. The bottom figure shows the template which is obtained by taking the mean of each timing bin of the 2-dimensional histograms.

The waveforms are fitted assuming double pulses. The function below is used as a fitting function.

$$V(t) = A_1 F(t + T_1) + A_2 F(t + T_2) \quad (5.18)$$

$F(t)$  is the waveform template of single pulse and  $A_1, A_2, T_1, T_2$  are parameters of the fit.  $A_1$  and  $T_1$  are the amplitude and the timing of the first pulse, respectively.  $A_2$  and  $T_2$  are the parameters of the second pulse. The fitting region is from -20 ns to 60 ns with respect to the peak timing which is 40 FADC samples.  $\sigma$  of each sample is set to 2.3 mV to all PMTs. The lines in Fig.5.7 show the results of the fit. Fig.5.9 shows the useful variables for the decay mode identification which is obtained from fitting. For

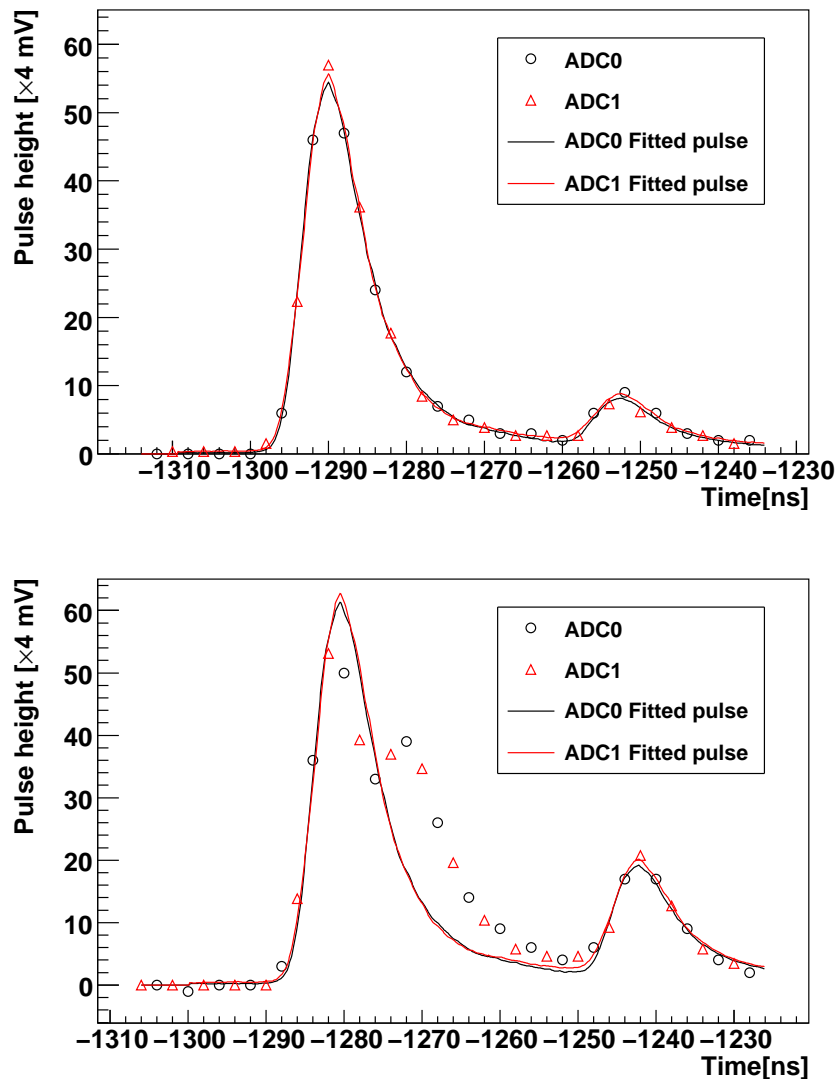


Figure 5.7: Waveform data of the target PMT.

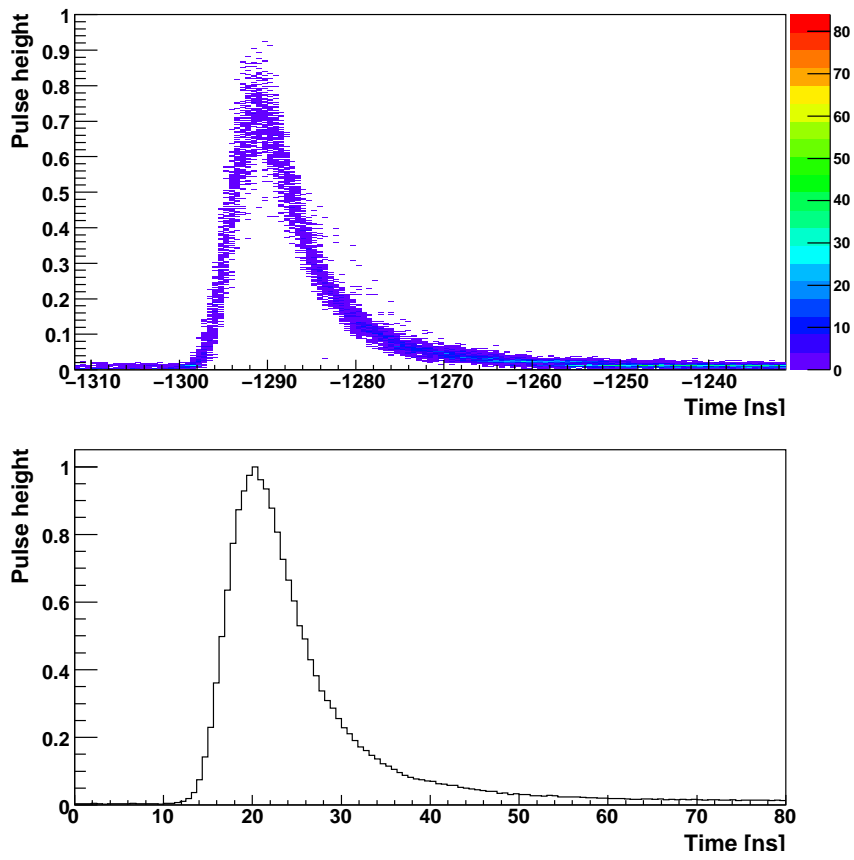


Figure 5.8: Waveform template for the pulsefitting.

these plots the  $\pi^+ \rightarrow \mu^+ \rightarrow e^+$  sample is not after Total-Energy-Cut to keep  $\pi^+ \rightarrow \mu^+ \rightarrow e^+$  pion-decay-at-rest events ( $\pi$ DAR), because identification capability of  $\pi$ DAR events needs to be studied. The top left histogram shows the  $\chi^2$  of the fit. The blue line shows  $\pi^+ \rightarrow e^+\nu$  sample and red line shows  $\pi^+ \rightarrow \mu^+ \rightarrow e^+$  sample. The peak value of the  $\chi^2$  is about 65 although it should be around 36 which is the number of degree of freedom of the fit and the shape is also different from ideal  $\chi^2$  distribution. This means the  $\sigma$  of each sample point may not be correct or the waveform shape have some non-linear effects. However there is clearly a big difference of the  $\chi^2$  between the two decay modes. The top right histogram shows the  $\chi^2$  of  $\pi^+ \rightarrow \mu^+ \rightarrow e^+$  sample and it distribute around 10000 which is 100 times bigger than that of  $\pi^+ \rightarrow e^+\nu$  decay. The bottom left figure shows the absolute value of the timing difference between the fitted first pulse of the target and B1 hit. In case of  $\pi^+ \rightarrow e^+\nu$  decay, it should distribute around 0, however in case of  $\pi^+ \rightarrow \mu^+ \rightarrow e^+$  decay, the timing may be delayed due to overlapped muon pulse. The same things happens for positron timing. The bottom right figure shows the absolute value of the timing difference between the fitted second pulse of the target and T1 hit. In  $\pi^+ \rightarrow \mu^+ \rightarrow e^+$  case, the timing may be earlier due to overlapped muon pulse. The peak at around 12 if due to the parameter limit of the fitting. These 3 variables are useful for decay mode identification. The likelihood of  $\pi^+ \rightarrow e^+\nu$  events will be defined with these information. The pulse height information is not used because energy deposit information is already use as Total-Energy-Cut.

### 5.3.2 Likelihood definition for pulse shape cut

Fig.5.10 shows the probability functions which are defined from the each variable distribution of the  $\pi^+ \rightarrow e^+$  sample. The likelihood for  $\pi^+ \rightarrow e^+\nu$  decay is defined with these probability functions as below.

$$L_{PMT\_i} = p_{\chi^2} \times p_{B1\Delta t} \times p_{T1\Delta t}$$

$$L_{all} = \log(L_{PMT\_a} \times L_{PMT\_b} \times L_{PMT\_c})$$

The likelihood of each PMT is defined first and then the integrated likelihood (PS-Likelihood) is defined as a multiplication of 3 PMT's likelihood except one PMT which has the worst likelihood. This is because sometimes fitting fails and the resulting likelihood value is small even if it is  $\pi^+ \rightarrow e^+$  events.

### 5.3.3 Suppression capability to the pion decay at rest event

The top left histogram in Fig.5.11 shows PS-Likelihood of the two decay modes and the bottom left shows the efficiency as a function of the cut value. All the events whose likelihood is less than -29 is filled as -29. The dashed purple line shows the cut which keeps 90% of  $\pi^+ \rightarrow e^+\nu$  and reject 86% of  $\pi^+ \rightarrow \mu^+ \rightarrow e^+$  DAR events. The top right histograms shows Total-Energy before and after the PS-Likelihood cut (PS-Cut). The bottom right figure shows the ratio of these two histograms which corresponds to the suppression factor of each Total-Energy bin. This shows that the suppression factor between 17 MeV and 20 MeV has no correlation with Total-Energy. The reason why the suppression factor bellow 17 MeV is bad is that the events below 17 MeV are mostly  $\pi$ DIF events.

### 5.3.4 Pulse shape cut after Total-Energy-Cut

$\pi^+ \rightarrow \mu^+ \rightarrow e^+$  decay sample without Total-Energy-Cut was used to estimate PS-likelihood capability to suppress  $\pi$ DAR events. However, from now on we use the original data samples which is after Total-

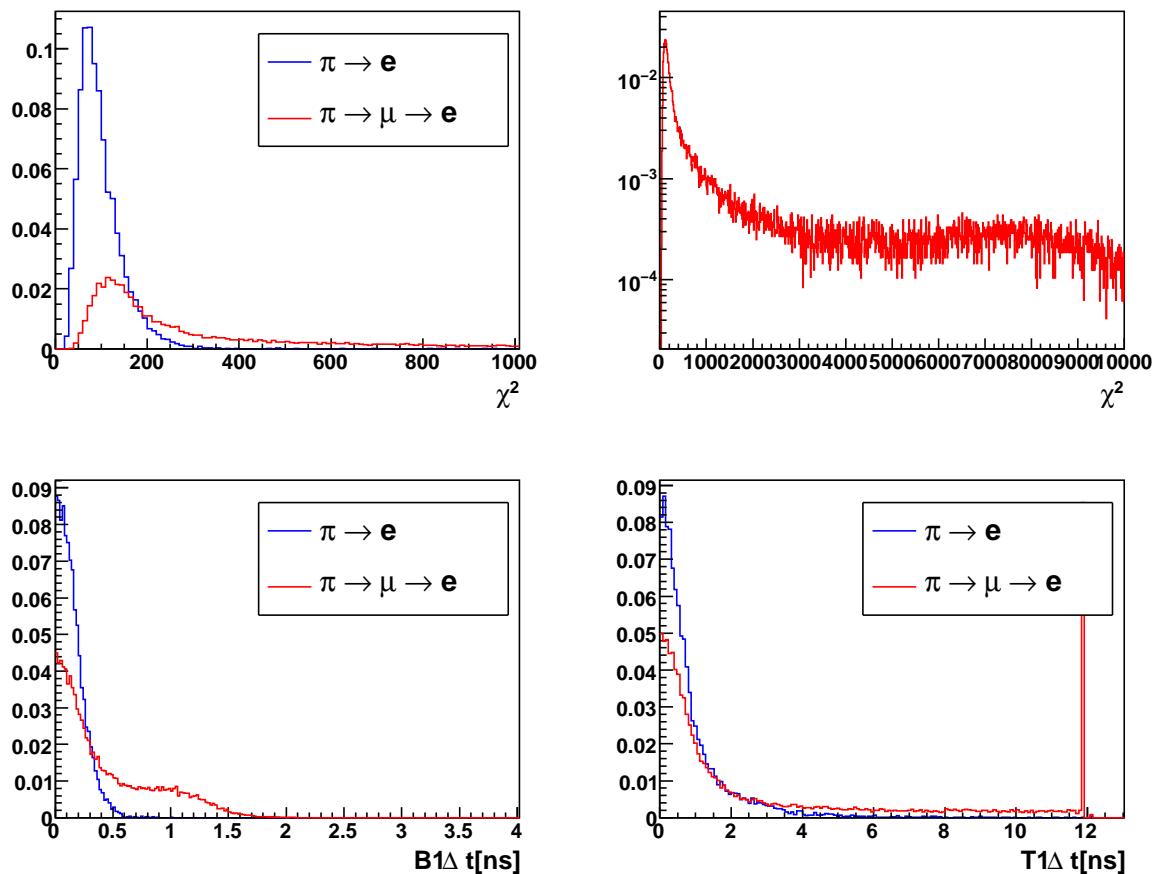


Figure 5.9: Variables extracted by pulse fitting. Top:  $\chi^2$  distribution. Bottom Left: Absolute time difference between the fitted first pulse of the target and B1 hit. Bottom Right: Absolute time difference between the fitted second pulse of the target and T1 hit. Blue line shows  $\pi^+ \rightarrow e^+$  decay and Red line shows  $\pi^+ \rightarrow \mu^+ \rightarrow e^+$  in which pion decays at rest (DAR).

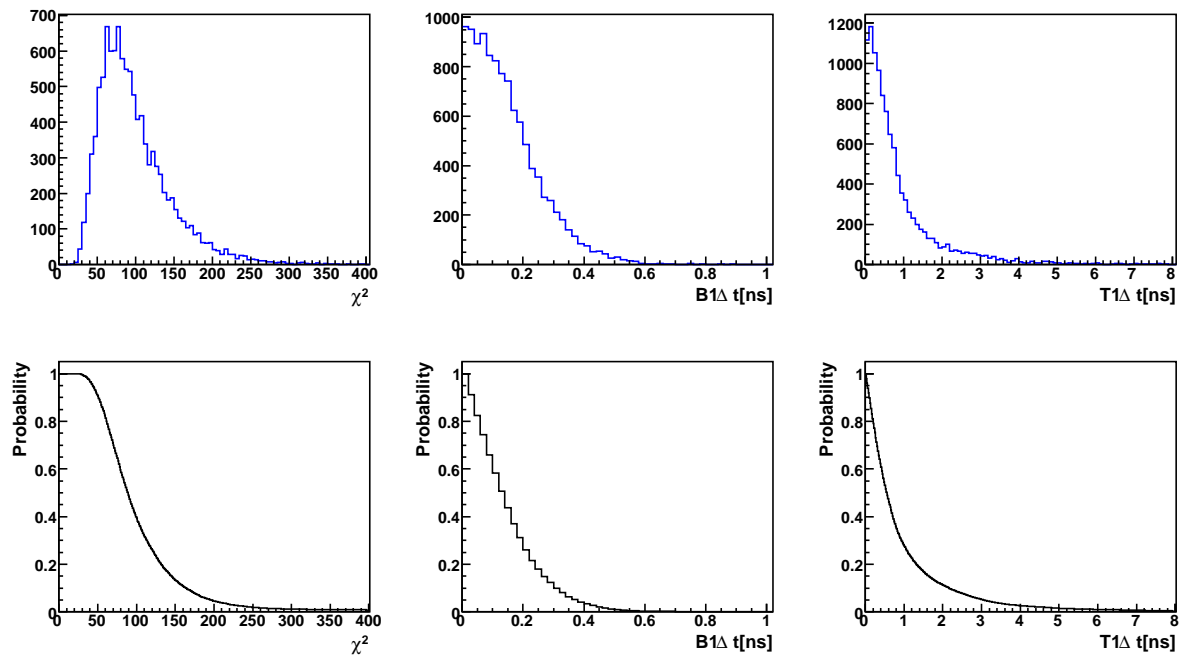


Figure 5.10: Probability density functions of the variables which are extracted from pulse fitting.

Energy-Cut to define the cut to suppress  $\pi^+ \rightarrow \mu^+ \rightarrow e^+$  decay after Total-Energy-Cut.

Fig.5.12 shows PS-Likelihood after Total-Energy-Cut. The blue line shows  $\pi^+ \rightarrow e^+\nu$  decay sample and red line shows  $\pi^+ \rightarrow \mu^+ \rightarrow e^+$  decay sample. The reason why the distribution of  $\pi^+ \rightarrow \mu^+ \rightarrow e^+$  decay sample is different from the events shown in Fig.5.11 is that  $\pi^+ \rightarrow \mu^+ \rightarrow e^+$  decay sample after Total-Energy-Cut mainly consists of  $\pi$ DIF events. The dashed purple line shows the cut which keep 90% of  $\pi^+ \rightarrow e^+\nu$  events.

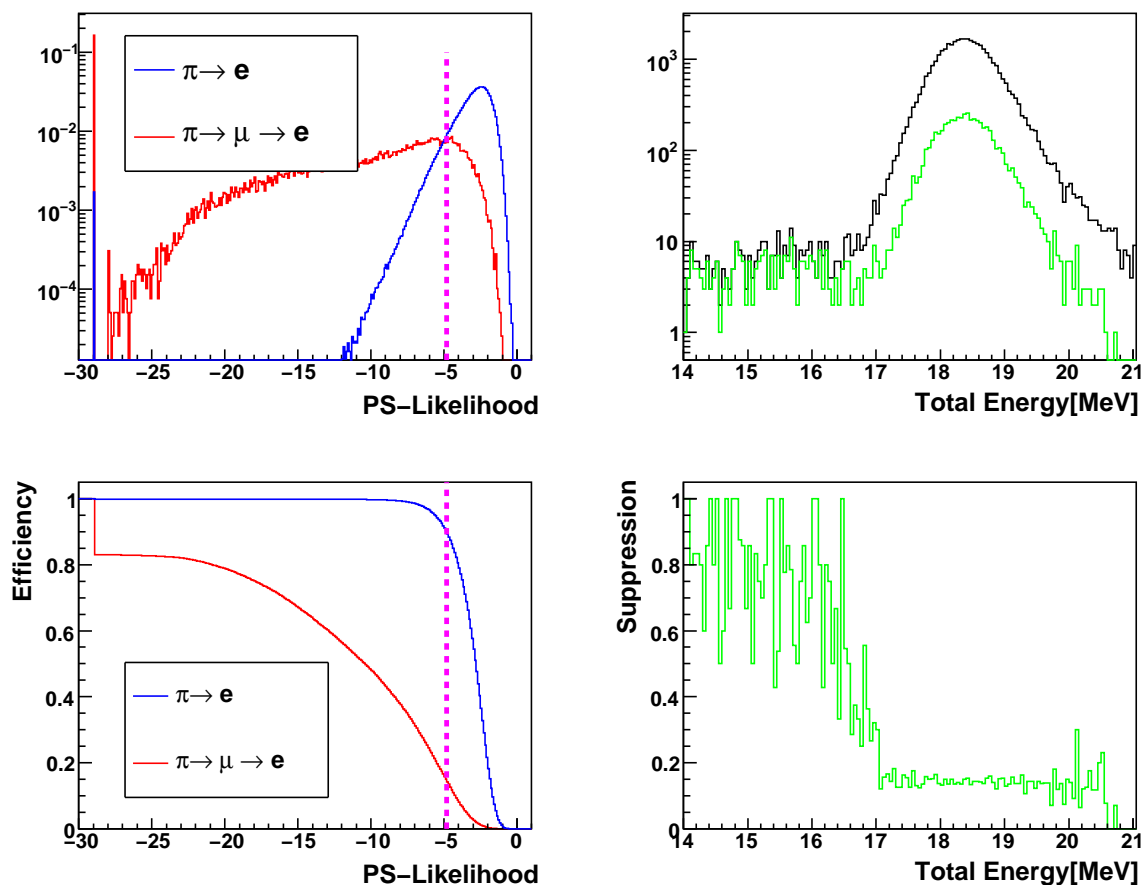


Figure 5.11: Capability of PS-Cut to suppress  $\pi^+ \rightarrow \mu^+ \rightarrow e^+$  DAR events. Top left: PS-Likelihood of two decay modes. Bottom left: Efficiency as a function of the cut value. Top right shows Total-Energy. Green line is after applying PS-Cut which is shown with dashed purple line. Bottom right is the ratio of the two histograms of the top right figure.

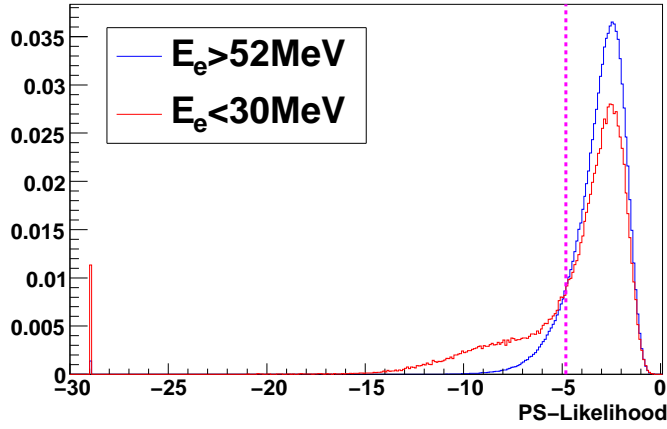


Figure 5.12: Pulse-Shape-Likelihood distribution. Blue line is  $\pi^+ \rightarrow e^+$  sample and Red line is  $\pi^+ \rightarrow \mu^+ \rightarrow e^+$  sample

## 5.4 Cut optimization

In the previous section, the variables which are useful to suppress  $\pi^+ \rightarrow \mu^+ \rightarrow e^+$  events were described. In this section the cuts using these variables will be optimized. These variables seems to be totally independent from each other for  $\pi^+ \rightarrow e^+\nu$  events. But for  $\pi^+ \rightarrow \mu^+ \rightarrow e^+$  events, the variables might have strong correlation. In order to optimize the cuts to minimize 'S', the procedure below is used.

- Define temporal cut which keep 90% of  $\pi^+ \rightarrow e^+\nu$  sample for all the variables (Temporal-Suppression-Cut)
- Make Total-Energy distribution of 2 decay mode samples with Temporal-Suppression-Cut and define the Total-Energy-Cut to minimize 'S'.
- Make Incident-Angle distribution with the Temporal-Suppression-Cut and Total-Energy-Cut defined above and define the Incident-Angle-Cut to minimize 'S'.
- Make Rmin distribution with Temporal-Suppression-Cut and the cuts defined before and define the Rmin-Cut to minimize 'S'.
- Make Zmin distribution with Temporal-Suppression-Cut and the cuts defined before and define the Zmin-Cut to minimize 'S'.
- Make PS-Likelihood distribution with the cuts defined before and define the PS-Cut to minimize 'S'.

The cut sequence is from the strong cut to the weak cut. The detail of the processes is described in this section.

### 5.4.1 Total energy cut

The top left histograms in Fig.5.13 shows Total-Energy of the two decay modes with Temporal-Suppression-Cut. The bottom left figure shows 'S' as a function of the lower and higher cut value of Total-Energy-Cut and the bottom right figure shows the efficiency of  $\pi^+ \rightarrow e^+\nu$  sample. The values which minimize 'S' is adopted as the cut values. The white box in the figure and the dashed purple line in Total-Energy spectrum shows the cuts. The  $\pi^+ \rightarrow e^+\nu$  efficiency is 82% for this cuts.

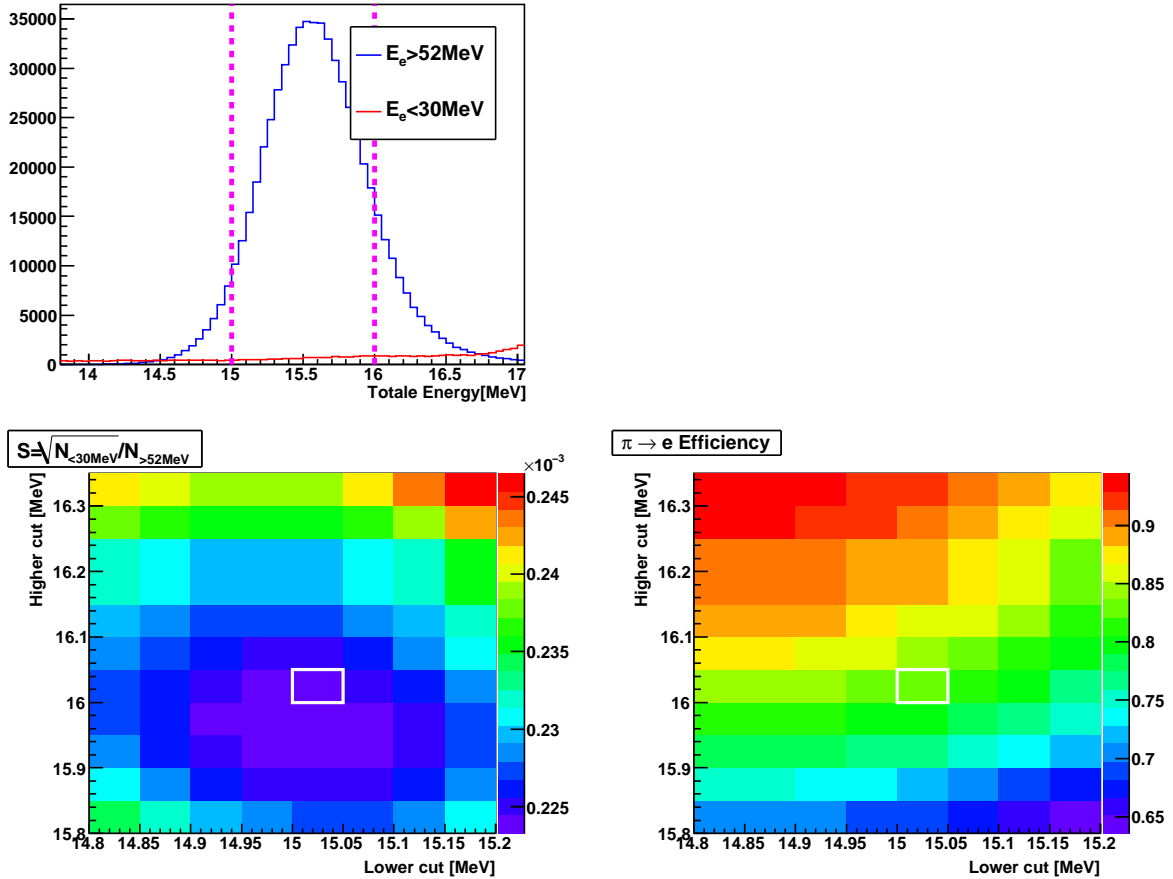


Figure 5.13: Optimization of Total-Energy-Cut. Top left: Total-Energy after Temporal-Suppression-Cut. Blue line is  $\pi^+ \rightarrow e^+$  sample and Red line is  $\pi^+ \rightarrow \mu^+ \rightarrow e^+$  sample. Bottom left: 'S' value as a function of cut value. Bottom right:  $\pi^+ \rightarrow e^+$  efficiency as a function of cut value. The dashed purple line and the white box show the adopted cut.

## 5.4.2 Tracking cut

### Incident angle cut

The top left histograms in Fig.5.14 shows the Incident-Angle of the two decay modes with Temporal-Suppression-Cut and Total-Energy-Cut which were optimized. The bottom left figure shows 'S' as a function of the cut value of Incident-Angle-Cut and the bottom right figure shows efficiency of  $\pi^+ \rightarrow e^+\nu$  sample. The value which minimize 'S' is adopted as the cut values. The dashed purple line shows the optimized cut. The  $\pi^+ \rightarrow e^+\nu$  efficiency is 97% with this cuts.

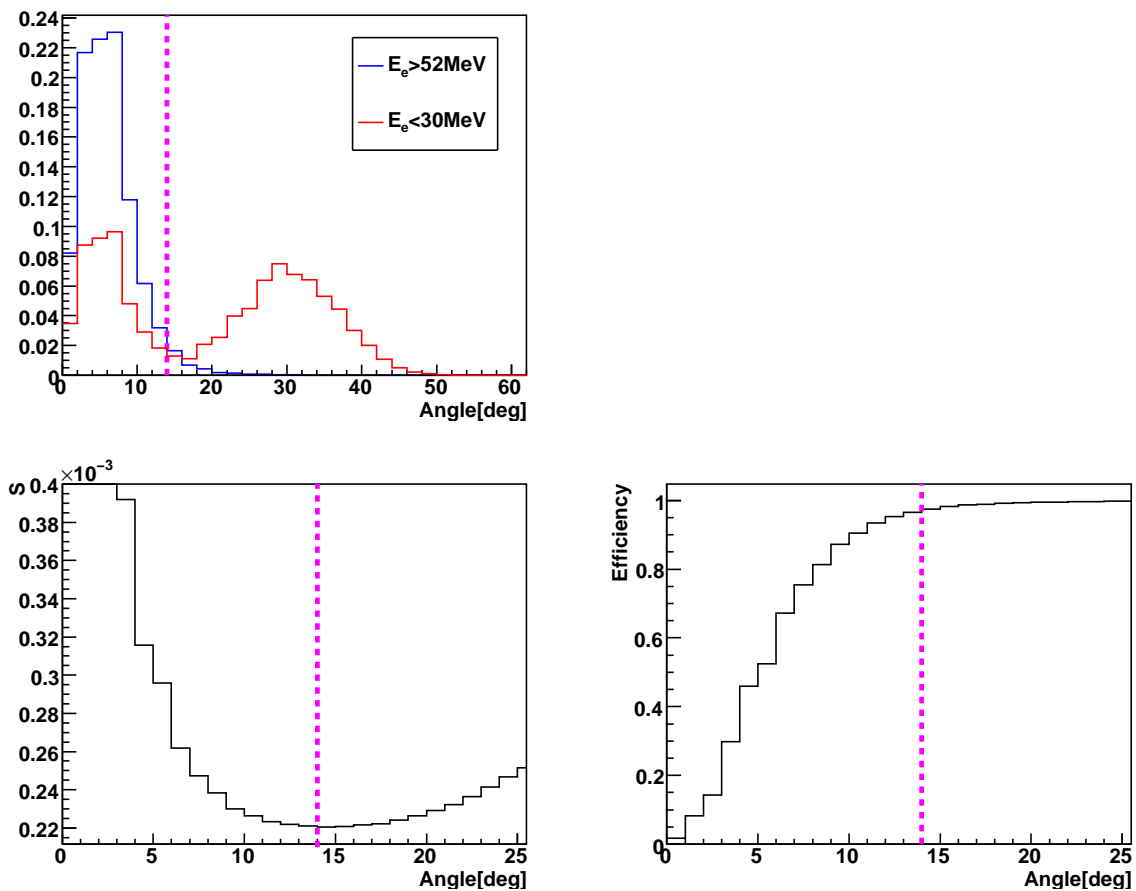


Figure 5.14: Optimization of Incident-Angle-Cut. Top left: Incident-Angle after Temporal-Suppression-Cut and Total-Energy-Cut optimized previously. Blue line is  $\pi^+ \rightarrow e^+$  sample and Red line is  $\pi^+ \rightarrow \mu^+ \rightarrow e^+$  sample. Bottom left: 'S' value as a function of cut value. Bottom right:  $\pi^+ \rightarrow e^+$  efficiency as a function of the cut value. Dashed purple line shows the adopted cut.

### 5.4.3 Rmin cut

The top left histograms in Fig.5.15 shows the Rmin distribution of the two decay modes with Temporal-Suppression-Cut and the cuts which were optimized previously. The bottom left figure shows 'S' as a function of cut value of Rmin-Cut and the bottom right figure shows efficiency of  $\pi^+ \rightarrow e^+\nu$  sample. The values which minimize 'S' is adopted as a cut value. The dashed purple line shows the optimized cut. The  $\pi^+ \rightarrow e^+\nu$  efficiency is 86% for this cuts.

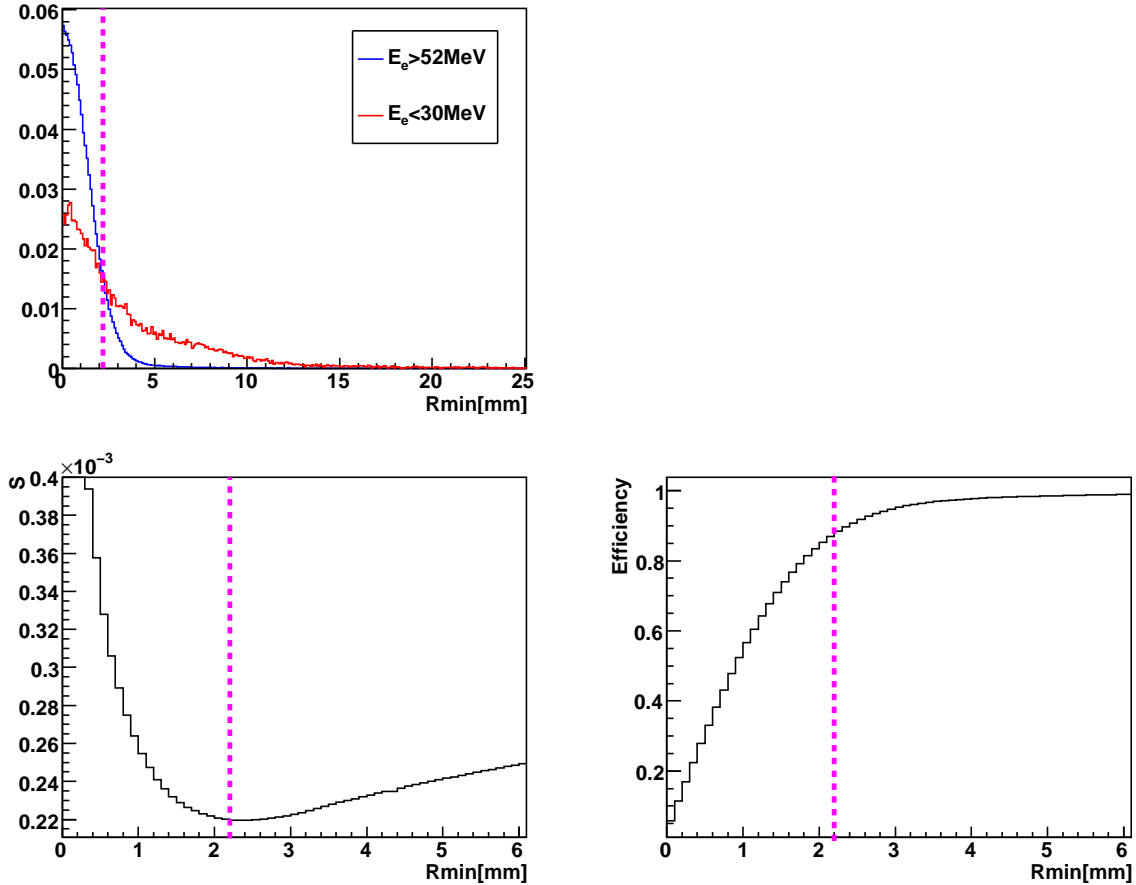


Figure 5.15: Optimization of Rmin-Cut. Top left: Rmin after Temporal-Suppression-Cut and the cuts which were optimized before. Blue line is  $\pi^+ \rightarrow e^+$  sample and Red line is  $\pi^+ \rightarrow \mu^+ \rightarrow e^+$  sample. Bottom left: 'S' value as a function of cut value. Bottom right:  $\pi^+ \rightarrow e^+$  efficiency as a function of the cut value. Dashed purple line shows the adopted cut.

### 5.4.4 Zmin cut

The top left histograms in Fig.5.16 shows the Zmin of two decay modes with Temporal-Suppression-Cut and the cuts optimized previously. The bottom left figure shows 'S' as a function of the lower and higher cut value of Zmin-Cut and the bottom right figure shows efficiency of  $\pi^+ \rightarrow e^+ \nu$  sample. The values which minimize 'S' is adopted as the cut values. The dashed purple line shows the optimized cut. The  $\pi^+ \rightarrow e^+ \nu$  efficiency is 87% for this cuts.

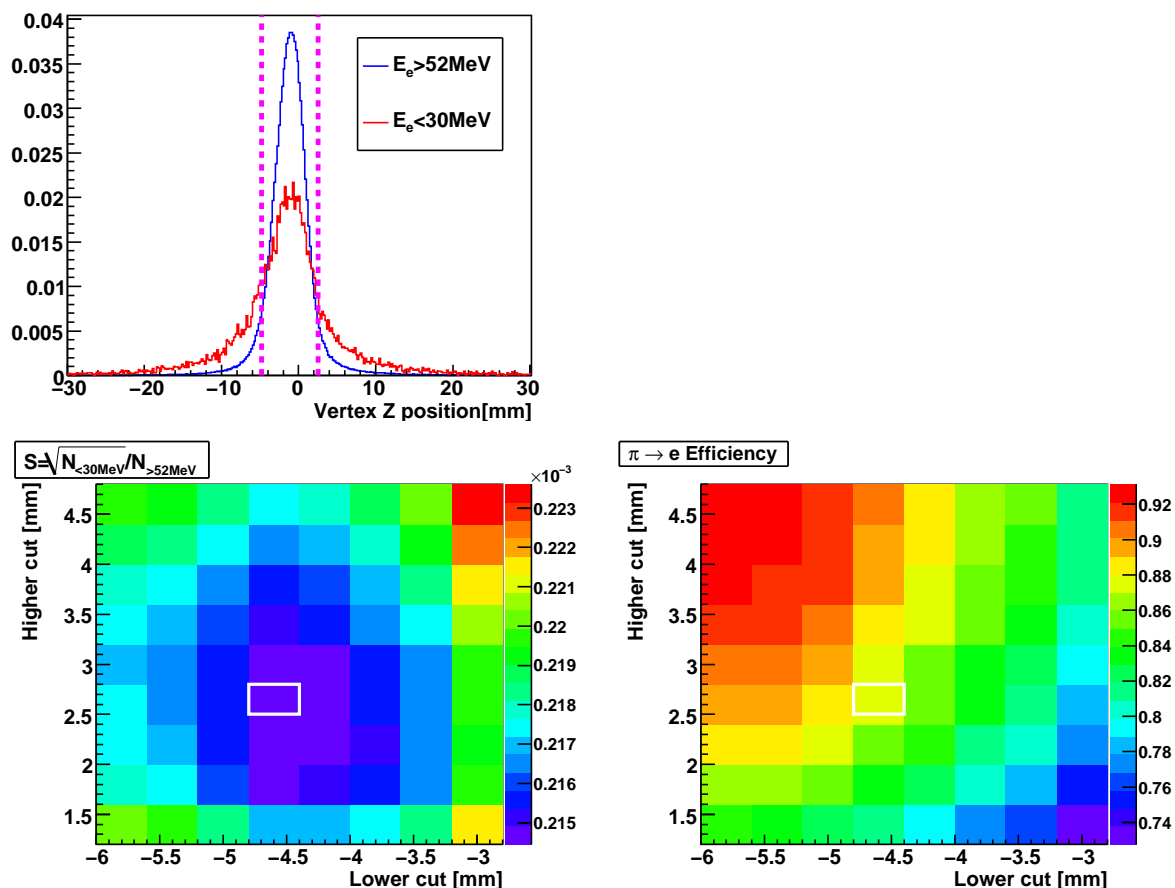


Figure 5.16: Optimization of Zmin-Cut. Top left: Zmin after Temporal-Suppression-Cut and the cuts optimized previously. Blue line is  $\pi^+ \rightarrow e^+$  sample and Red line is  $\pi^+ \rightarrow \mu^+ \rightarrow e^+$  sample. Bottom left: 'S' value as a function of cut values. Bottom right:  $\pi^+ \rightarrow e^+$  efficiency as a function of the cut values. Dashed purple line and the white box line shows the adopted cut.

### 5.4.5 Pulse shape cut

The top left histograms in Fig.5.17 shows the PS-Likelihood of the two decay modes with the cuts optimized previously. The bottom left figure shows 'S' as a function of the cut value of PS-Cut and the bottom right figure shows efficiency of  $\pi^+ \rightarrow e^+\nu$  sample. The values which minimize 'S' is adopted as the cut value. The dashed purple line shows the optimized cut. The  $\pi^+ \rightarrow e^+$  efficiency is 99.5% for this cuts.

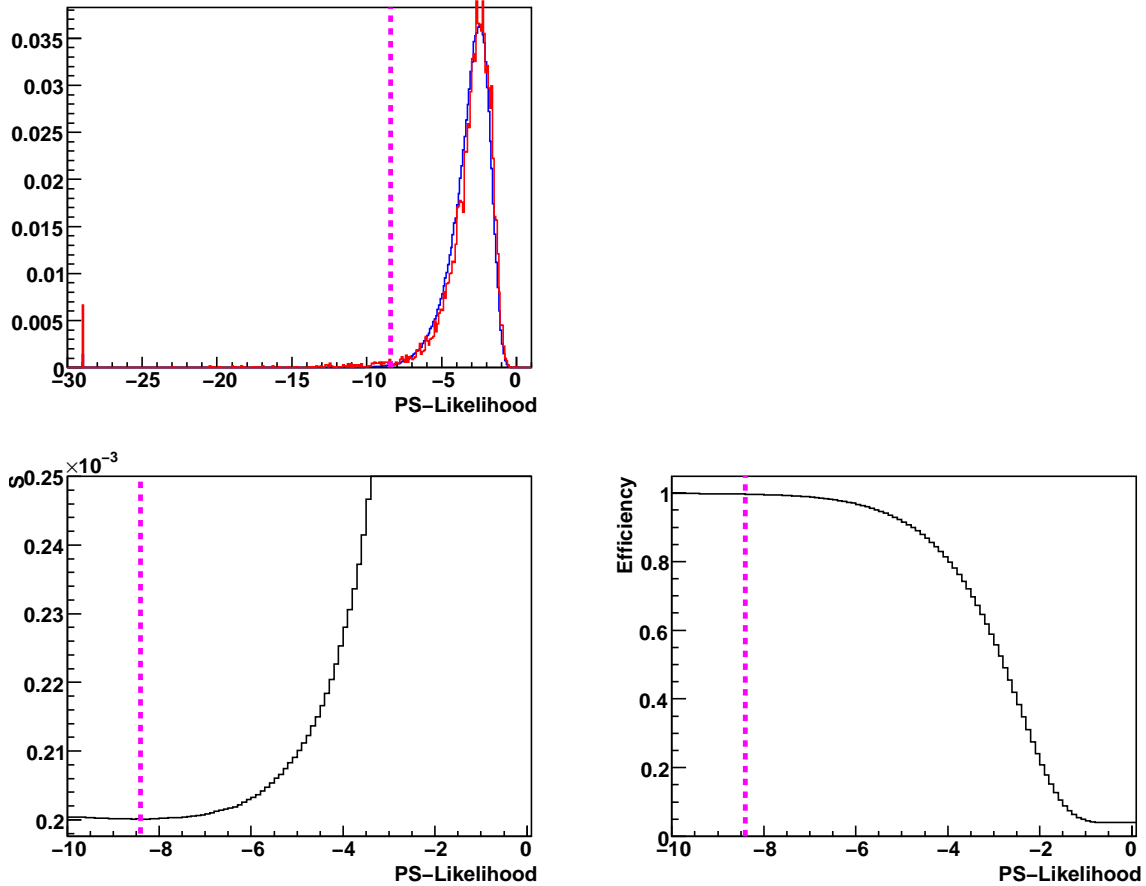


Figure 5.17: Optimization of PS-Cut. Top left: PS-Likelihood after the suppression cuts optimized previously. Blue line is  $\pi^+ \rightarrow e^+$  sample and Red line is  $\pi^+ \rightarrow \mu^+ \rightarrow e^+$  sample. Bottom left: 'S' value as a function of cut value. Bottom right:  $\pi^+ \rightarrow e^+$  efficiency as a function of the cut values. Dashed purple line shows the adopted cut.

### 5.4.6 Summary of cut optimization

The left histogram in Fig.5.18 shows the positron energy spectrum for each cuts. The table below shows the result of the suppression cuts.

Cut	$\pi e$ efficiency (in total)	$N_{<52MeV}/N_{>52MeV}$	S
			$\sqrt{N_{<52MeV}/N_{>52MeV}}$
Total-Energy	80%(80%)	40.3%	$7.7 \times 10^{-4}$
+Incident-Angle	96%(77%)	20.3%	$5.6 \times 10^{-4}$
+Rmin	84%(65%)	9.8%	$4.2 \times 10^{-4}$
+Zmin	86%(56%)	6.9%	$3.8 \times 10^{-4}$
+PS	100%(56%)	6.8%	$3.8 \times 10^{-4}$

Table 5.2: Summary of Suppression-Cut.

$S = 3.8 \times 10^{-4}$  is obtained after all suppression cuts. PS-Cut has almost no effect on the suppression, this mean there are almost no DAR events after suppression cuts. Thus the events left after suppression are the DIF events or low energy tail of  $\pi \rightarrow e$  decay.

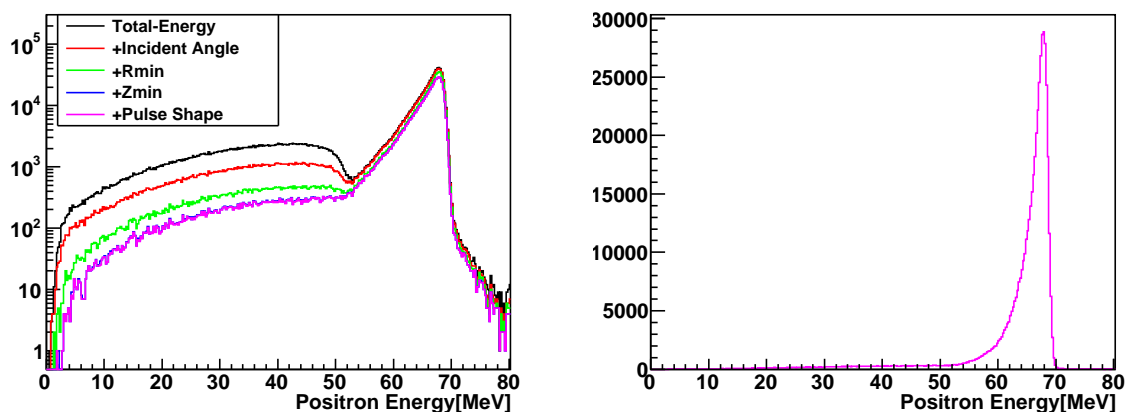


Figure 5.18: Positron energy spectrum with the suppression cuts. Left figure shows the effect of each cut. Right figure shows the spectrum after all the cuts.

### 5.4.7 Fiducial cut on WC3

The left events after suppression cut include some low energy tail of  $\pi^+ \rightarrow e^+\nu_e$  events. It is known from Monte Carlo study that the fiducial cut at WC3 has correlation with the tail. For the suppression cuts study 'Radius at WC3 < 80 mm' is used as a fiducial cut on WC3. Fig.5.19 shows the relation of the fiducial cut on WC3 and the tail. The top left figure shows the positron radius distribution at WC3 after all suppression cuts. The other 3 plots show efficiency of  $\pi^+ \rightarrow e^+\nu$  events,  $N_{<52MeV}/N_{>52MeV}$ , and  $S=\sqrt{N_{<52MeV}/N_{>52MeV}}$  as a function of the WC3 fiducial cut, respectively.  $N_{<52MeV}/N_{>52MeV}$  decrease with the radius cut value, this mean the low energy tail of  $\pi^+ \rightarrow e^+\nu$  events decreases with the fiducial cut. However the ratio have almost no change if the cut become less than 50 mm. This means almost all the tail which has a correlation with the fiducial cut are eliminated and most of the events left are  $\pi^+ \rightarrow \mu^+ \rightarrow e^+$  DIF event. The dashed purple line in the figure shows the adopted cut value (Radius at WC3 < 80mm) to minimize 'S'.

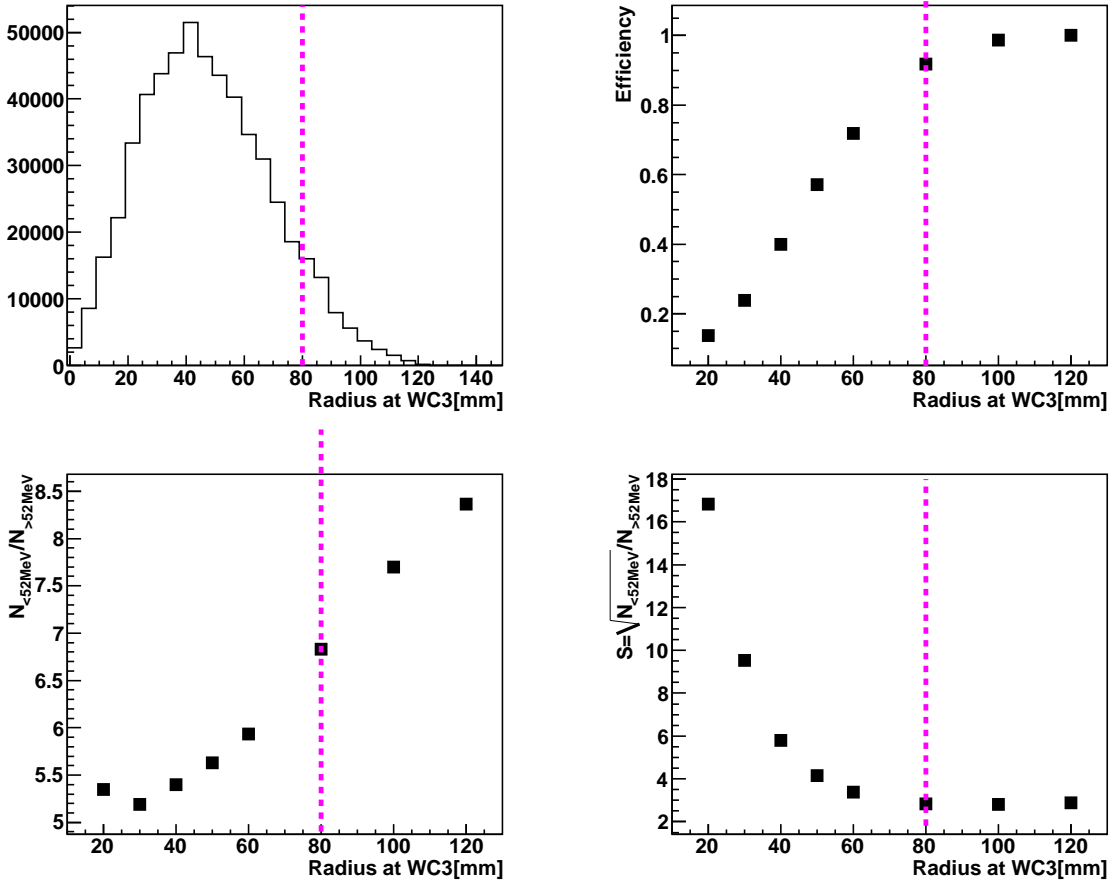


Figure 5.19: Fiducial cut on WC3. Top left shows the radius at WC3 after all suppression cuts. top right: efficiency of  $\pi^+ \rightarrow e^+$  event, bottom left:  $N_{<52MeV}/N_{>52MeV}$ , bottom right:  $S=\sqrt{N_{<52MeV}/N_{>52MeV}}$ . Dashed purple line shows the adopted cut.

## 5.5 Summary of $\pi^+ \rightarrow e^+\nu$ decay selection

The positron energy spectrum of  $\pi^+ \rightarrow e^+\nu$  events with good background suppression (Suppressed-Spectrum) are obtained. In order to suppress  $\pi^+ \rightarrow \mu^+ \rightarrow e^+$  decay event, Total-Energy-Cut, Incident-Angle-Cut, Rmin-Cut, Zmin-Cut and PS-Cut were defined. Also, to reduce the low energy tail from  $\pi^+ \rightarrow e^+\nu$  decay itself the fiducial cut on WC3 was optimized. Fig.5.20 shows the spectrum after the cuts optimization to minimize  $S=\sqrt{N_{<52MeV}}/N_{>52MeV}$ . The information of the spectrum is shown in Table5.3.

$N_{>52MeV}$	$N_{<52MeV}$	$N_{<52MeV}/N_{>52MeV}$	$S=\sqrt{N_{<52MeV}}/N_{>52MeV}$
477554	32623	6.8%	$3.8 \times 10^{-4}$

Table 5.3: Summary of positron energy spectrum after background suppression.

This spectrum will be used for massive neutrino search in the next chapter.

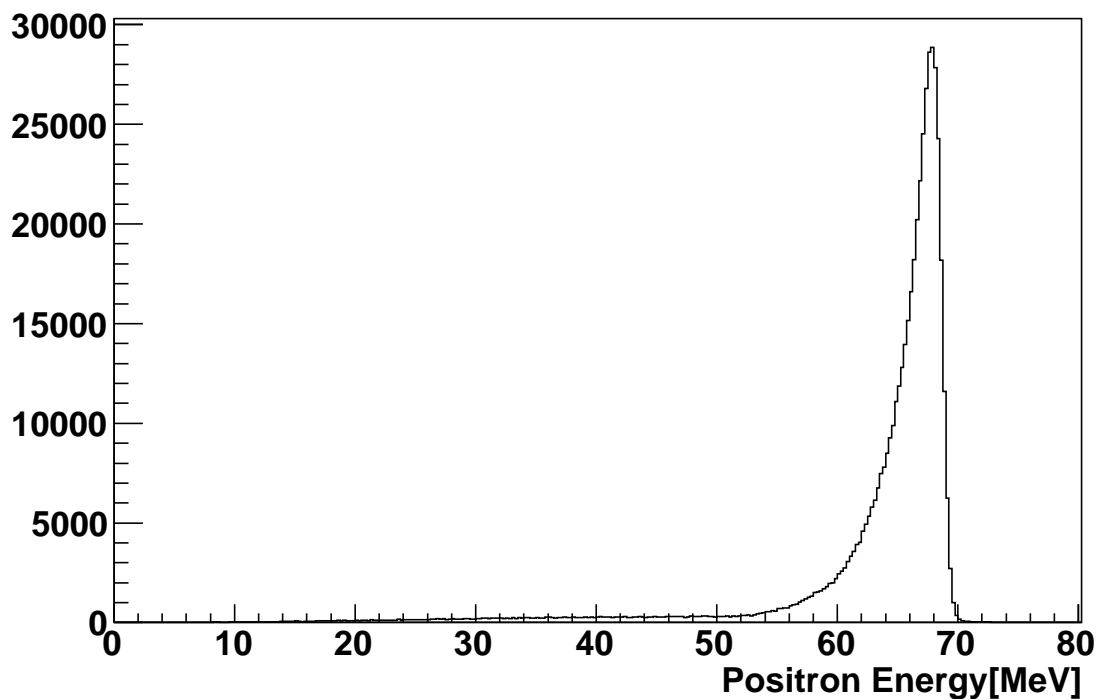


Figure 5.20: Positron energy spectrum after background suppression for massive neutrino search.



## Chapter 6

# Spectrum fitting for massive neutrino search

The positron energy spectrum of  $\pi^+ \rightarrow e^+\nu$  decay with suppression of  $\pi^+ \rightarrow \mu^+ \rightarrow e^+$  events (Suppressed-Spectrum) was obtained in the last chapter. Massive neutrino search will be done by fitting this spectrum in this chapter.

### 6.1 Component of the spectrum

First of all, the components of the spectrum and the spectrum shape of them should be known for spectrum fitting. Suppressed-Spectrum includes 4 component below.

- $\pi^+ \rightarrow \mu^+ \rightarrow e^+$  muon decay-at-rest ( $\mu$ DAR)
- $\pi^+ \rightarrow \mu^+ \rightarrow e^+$  muon decay-in-flight ( $\mu$ DIF)
- Low energy tail of  $\pi^+ \rightarrow e^+\nu_e$  decay
- Positron from  $\pi^+ \rightarrow e^+\nu_i$  decay (if massive neutrinos exist)

Positron energy spectrum shape of these component is estimated in this section.

#### 6.1.1 Positron energy spectrum shape of $\pi^+ \rightarrow \mu^+ \rightarrow e^+$ muon decay-at-rest ( $\mu$ DAR)

Positron energy spectrum of  $\pi^+ \rightarrow \mu^+ \rightarrow e^+$  muon decay-at-rest( $\mu$ DAR) which are left after suppression cut is obtained by using delayed event which occurred 200 ns after pion stop.  $\pi^+ \rightarrow e^+\nu$  events and  $\mu$ DIF events are suppressed by factor  $10^3$  because of pion lifetime. The blue line in Fig.6.1 shows the spectrum. The number of events of the histogram is 3 times lower than the events which are left in Suppressed-Spectrum because the delayed events are prescaled by factor of 16 [§3.3]. This means it has  $\sqrt{3}$  time more statistical error than the statistical error of Suppressed-Spectrum itself. In order to know more accurate shape, the energy spectrum of delayed event without Total-Energy-Cut is made as shown in Fig.6.1 with the red line. The shape has no obvious difference although some systematic difference could have appeared due to the cut condition difference.

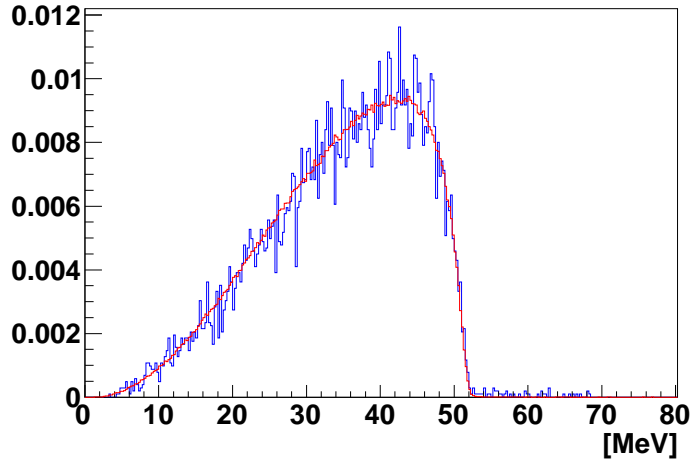


Figure 6.1: Positron energy spectrum of  $\pi^+ \rightarrow \mu^+ \rightarrow e^+$  muon decays-at-rest event. Blue line is with Total-Energy-Cut. Red line is without Total-Energy-Cut

### 6.1.2 Positron energy spectrum shape of $\pi^+ \rightarrow \mu^+ \rightarrow e^+$ muon decays-in-flight

If muons from pion-decay decay to positron in flight ( $\mu$ DIF), the energy distribution of the positron become different from the spectrum of  $\mu$ DAR events. From the Monte Carlo study,  $\mu$ DIF become about 2% compared to  $\pi^+ \rightarrow e^+ \nu_e$  decay after suppression cut.[§2.5] However, it is impossible to know the positron energy spectrum shape of  $\mu$ DIF events from the data because it is impossible to eliminate  $\pi^+ \rightarrow \mu^+ \rightarrow e^+$   $\mu$ DAR and low energy tail of  $\pi^+ \rightarrow e^+ \nu_e$  decay from the spectrum by changing the time window. Instead of seeing it, a Monte Carlo simulation is done to know the rough shape of the spectrum. Fig.6.2 shows energy spectrum of positron from  $\pi^+ \rightarrow \mu^+ \rightarrow e^+$   $\mu$ DIF with the Monte Carlo. Red line shows the spectrum of muons which have more than 3.3 MeV when decaying. These muons are expected to be left after Total-Energy-Cut. The spectrum shape is continuous and there is no bump while the spectrum has longer tail in high energy region.

### 6.1.3 Positron energy spectrum shape of low energy tail of $\pi^+ \rightarrow e^+ \nu_e$ decay

It is impossible to know the positron energy spectrum shape of low energy tail of  $\pi^+ \rightarrow e^+ \nu_e$  decay because there is no way to eliminate  $\pi^+ \rightarrow \mu^+ \rightarrow e^+$  decay from the spectrum. Instead of seeing it, beam positron data is used to know rough shape of low energy tail of  $\pi^+ \rightarrow e^+ \nu_e$  decay. Fig.6.3 shows the energy spectrum of 75 MeV/c beam positrons. Energy deposit in upstream counter (B1, B2, S1, S2, Target) is not included in the energy spectrum. There are 3 bump around 62MeV, 53 MeV and 42 MeV. It is known that these bumps are due to photo-nuclear interaction from Monte Carlo study. Some times photons from electromagnetic shower interact with nucleus and kick out neutrons. If the neutrons don't emit the energy again within the FADC gate or just escape from the detector, it makes missing energy.

Difference between actual positrons from  $\pi^+ \rightarrow e^+ \nu_e$  decay and beam positron is an angle to the detector and radiative decay effect. That is why amount of actual tail from  $\pi^+ \rightarrow e^+ \nu_e$  decay could be larger than that of beam positron, however it should not have any additional bump except 3 bump due to photo-nuclear interaction.

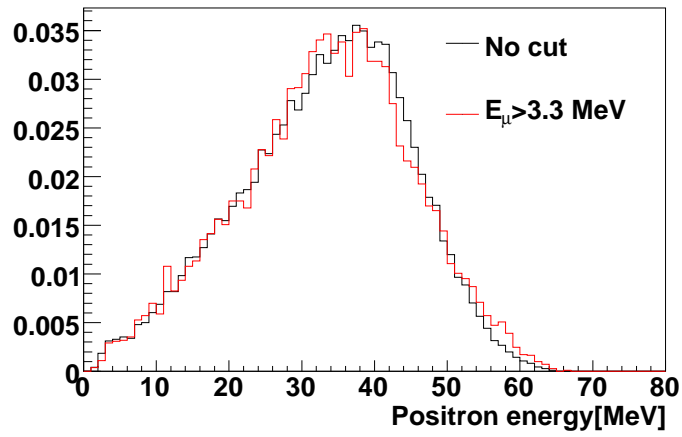


Figure 6.2: Positron energy spectrum of  $\pi^+ \rightarrow \mu^+ \rightarrow e^+$  muon decays-in-flight event. Red line shows the events in which muons have more than 3.3 MeV of kinematic energy when decaying.

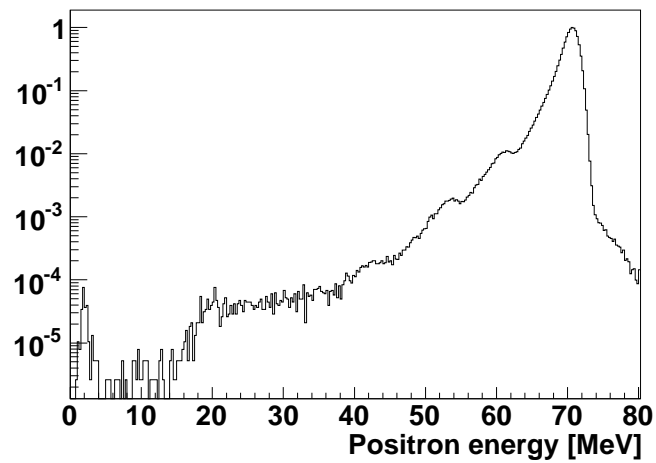


Figure 6.3: Energy spectrum of 75 MeV/c beam positron.

### 6.1.4 Positron energy spectrum shape of $\pi^+ \rightarrow e^+\nu_i$ decay

#### Overview

In order to search an additional bump due to a massive neutrino in the positron energy spectrum, the shape of the bump should be known. Basically the shape should be the same as the spectrum of  $\pi^+ \rightarrow e^+\nu_e$  decay although the shape could change depending on the positron energy. In this subsection, the shape of the energy spectrum of different positron energy is estimated with a Monte Carlo simulation.

In this subsection the Monte Carlo is tuned to have a broader shape than the real data, because if the shape from Monte Carlo is broader than actual data the upper limit become conservative. Procedure to tune the Monte Carlo is described below.

- Estimation of the energy resolution of the NaI calorimeter from the data and implementation in the Monte Carlo
- Comparison and optimization of the Monte Carlo with the 70 MeV positron peak of  $\pi^+ \rightarrow e^+\nu_e$  decay data
- Estimation of the positron energy dependence effect with beam positron data and the Monte Carlo
- Generation of the energy spectrum of decay positron at several energies with the Monte Carlo. (Signal MC)

The Monte Carlo will be tuned at 70 MeV by using positron from  $\pi \rightarrow e\nu_e$  decay and the energy dependence effect will be evaluated with beam positron data. After that, the energy spectrum of decay positrons with several energies will be simulated.

#### Beam positron data

In order to evaluate the validity of the Monte Carlo, the data with beam positrons was taken with several momenta and 2 incident angles ( $0^\circ$ ,  $45^\circ$ ,  $0^\circ$  being straight beam). The PIENU-1 detector [§3.2.8] was removed and only WC1, WC2, WC3, T2, the NaI calorimeter and the CsI calorimeter were left, to simulate positrons which coming from the target. Fig.6.4 shows the picture of the setup.

The data point which were taken with this setup are below.

- $0^\circ$ : 70 MeV, 40 MeV, 30 MeV, 20 MeV, 10 MeV
- $45^\circ$ : 70 MeV, 35 MeV

These data sets are used to evaluate the Monte Carlo validity.

#### Monte Carlo

**Energy resolution** The energy resolution of the detector need to be implemented into the Monte Carlo. The resolution is obtained from the beam positron data with  $0^\circ$  by fitting the higher region of each peak with a Gaussian as shown Fig.6.5. The energy distribution of each energy is not consistent with a Gaussian and the  $\sigma$  which is obtained from the fit might be not so accurate. Fig.6.6 shows the resolution ( $\sigma$ ) as a function of the positron energy. Normally resolution of calorimeter should be described with the equation below.

$$\sigma = \sqrt{\sigma_{ph}^2 E + \sigma_{fixed}^2} \quad (6.1)$$

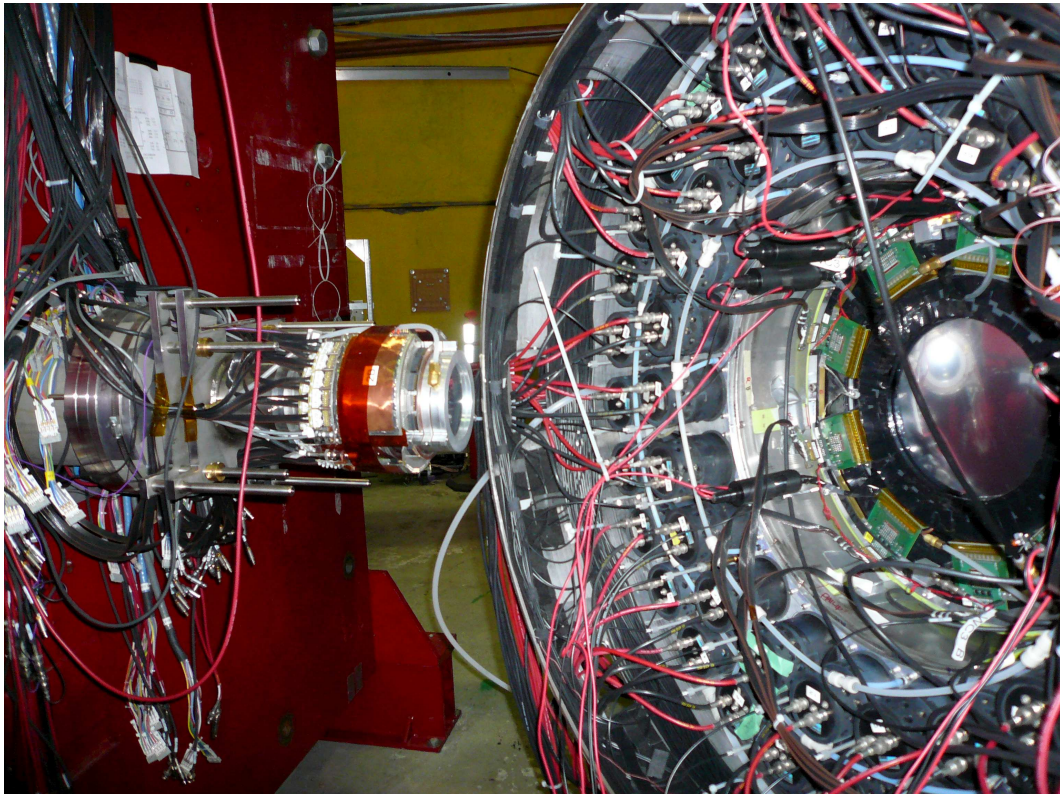


Figure 6.4: Detector setup for beam positron data. The PIENU-1 detector is removed and only WC1, WC2, WC3, T2, the NaI calorimeter and the CsI calorimeter are left.

Where,  $E$  is the energy deposit in the calorimeter,  $\sigma_{ph}$  is a component which is affected by photon statistics and  $\sigma_{fixed}$  is a component which has no correlation with the energy deposit. However Fig.6.6 is not consistent with this equation. Instead of using the equation, the points are fitted with a polynomial function which is drawn as blue line in Fig.6.6. The function is used as a detector resolution in the Monte Carlo. The consistency of data and the Monte Carlo is discussed afterwards.

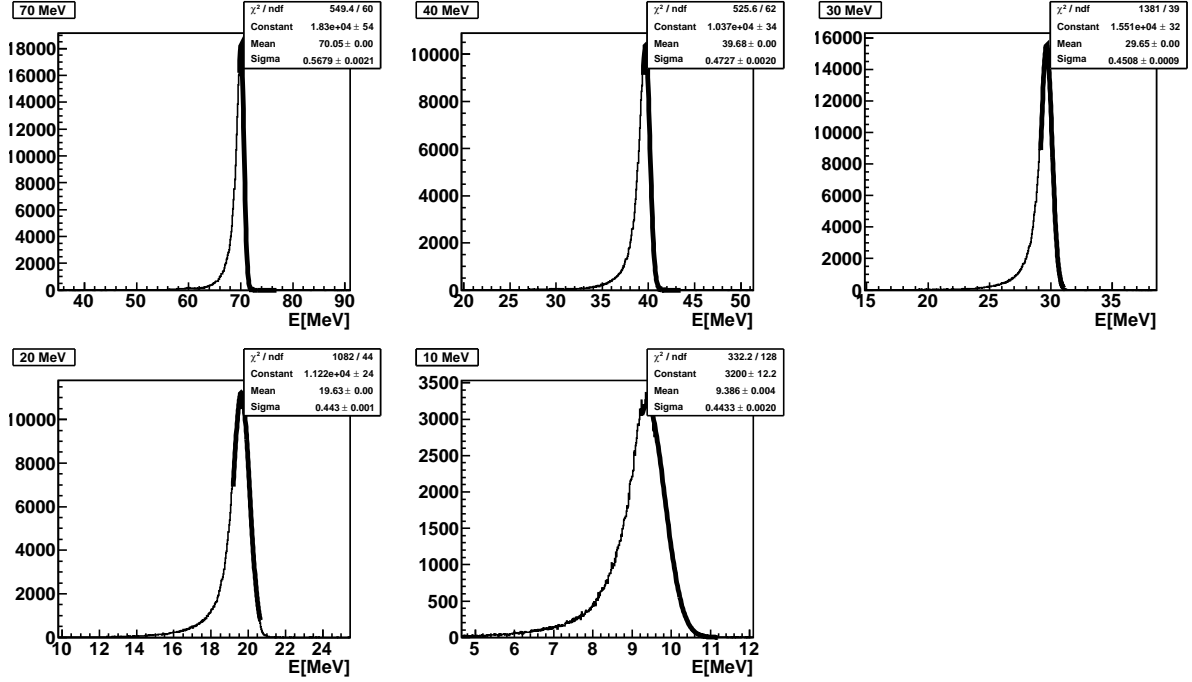


Figure 6.5: Positron energy distribution at different momenta

**Comparison of data and Monte Carlo with  $\pi^+ \rightarrow e^+ \nu_e$  decay** In order to obtain the positron energy spectrum of normal  $\pi^+ \rightarrow e^+ \nu_e$  decay, a Monte Carlo with 70 MeV positrons which start from pion stop position in the experimental data and have a random momentum direction is prepared. The left figure in Fig.6.7 shows the positron spectra, the black line is Suppressed-Spectrum and the red line is the Monte Carlo result. All the Histograms are normalized with the maximum height. In the Monte Carlo, the same fiducial cut in WC3 (Radius < 8 cm) and CsI-Veto-Cut is applied. The exact energy threshold of CsI-Veto-Cut is not known because the energy calibration of the CsI calorimeter was not done at the time of this analysis. The veto threshold is set to 6 MeV in the Monte Carlo to have a similar shape than the data. In order to obtain a more similar spectrum than the data, the low energy tail of the Monte Carlo result is scaled with a factor of 1.08. The green line shows the Monte Carlo spectrum with the correction. The corrected Monte Carlo spectrum is almost the same or a bit wider than the data. The right figure shows the same histograms but normalized with the number of event. The amplitude of the peak corresponds to the sharpness of the spectrum. In order to obtain conservative upper limit, the Monte Carlo spectrum should be wider than the data. The amplitude of the corrected Monte Carlo spectrum is about 8% lower than the data.

Basically the positron energy spectrum at lower energy can be obtained by changing the initial energy of positron in the Monte Carlo. However the effect of changing the positron energy should be

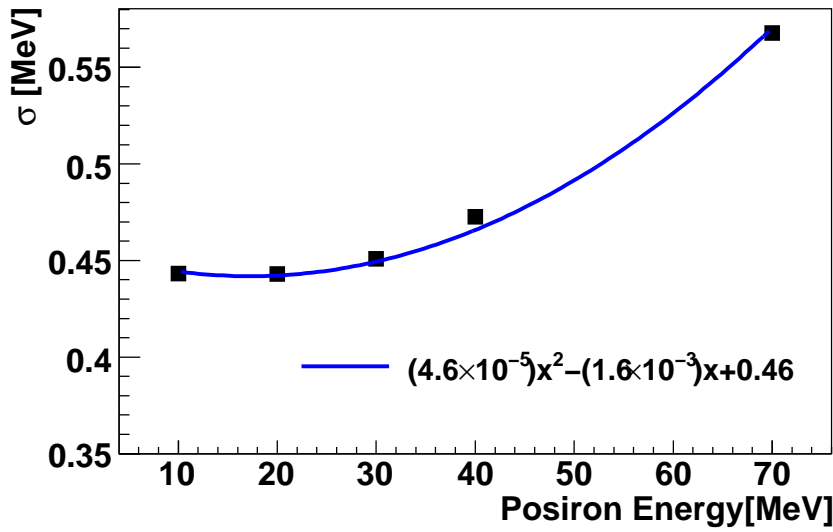


Figure 6.6: Positron energy resolution as a function of energy

compared to the data.

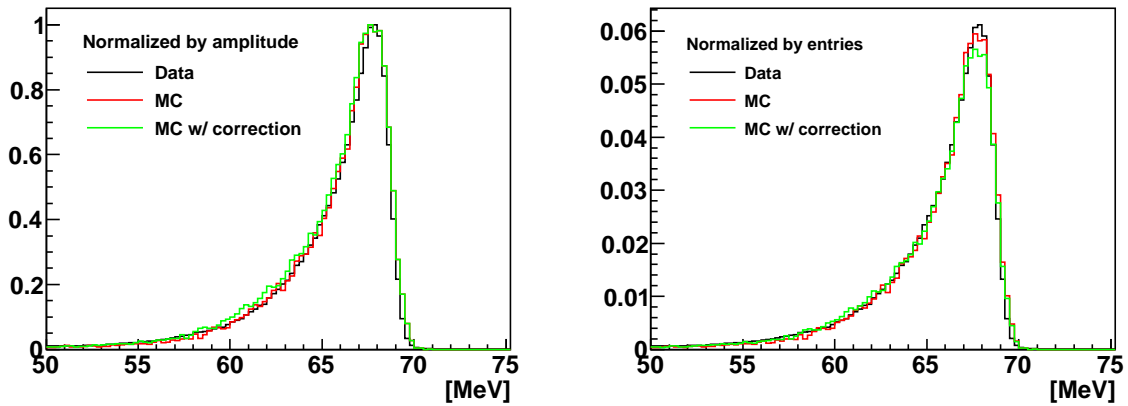


Figure 6.7: Positron energy spectrum of  $\pi^+ \rightarrow e^+ \nu_e$  decay. Black:Data. Red:Raw Monte Carlo. Green:Monte Carlo with correction.

**Study of energy dependence effect to the spectrum shape** The shape the of positron energy spectrum could have some energy dependence. At first, the energy resolution charges with the amount of energy deposit in the NaI calorimeter. Also, shower leak effect may have an energy dependence. The top 2 histograms in Fig.6.8 show the energy spectra of beam positrons with different momenta at  $0^\circ$ . The right histograms show the data and the left histograms show the Monte Carlo. It is known that low energy tail of the spectra becomes wider when the energy decreases and high energy tail also becomes wider due to energy resolution effect. The bottom right histogram in Fig.6.8 shows maximum amplitude

normalized with the entries (AMP/ENT) of each spectrum. The binning of the spectra are the same and AMP/ENT corresponds to the sharpness of the spectrum. The bottom left histogram in Fig.6.8 shows relative AMP/ENT compared to 70 MeV. Fig.6.9 shows the same things at  $45^\circ$ . In both the data and the Monte Carlo, the shape is getting wider when the energy decreases and relative AMP/ENT of the Monte Carlo are always smaller than the data. This means that the Monte Carlo always estimate the shape conservatively.

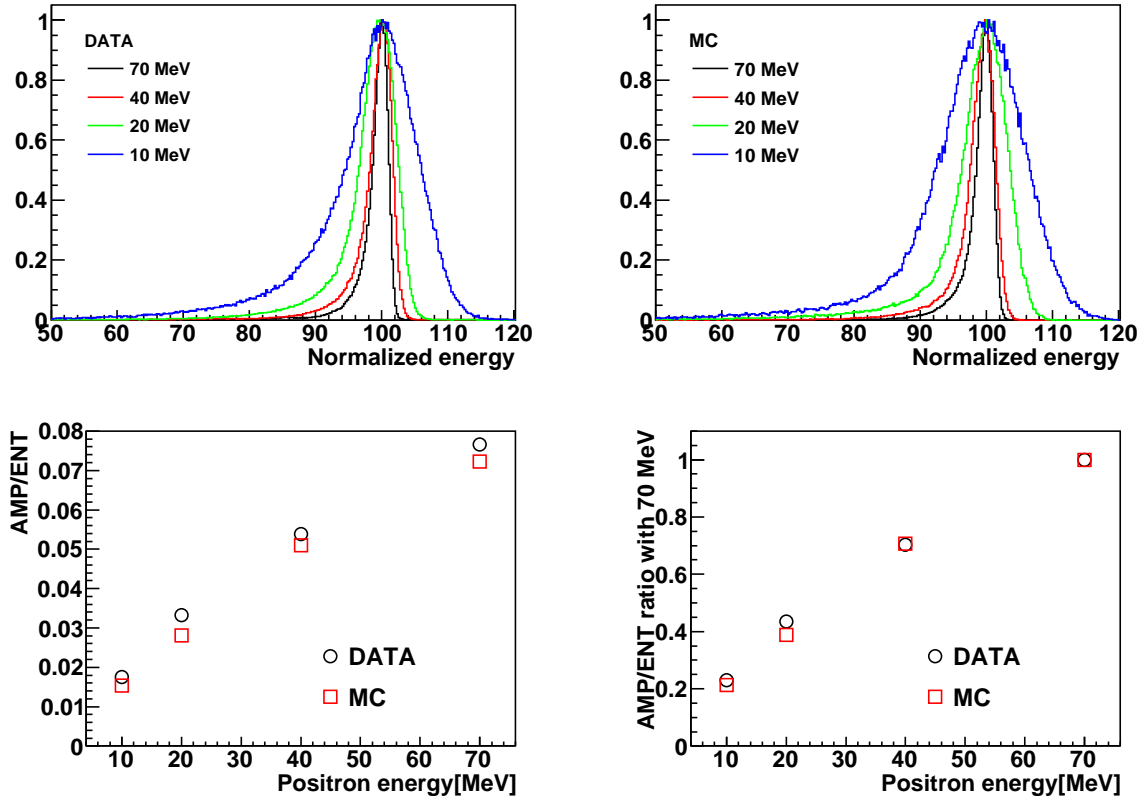


Figure 6.8: The energy spectra of beam positrons with different momenta at  $0^\circ$ . The top figures are the spectrum and the bottom figures are the amplitude normalized with the entries. The left figures are the data, and The right figures are the Monte Carlo.

**Signal Monte Carlo** Positrons with a random momentum direction are simulated with the Monte Carlo by changing the energy (Signal MC). The positron start position is the same as the pion stop position in the data. The top figures in Fig.6.10 shows the positron energy spectra. The shape becomes broader with decreasing of the positron energy. The bottom 2 figures in Fig.6.10 shows AMP/ENT of the spectra as a function of the positron energy. These spectra will be used for spectrum fitting as the shape of the positron from the pion decay with massive neutrinos. The upper limits which are evaluated with these spectra become conservative result because it is known that the shape is broader than the data.

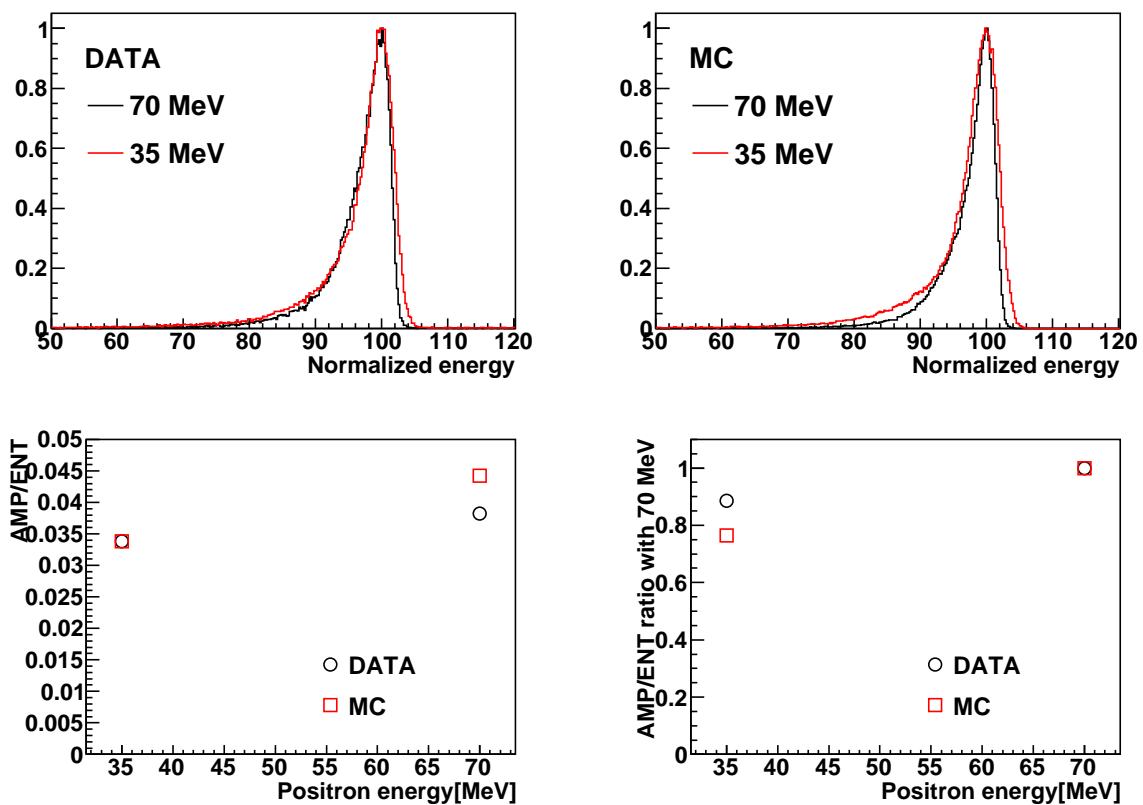


Figure 6.9: The energy spectra of beam positrons with different momenta at  $45^\circ$ . The top figures are the spectrum and the bottom figures are the amplitude normalized with the entries. The left figures are the data, and The right figures are the Monte Carlo.

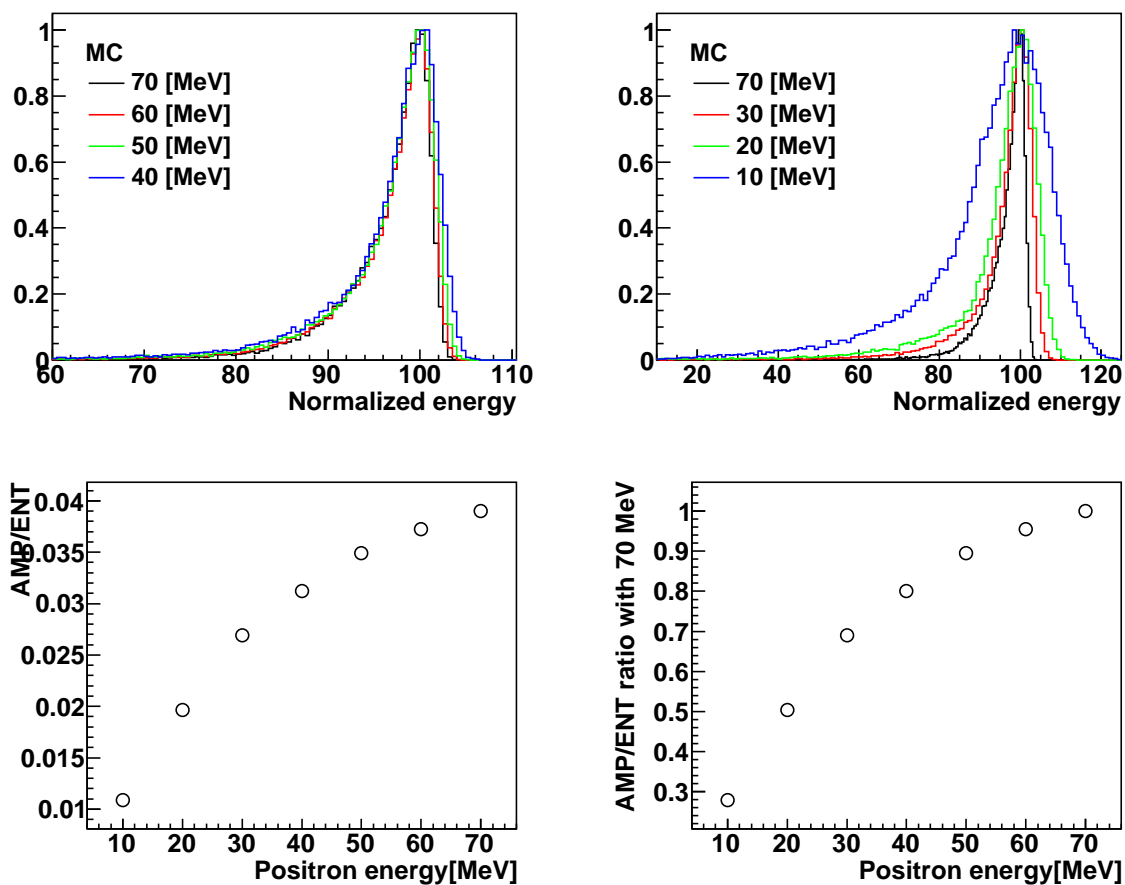


Figure 6.10: Energy spectrum of the positrons with a random momentum direction (Signal MC). Top: the positron energy spectra with several momenta. Bottom left: AMP/ENT as a function of the energy. Bottom right: Relative AMP/ENT compared to 70 MeV as a function of the energy.

## 6.2 Spectrum fitting

Search for massive neutrinos is done by fitting Suppressed-Spectrum in this section. First of all,  $\pi \rightarrow \mu \rightarrow e$   $\mu$ DAR component is subtracted from the spectrum, because the spectrum shape of it is well known from the data and the amount in Suppressed-Spectrum can be estimated with time spectrum fitting. Then the massive neutrino search is done by fitting the spectrum.

### 6.2.1 Subtraction of $\pi^+ \rightarrow \mu^+ \rightarrow e^+$ muon decays-at-rest event ( $\mu$ DAR)

#### Amplitude estimation of $\mu$ DAR

**$\pi$ DIF and  $\pi$ DAR in  $\mu$ DAR** Fig.6.11 shows the likelihood distribution which were obtained by pulse shape fitting (PS-Likelihood). [§5.3] The blue line in the left histogram shows the events which have more than 52 MeV in Suppressed-Spectrum which are mainly  $\pi^+ \rightarrow e^+ \nu_e$  decay. The red line in left histogram shows the events which have less 30 MeV in Suppressed-Spectrum which are mainly  $\pi^+ \rightarrow \mu^+ \rightarrow e^+$  decay. The purple line shows the cut value (-8.4) which was used to obtain Suppressed-Spectrum. The red line in right histogram shows  $\pi^+ \rightarrow \mu^+ \rightarrow e^+$  pion-decay-at-rest ( $\pi$ DAR) sample which is made by not applying Total-Energy-Cut.

$\mu$ DAR events in Suppress-Spectrum are  $\pi$ DIF or  $\pi$ DAR events. [§2.5] If it is  $\pi$ DIF, PS-Likelihood should have the same shape as  $\pi^+ \rightarrow e^+ \nu_e$  decay and if it is  $\pi$ DAR, it should have the same shape as right histogram in 6.1. However, in the histogram of  $\pi^+ \rightarrow \mu^+ \rightarrow e^+$  background ( $<30$  MeV) the DAR component looks small. This mean that  $\pi^+ \rightarrow \mu^+ \rightarrow e^+$  background is mainly  $\pi$ DIF events. Therefore, the mout of  $\pi$ DAR events which are left in Suppressed-Spectrum is estimated by using the PS-Likelihood distribution of  $\pi$ DAR sample. The number of event in -20 to -10 in the PS-Likelihood histogram of  $<30$  MeV sample is 0.8% of the events in -8.4 to 0. And the ratio of number of event in -20 to -10 and -8.4 to 0 in the PS-Likelihood histogram of DAR events is 1.27 Thus the events which are left in the suppress spectrum is  $0.8\% \times 1.27 = 1.02\%$ . Therefore about 99% of the  $\pi^+ \rightarrow \mu^+ \rightarrow e^+$  background are  $\pi$ DIF event.

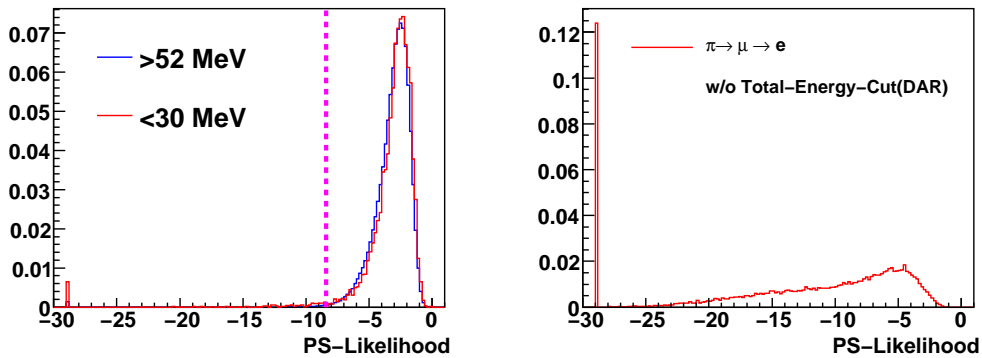


Figure 6.11: PS-Likelihood distribution. Blue line in left histogram: Events which have more than 52 MeV in the suppressed spectrum. Red line in left histogram : Events which have less 30 MeV in suppressed spectrum. Purple line shows the cut value (-8.4) to obtain Suppressed-Spectrum Right histogram: $\pi$ DAR sample which is made by not applying Total-Energy-Cut.

**Time spectrum** Fig.6.12 shows time spectrum (time difference between positron and pion) of the events which have less than 52MeV in Suppressed-Spectrum. First 3 histograms shows different run period and bottom left histogram shows all the data. The events which have less than 52MeV in Suppressed-Spectrum include low energy tail of  $\pi^+ \rightarrow e^+ \nu_e$ ,  $\mu$ DAR and  $\mu$ DIF. And as discussed above,  $\pi^+ \rightarrow \mu^+ \rightarrow e^+$  events are mostly  $\pi$ DIF events. Therefore the time spectrum should have two life time component. One is pion lifetime (26ns) which is due to  $\pi^+ \rightarrow e^+ \nu_e$  decay and  $\mu$ DIF in which muon and positron has the same timing. The other is muon lifetime (2.2 $\mu$ s) which is due to  $\mu$ DAR. Thus the amplitude of these two components can be extracted by fitting. The time spectra are fitted with the function below.

$$F(t) = Aexp(t/26.03) + Bexp(t/2197) \quad (6.2)$$

The blue line is the pion lifetime component and the red line is the muon lifetime component. As shown in the histograms, events in the time window between 2 ns and 6 ns are missed in some run (run9000~10024, run13271~run17800) due to the trigger logic problem. The amount of  $\pi^+ \rightarrow \mu^+ \rightarrow e^+ \mu$  DAR events in the region between 7 ns and 33 ns is estimated with the fitting result of the histogram with full data. The amount of  $\pi^+ \rightarrow \mu^+ \rightarrow e^+ \mu$  DAR events before 7 ns is estimated by using the fitting result of the histograms of each run period. The estimated amount of the  $\pi^+ \rightarrow \mu^+ \rightarrow e^+ \mu$  DAR events in Suppressed-Spectrum is:

- $N_{\pi\mu e}=17960$  events  $\pm 4.0\%$

The error is estimated from the error on the fit amplitude.

#### **Subtraction of $\pi^+ \rightarrow \mu^+ \rightarrow e^+$ muon decay-at-rest event**

The  $\mu$ DAR background in Suppressed-Spectrum is subtracted by using the amplitude and the spectrum shape which were obtained previously. Fig.6.13 shows Suppressed-Spectrum before and after the subtraction of the  $\mu$ DAR background. The top histogram is in log-scale and the bottom histogram is in linear scale which focus on the tail region. The red line in bottom histogram is the subtracted  $\mu$ DAR background spectrum. This spectrum will be used for neutrino search.

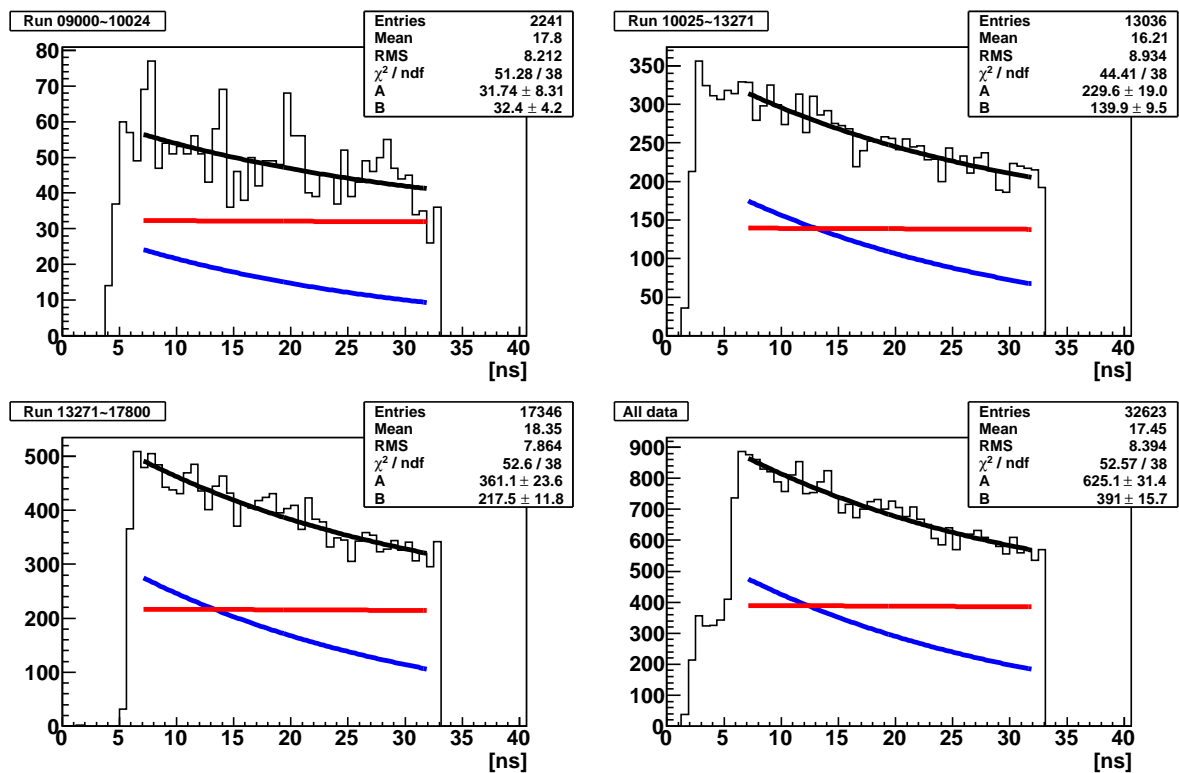


Figure 6.12: Time spectrum of events which have less than 52MeV in Suppressed-Spectrum. The first 3 histograms show different run period and the bottom left histogram shows all the data. The histograms are fitted with the function which consists from pion life time and muon life time components (black line). The blue line is the pion lifetime component and the red line is the muon lifetime component.

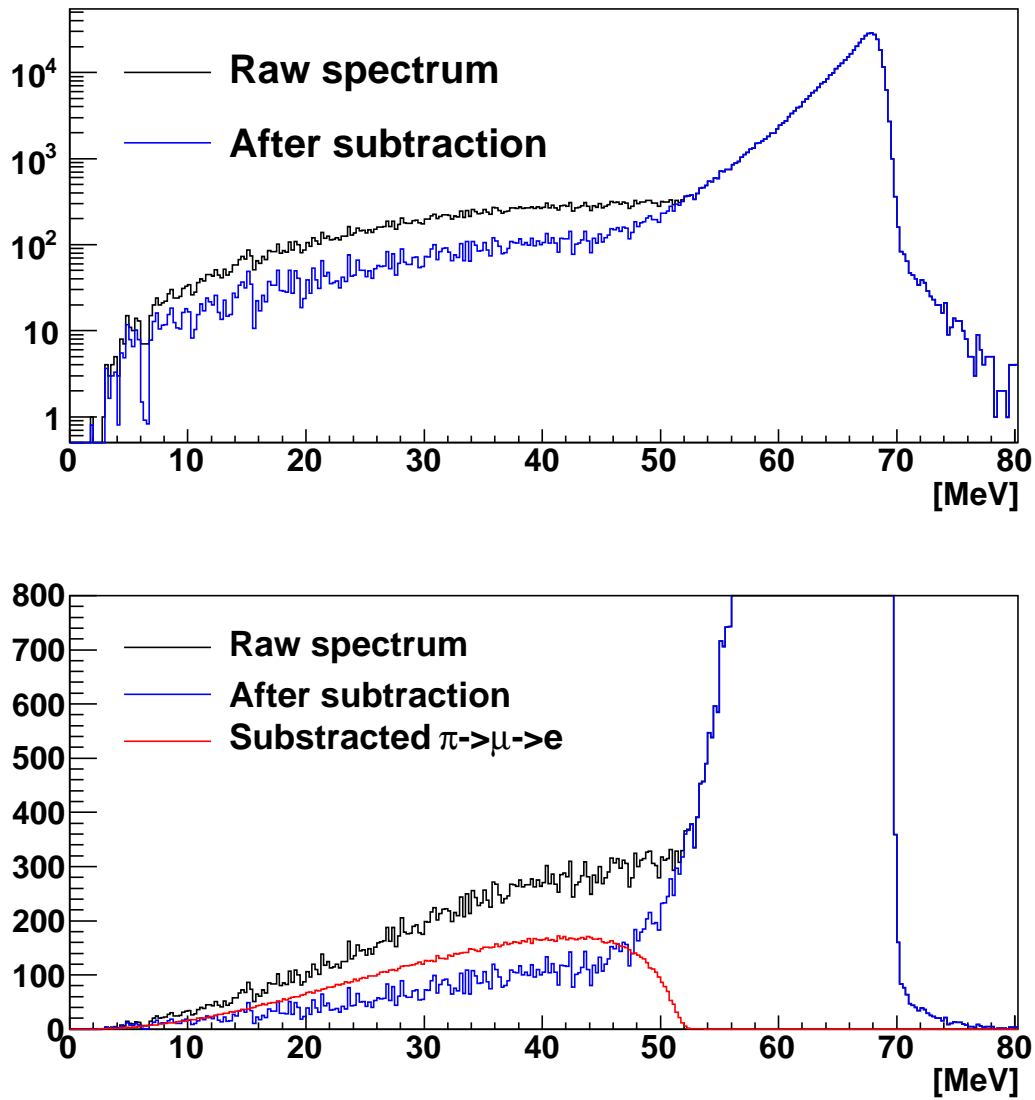


Figure 6.13: Suppressed spectrum before and after  $\mu$ DAR background subtraction. Black line: Raw Suppressed-Spectrum. Blue line: Suppressed-Spectrum after  $\mu$ DAR background subtraction. Red line : Subtracted  $\mu$  DAR background.

### 6.2.2 Spectrum Fitting

The massive neutrino search corresponds to a bump search in Suppressed-Spectrum as described in §2.2. The bumps are search by fitting Suppressed-Spectrum with the bump component and the background component. The fit is done by changing the assumed bump energy. The left background in the spectrum is  $\mu$ DIF and low energy tail of  $\pi^+ \rightarrow e^+\nu_e$  decay. It is known that low energy tail of  $\pi^+ \rightarrow e^+\nu_e$  decay is expected to have some bumps at 62MeV, 53 MeV and 42 MeV as described in §6.1.3. Therefore the energy region from 10 MeV to 40 MeV is used for massive neutrino search.

The fitting window is defined  $\pm 6$  MeV with respect to the searched positron energy. The fit with and without bump is done by using function below.

$$f_{exp}(x) = e^{Ax+B} \quad (6.3)$$

$$f_{exp+bump}(x) = e^{Ax+B} + C f_{bump}(x) \quad (6.4)$$

$$(6.5)$$

The left background in the spectrum is low energy tail of  $\pi^+ \rightarrow e^+\nu_e$  and  $\mu$ DIF. The positron energy spectrum of these background were discussed previously and the spectra has no bump and have monotonic increase. That is why an exponential function is used for fitting of the background component.  $f_{bump}(x)$  is the positron energy spectrum shape which were obtained with the Monte Carlo in § 6.1.4. The fits are done with 0.5 MeV steps.

Fig 6.14 shows the spectra with 5MeV step which are fitted with  $f_{exp}$ . Fig.6.15 shows the spectra with 5 MeV step which are fitted with  $f_{exp+bump}(x)$ .

Left figure in Fig.6.16 shows reduced  $\chi^2$  distribution as function of bump energy. The black circle marker is  $\chi^2$  of the fit without bump and the blue box marker is the fit with bump. The right figure in Fig.6.16 shows the probability of  $\chi^2$  as function of bump energy. The probability of the  $\chi^2$  are good in both  $f_{exp}$  and  $f_{exp+bump}$ . This means that there is only random statistical distortion from the fitted exponential function in the histogram and using exponential function for fitting function of the background component works well.

Fig.6.17 shows bump amplitude obtained from the fit and the amplitudes are consistent with 0. This means no bump is found in the energy region and the fitting assumption is correct. Therefore it is concluded that there is no evidence for massive neutrinos in the energy region between 10 MeV and 40 MeV.

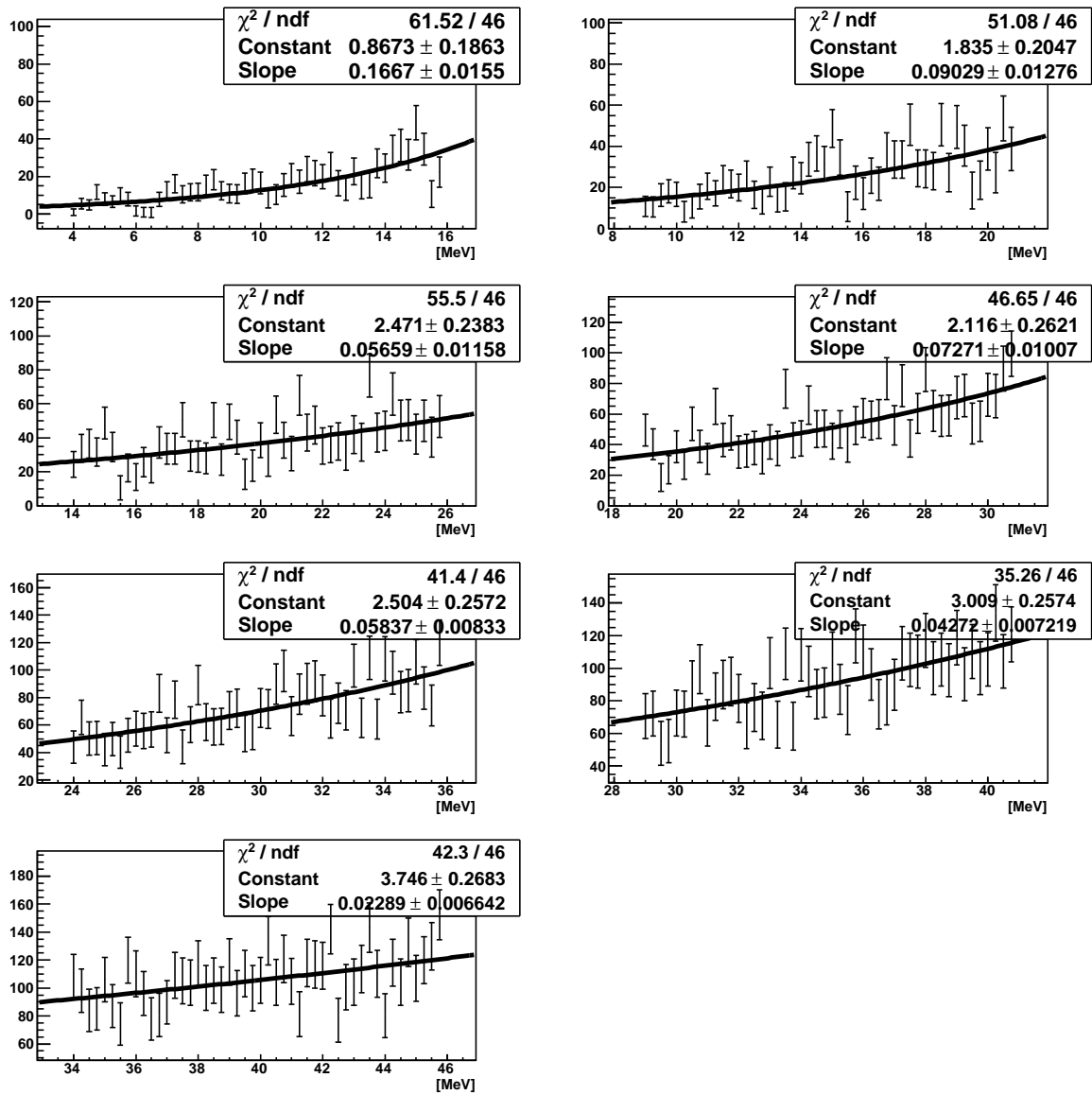


Figure 6.14: Positron energy spectra with 5MeV step which are fitted with just an exponential function.

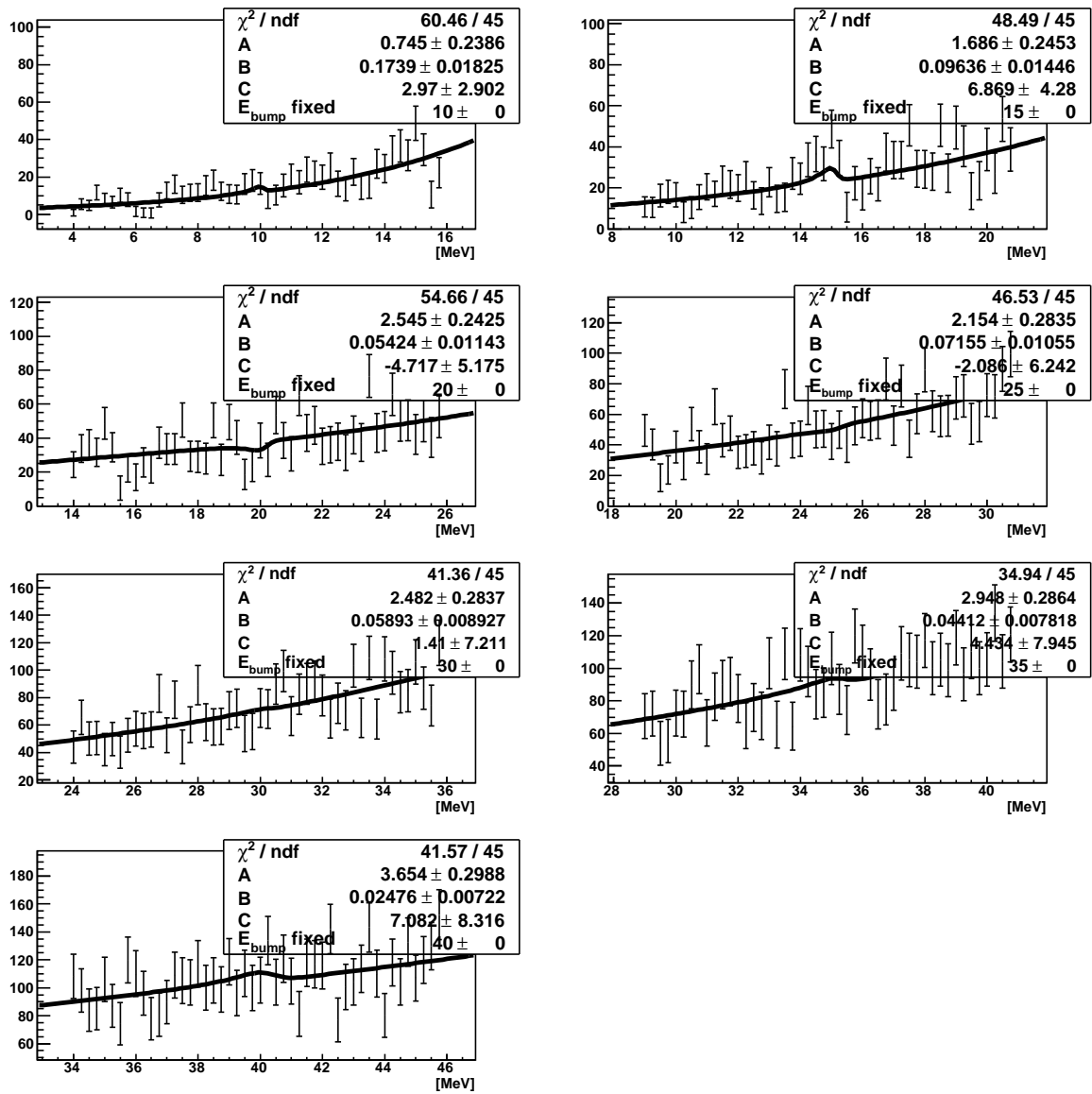


Figure 6.15: Positron energy spectra with 5MeV step which are fitted with  $f_{exp+bump}(x)$ .

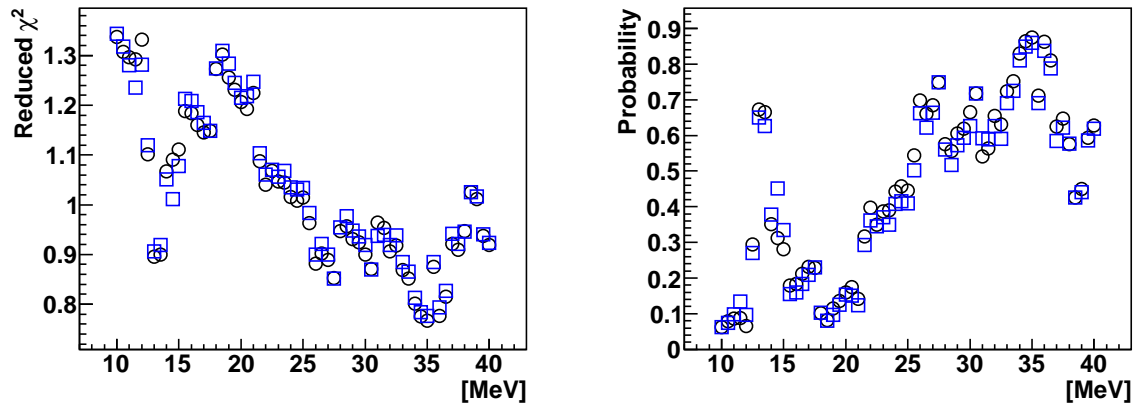


Figure 6.16:  $\chi^2$  and probability of the spectrum fitting. Left: Reduced  $\chi^2$  of the fitting. circles show fit with  $f_{exp}(x)$  and box show fit with  $f_{exp+bump}(x)$  Right: Probability of the fit.

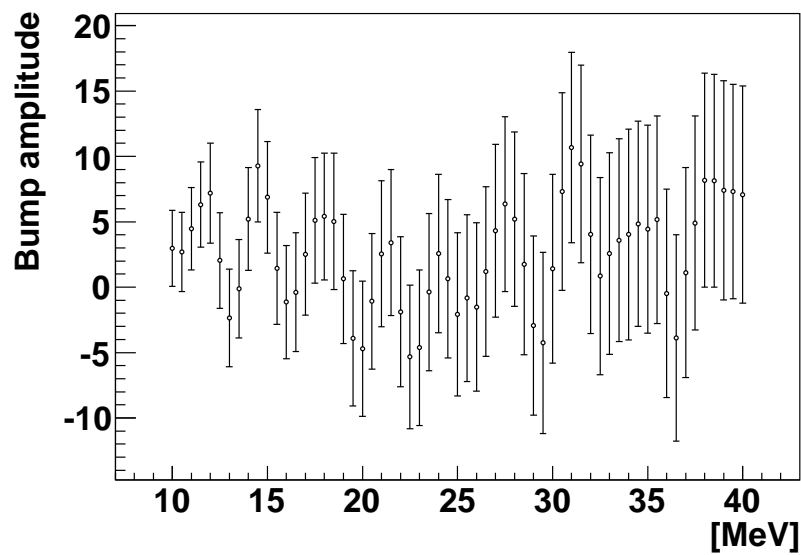


Figure 6.17: Bump amplitude from the spectrum fitting. The amplitudes are consistent with 0. No bump is found from the spectrum fitting.

### 6.2.3 Raw upper limit estimation

In order to estimate upper limits from the fitting result, the Bayes's method is used. First of all, a Gaussian function which have the mean and the error of the fitted result is generated. Fig.6.18 shows an example of the Gaussian function from the result at 10 MeV (mean:3.0,  $\sigma$ :5.8). As described in the figure, the negative region is just ignored and 90% C.L limit is defined by using the integration of the positive region.

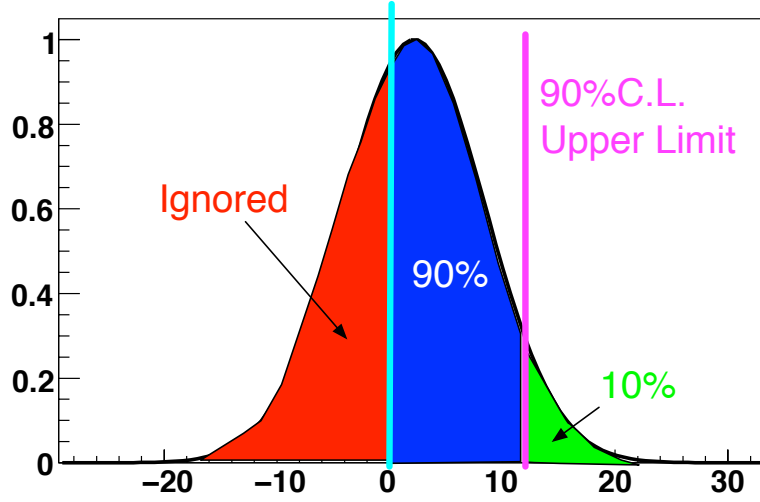


Figure 6.18: The Gaussian function to obtain an upper limit from the fitting result by the Bayes's method

The obtained upper limits are still amplitude of the bumps. The upper limits are converted to the branching ratio by comparing with the number of events in the  $\pi^+ \rightarrow e^+\nu_e$  peak as described below.

$$\frac{\Gamma(\pi \rightarrow e\nu_i)}{\Gamma(\pi \rightarrow e\nu_e)} = \frac{N_{\pi \rightarrow e\nu_i}}{N_{\pi \rightarrow e\nu_e}} \quad (6.6)$$

$$(6.7)$$

$N_{\pi \rightarrow e\nu_e}$  is the number of events which have more than 52 MeV in Suppressed-Spectrum and  $N_{\pi \rightarrow e\nu_i}$  is the integration of  $AMP_{UL} \times f_{bump}(x)$  where  $AMP_{UL}$  is an upper limit of the amplitude which is obtained previously. Fig.6.19 shows obtained upper limits (90% C.L.) of  $\Gamma(\pi \rightarrow e\nu_i)\Gamma(\pi \rightarrow e\nu_e)$  with the procedure. This 'Raw' upper limit should be corrected considering some systematic effect. The systematic correction will be done in the next chapter.

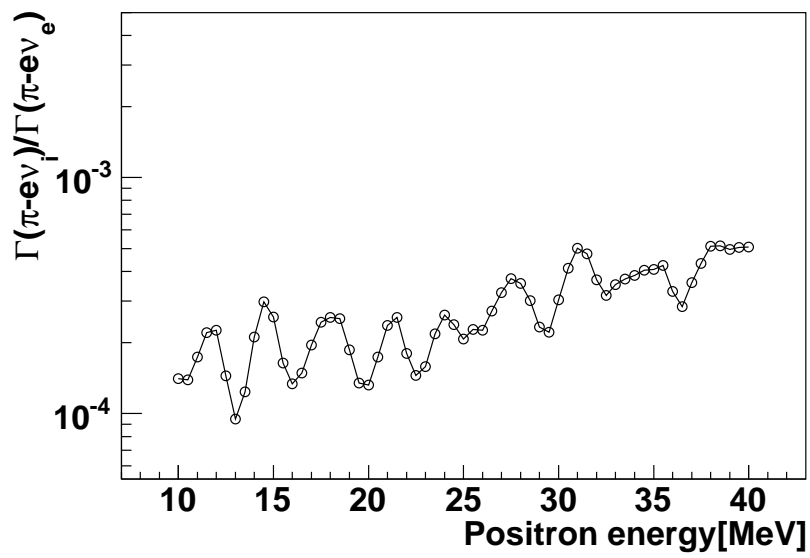


Figure 6.19: Raw upper limits (90% C.L.) of the branching ratio  $\Gamma(\pi \rightarrow e\nu_i)/\Gamma(\pi \rightarrow e\nu_e)$

# Chapter 7

## Systematic corrections

Some systematic corrections are done in this chapter. The upper limit is estimated at the end of this section.

### 7.1 Subtracted $\mu$ DAR amplitude

Before fitting the spectrum,  $\mu$ DAR component was subtracted from Suppressed-Spectrum in §6.2.1. The amplitude of the subtracted  $\mu$ DAR spectrum was obtained with time spectrum fitting with  $\pm 4\%$  error, it might have some systematic effect to the spectrum fitting results. The spectrum fitting by changing the amplitude  $\pm 10\%$  is done and the raw upper limits are shown in Fig.7.1. The raw upper limits become about 3% worse when the amplitude is -10%. The biggest difference of the raw upper limit is 5.3% and it will be used as correction factor for upper limit estimation.

### 7.2 Purity of $\pi^+ \rightarrow e^+\nu_e$ decay

In order to obtain the raw upper limit of  $\Gamma(\pi \rightarrow e\nu_i)\Gamma(\pi \rightarrow e\nu_e)$ , the number of events which have more than 52 MeV in Suppressed-Spectrum was used as number of  $\pi^+ \rightarrow e^+\nu_e$  decay. Therefore the amount of background which have more than 52 MeV in Suppressed-Spectrum should be evaluated. It is done by using the time spectrum.

One possible background is pileup of  $\pi^+ \rightarrow \mu^+ \rightarrow e^+$  events which increase with pion lifetime and decrease with muon lifetime. Fig.7.2 shows the time spectrum of the events which have more than 52 MeV without Timing-Cut. The histogram is obtained with 1/30 of the full data set. We can see that there are few events after 200 ns (7.7 pion lifetime). This means that there is almost no background events. The peak which is about 290 ns is due to prescale factor of 16 §3.3. The number of events in 200~ 500 ns is 28 events and the expected background in the 2~ 33 ns which is used for the analysis is 3.0 events with the assumption that the time distribution of the background is flat. The number of events in 2~ 33 ns is 15362 events. That is why the background amount is about 3.0/15362=0.02%.

There is another background which is the higher energy tail of positron from the  $\mu$ DIF events as shown in Fig.2.11 It has pion life time and is not included the background which evaluated above. It is known that the amount of the background is about 0.12% which is about 6% of all the  $\mu$ DIF events. In total, 1% correction will be used as the conservative amount of background for the upper limit estimation.

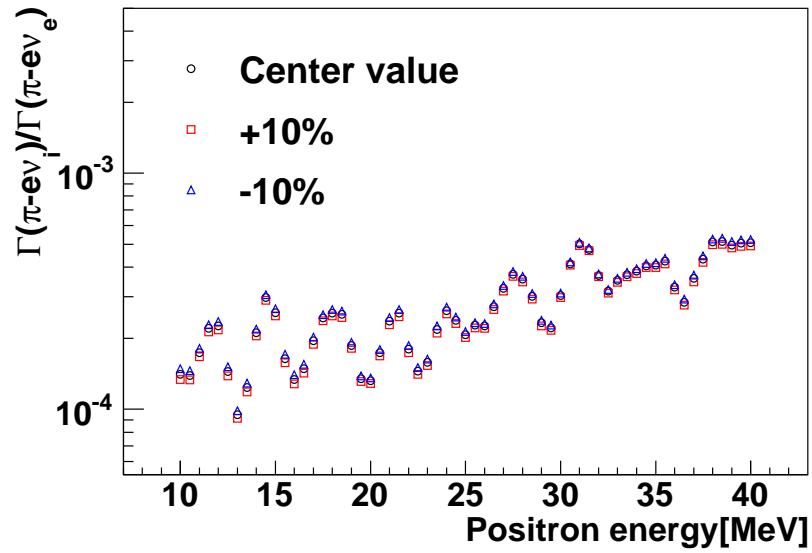


Figure 7.1: Raw upper limits (90% C.L.) of  $\Gamma(\pi \rightarrow e\nu_i)\Gamma(\pi \rightarrow e\nu_e)$  by changing the subtracted  $\mu$ DAR amplitude. The circle marker show the central value, the triangle markers show -10% and the box marker show +10%.

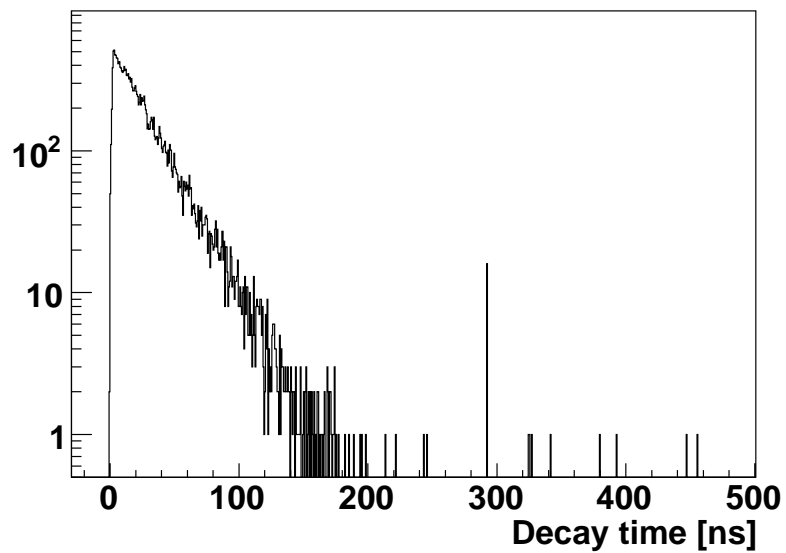


Figure 7.2: Time spectrum of the events which have more than 52 MeV in Suppressed-spectrum.

### 7.3 Acceptance correction

In order to select  $\pi^+ \rightarrow e^+\nu$  decay, several cuts were used in § 4 and § 5. And the upper limits for the existence of massive neutrinos were evaluated as the ratio to the  $\pi^+ \rightarrow e^+\nu_e$  decay. However, the acceptance of the cuts used to obtain the energy spectrum could have a positron energy dependence. That is why the acceptance difference depending on the positron energy should be corrected. The acceptance difference of the cuts is evaluated in this section.

#### 7.3.1 Summary of the cuts

The cuts used to obtain Suppressed-Spectrum are summarized in Table.7.1. No cut used positron energy itself, however the positron energy difference cause some energy deposit difference in the detector and positron tracking can also be changed due to multiple scattering effect. The cuts which used positron energy deposit information and positron track information are checked in Table.7.1. Proton-Cut used the energy deposit in the downstream detectors as shown in Fig.4.13 but the events eliminated by the cut is less than 0.01% (after Early-Time-Window-Cut) and therefore the effect is negligible. The energy dependence effect of the other cuts are studied with the Monte Carlo.

Cut	Acceptance(in total)	Positron info
Cut for pion decay event selection		
Number-Of-Hit-Cut	65.4%(65.4%)	
Q/Qw-Ratio-Cut	99.5%(65.1%)	
Timing-Consistency-Cut	96.1%(62.6%)	
Pre-Pileup-Cut	76.7%(48.0%)	
dE-TOF-Vut	91.0%(43.7%)	
Proton-Cut	99.1%(43.3%)	○
Profile-Cut	96.5%(41.8%)	
Early-Time-Window-Cut (2-33ns)	14%(5.9%)	
Ss3-Hit-Cut	90%(5.3%)	
CsI-Veto-Cut	89%(4.7%)	○
Fiducial-Cut	81%(3.8%)	○
Cut for $\pi^+ \rightarrow \mu^+ \rightarrow e^+$ suppression		
Acceptance is defined to $\pi^+ \rightarrow e^+\nu_e$ sample		
Total-Energy-Cut	80%(80%)	○
Incident-Angle-Cut	96%(77%)	○
Rmin-Cut	84%(65%)	○
Zmin-Cut	86%(56%)	○
PS-Cut	100%(56%)	

Table 7.1: Summary of the cuts

#### 7.3.2 Monte Carlo estimation

The energy dependence effect of the acceptance is studied with the Monte Carlo which was used in §6.1.4. The validity of the Monte Carlo is described in the next sub-section.

### Fiducial-Cut

Fiducial-Cut is there is a hit in every detector and the radius of the hit position in WC3 is less than 80mm. The only possible reason why the positron acceptance with this cut has energy dependence is multiple scattering effect. Fig.7.3 shows the acceptance of several energy positrons compared to 70 MeV positrons with Fiducial-Cut which is obtained with the Monte Carlo. The acceptance increases with decreasing positron energy about a few percent when the energy is less than 20 MeV.

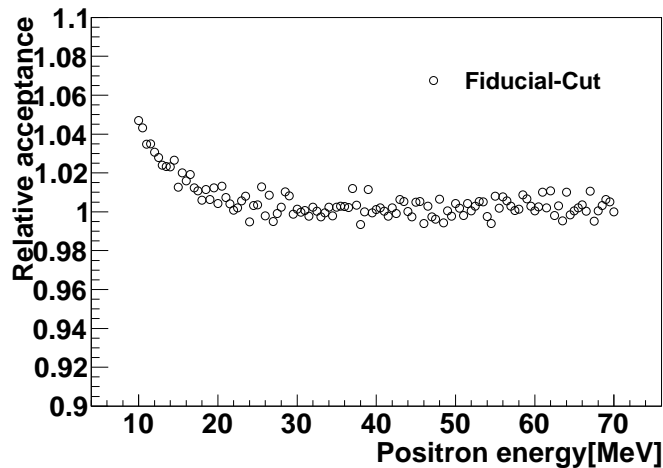


Figure 7.3: Relative acceptance of Fiducial-Cut compared to 70 MeV positron of the positron energy

### CsI-Veto-Cut

CsI-Veto-Cut kills the events which have shower leakage in the CsI calorimeter and the threshold is about 6 MeV. If the positron energy becomes lower, the energy of shower leakage also becomes lower and therefore the acceptance becomes larger. Fig.7.4 shows acceptance of several energy positrons compared to 70 MeV positron with CsI-Veto-Cut and Fiducial-Cut. The acceptance increases with decreasing positron energy.

### Total-Energy-Cut

Total-Energy is the sum of the energy deposit in B1, B2, S1, S2, and Target. It includes pion kinematic energy and positron energy deposit in the target. That is why if the energy deposit of the positrons changes depending on the energy, it will cause a difference in the acceptance. The left histograms in Fig.7.5 shows the positron energy deposit in the target as a function of the positron energy. It is known that the higher energy side tail increase with decreasing positron energy. This means that the lower energy positron have lower acceptance with the cut. In the Monte Carlo the cut is applied to the positron energy deposit in the target (dE-Cut) instead of Total-Energy-Cut because there is no pion in the Monte Carlo [§6.1.4]. The cut value is defined as the mean + 0.7 MeV which is the same as the data and is shown as a purple line in Fig.7.5. The right figure in Fig.7.5 shows the acceptance of several energy positrons compared to 70 MeV positrons with the cut. The circle markers show the effect of

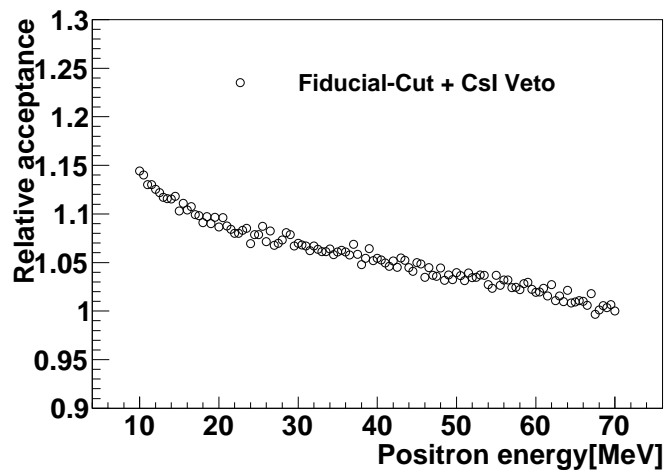


Figure 7.4: Relative acceptance of CsI-Veto-Cut and Fiducial-Cut compared to 70 MeV positron as a function of the positron energy.

all the cuts and the box marker shows the acceptance effect of dE-Cut. The acceptance decreases with decreasing positron energy for dE-Cut.

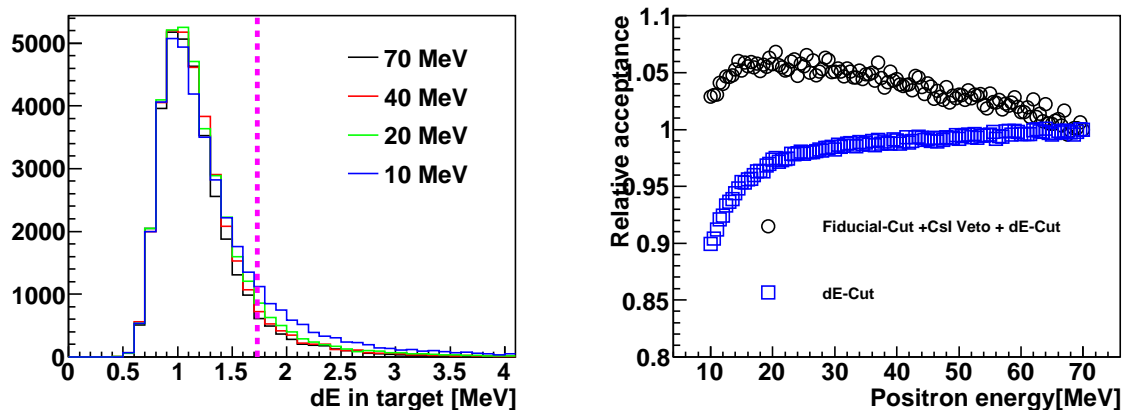


Figure 7.5: Acceptance with Total-Energy-Cut as a function of positron energy. Left: Positron energy deposit in the target. Right: Relative acceptance compared to 70 MeV for dE-Cut.

### Rmin-Cut

Rmin is the minimum distance between the pion track and the positron track as described in §5.2.2. In order to calculate Rmin from the X-Y position information in the Monte Carlo, the pion track is assumed to have no angle and the same X-Y position as the positron start position although there is no actual pion track in the Monte Carlo. Left histograms in Fig.7.6 shows the Rmin distribution as a function of the positron energy. It is known that the higher side tail increases with decreasing positron

energy because multiple scattering effect become larger with decreasing positron energy. This means the lower energy positrons have a lower acceptance with this cut. The cut value is the same as the data cut value which is shown as a purple line in Fig.7.6. The Right figure in Fig.7.6 shows the acceptance of several energy positrons compared to 70 MeV positrons with the cut. The circle markers show the effect of all the cut, the box markers show the effect of only Rmin-Cut and triangle markers show the effect of dE-Cut and Rmin-Cut. The acceptance decreases with decreasing positron energy for Rmin-Cut.

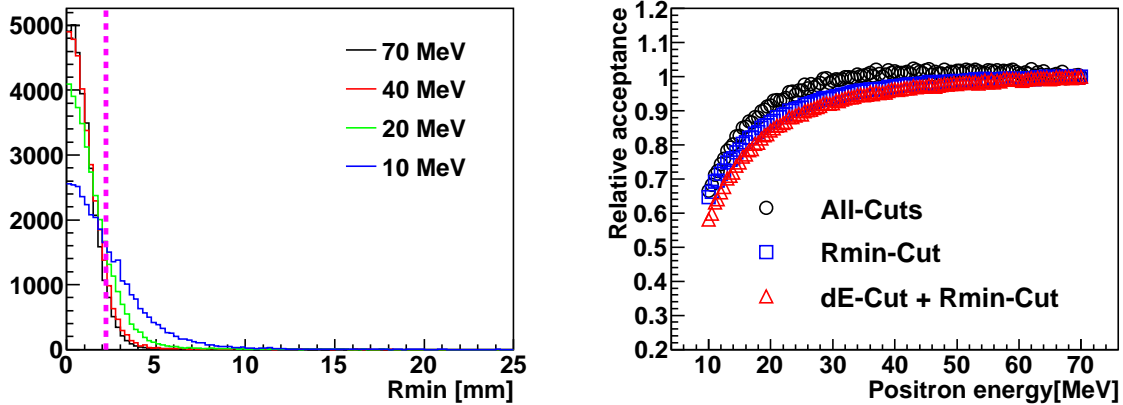


Figure 7.6: Acceptance with Rmin-Cut as a function of positron energy. Left:Rmin distribution as a function of positron energy. Right:Relative acceptance compared to 70 MeV for Rmin-Cut.

### Zmin-Cut

Zmin is the Z position where the pion track and the positron track have a minimum distance. In order to calculate Rmin from the X-Y position information in the Monte Carlo, the pion track is assumed to have no angle and the same X-Y position as the positron start position although there is no actual pion track in the Monte Carlo. The left histograms in Fig.7.7 shows Zmin distribution as a function of positron energy. It is known that the Zmin distribution become wider with decreasing positron energy because multiple scattering effect become larger with decreasing positron energy. This means lower energy positrons have lower acceptance with this cut. The cut value is the same as the data cut value which is shown as a purple line in Fig.7.7. The right figure in Fig.7.7 shows acceptance as a function of positron energy compared to 70 MeV positron with the cut. The circle markers show the effect of all the cut, the box markers show the effect of only Zmin-Cut and the triangle markers show the effect of dE-Cut, Rmin-Cut and Zmin-Cut. The acceptance decreases with decreasing positron energy for Zmin-Cut.

### Summary

The positron energy dependent acceptance difference of the cuts were studied with the Monte Carlo. The acceptance of Fiducial-Cut and CsI-Veto increase with decreasing positron energy. Therefore, the upper limits become conservative if these effects are just ignored. The acceptance of Total-Energy-Cut and Rmin-Cut and Z-min decrease with decreasing positron energy. These effect should be corrected to obtain proper upper limits. The validity of the Monte Carlo is confirmed with the data in the next subsection.

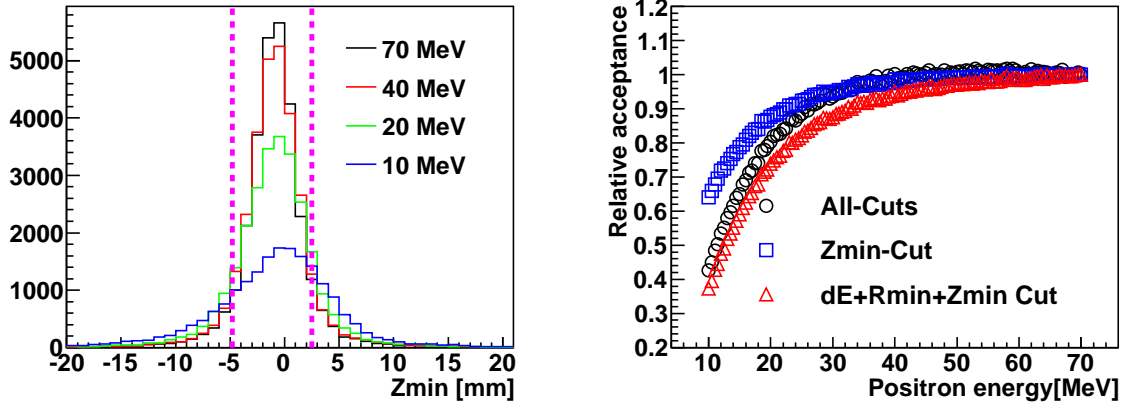


Figure 7.7: Acceptance with Zmin-Cut as a function of positron energy. Left: Zmin of several momenta. Right: Relative acceptance compared to 70 MeV.

### 7.3.3 Validity of the Monte Carlo

The validity of the Monte Carlo to evaluate the energy dependent acceptance difference of the positron is confirmed with the data in this subsection. In order to study positron energy dependent effects,  $\pi^+ \rightarrow \mu^+ \rightarrow e^+$  sample in the data is used because positrons from  $\pi^+ \rightarrow \mu^+ \rightarrow e^+$  decay have a wide range of energy (0~52.8 MeV). In order to compare data and the Monte Carlo,  $\pi^+ \rightarrow \mu^+ \rightarrow e^+$  decay is also simulated with the Monte Carlo. In the Monte Carlo, pions start inside the target with the same position as the data and the kinematic energy of pion is set to 0 MeV. Thus there is no pion track in the Monte Carlo. To simulate tracking information, pion track is assumed to have no angle and the same X-Y position as the pion start position. It is the same procedure for the Monte Carlo of positrons (Signal MC).

Fig.7.8 shows the information about the data. The top left histogram shows Total-Energy and the purple line is the cut which is main peak + 0.7 MeV. The top right is Rmin and the bottom left is Zmin and the purple lines show the cut values. The bottom right shows the positron energy spectrum with the cuts. It is possible to know the positron energy dependent acceptance difference by comparing the acceptance of each bin of the histograms.

Fig.7.9 shows the same histograms for the Monte Carlo. In the Monte Carlo, Total-Energy is the muon kinetic energy and the positron energy deposit in the target.

Fig.7.10 shows the acceptance of the cuts as a function of positron energy. The top histograms are the absolute acceptance of the cuts and the bottom histograms shows relative acceptance compared to 40 MeV. The black line is the data and the red line is the Monte Carlo. The relative acceptance of the Monte Carlo is consistent with the data within 3% although in the low energy region the Monte Carlo results becomes lower. This is acceptable because lower estimation of the relative acceptance results a conservative upper limit.

### 7.3.4 Summary of acceptance correction

The positron energy dependent acceptance difference was evaluated with the Monte Carlo. The effect of Fiducial-Cut and CsI-Veto is just ignored and the effect of Total-Energy-Cut, Rmin-Cut and Z-min

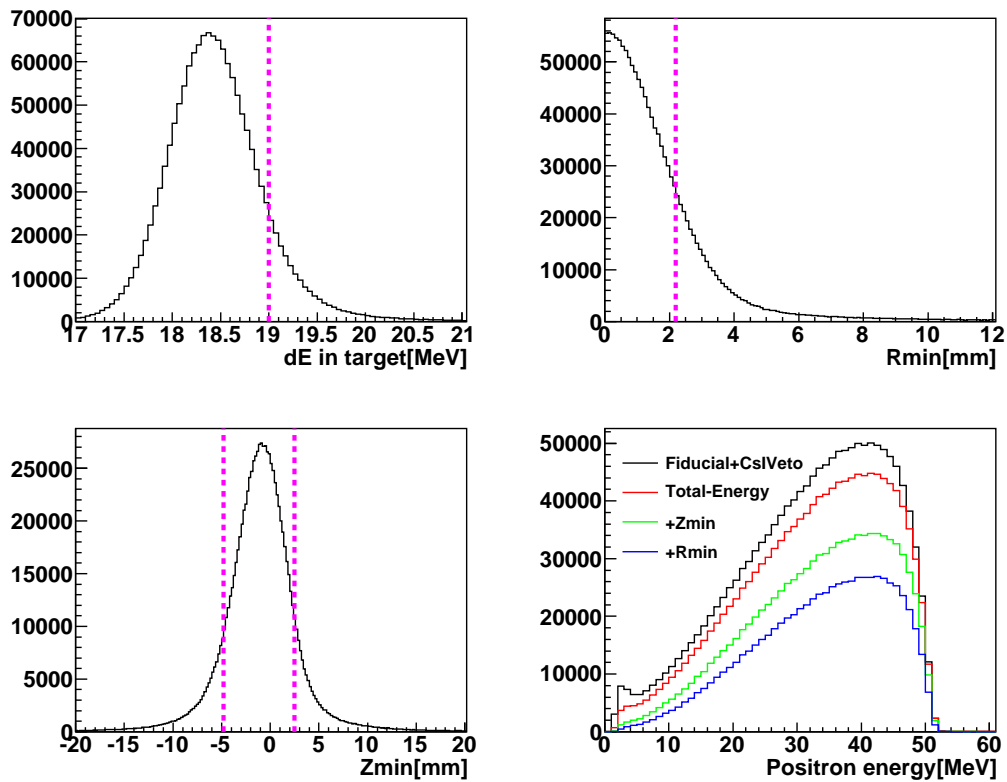


Figure 7.8: Acceptance study of the cuts with positrons from  $\pi^+ \rightarrow \mu^+ \rightarrow e^+$  (DATA). Top left: Total-Energy. Top right: Rmin. Bottom right: Zmin. Bottom left: positron energy spectrum with the cuts. Purple lines show the cut values.

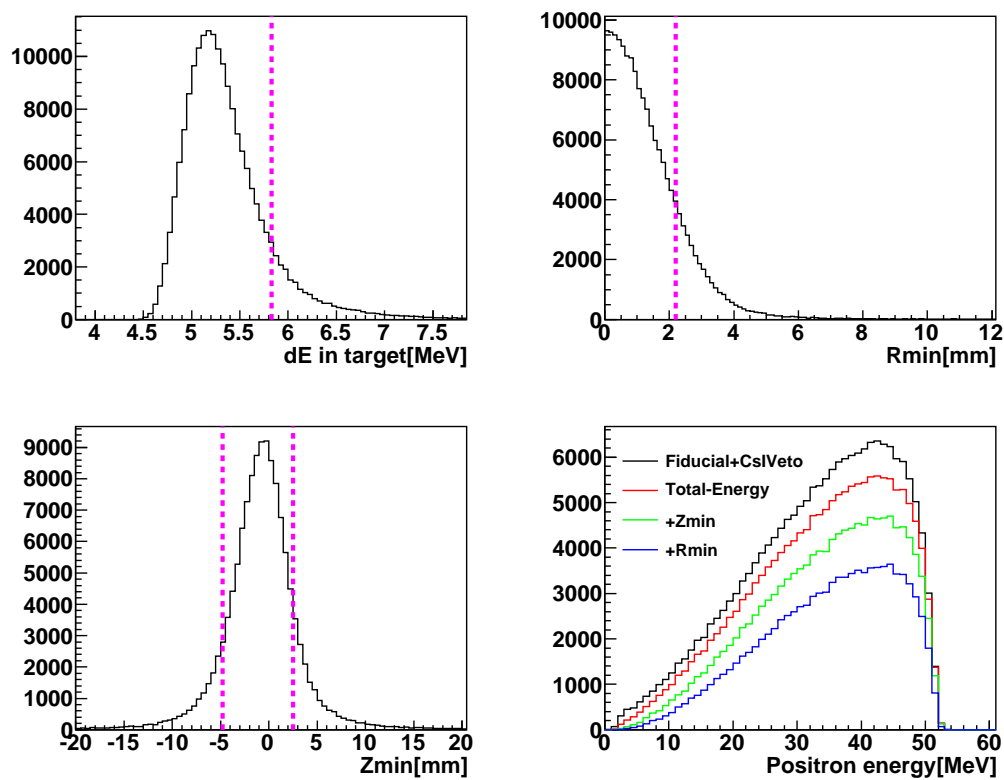


Figure 7.9: Acceptance study of the cuts with positrons from  $\pi^+ \rightarrow \mu^+ \rightarrow e^+$  (MC). Top left: Total-Energy. Top right: Rmin. Bottom right: Zmin. Bottom left: positron energy spectrum with the cuts. Purple lines show the cut values.

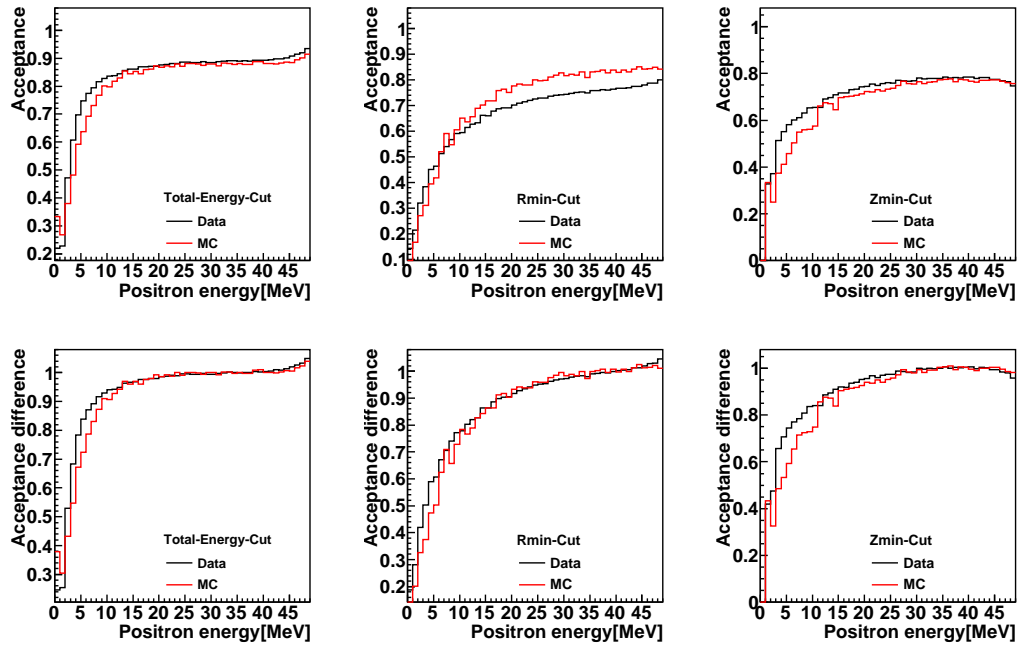


Figure 7.10: Acceptance with the cuts as a function of positron energy. Black line is the data and red line is the Monte Carlo.

which is shown with the red triangle markers in Fig.7.7 will be used as acceptance correction values with 3% correction.

## 7.4 Upper limit estimation

Upper limits (90% C.L.) of  $\Gamma(\pi \rightarrow e\nu_i)\Gamma(\pi \rightarrow e\nu_e)$  are obtained with raw upper limit obtained from the spectrum fitting and the systematic correction value. The systematic correction factors as summarized below.

- Amplitude of subtracted  $\mu$ DAR component : 5.3%
- Purity of  $\pi^+ \rightarrow e^+\nu_e$ : 1.0%
- Acceptance correction :  $1/\text{Acc}(E)$  Acc(E) is values of the triangle marker in Fig.7.7 minus 0.03 (3%).

Thus Upper limits are obtained with the equation below.

$$(\text{UpperLimit}(E)) = ((\text{RawUpperLimit}(E))) \times 1.053 \times 1.01 \times \frac{1}{\text{Acc}(E)} \quad (7.1)$$

Fig.7.11 shows the upper limits (90% C.L.) of the branching ratio  $\Gamma(\pi \rightarrow e\nu_i)/\Gamma(\pi \rightarrow e\nu_e)$ . The black line is before systematic correction and blue line is after systematic correction. Positron energy is converted to neutrino energy in the right histograms with the equation in §1.1

Fig.7.12 shows the upper limit (90% C.L.) of the mixing parameter  $|U_{ei}|^2$  which is obtained with the equation in §1.1.

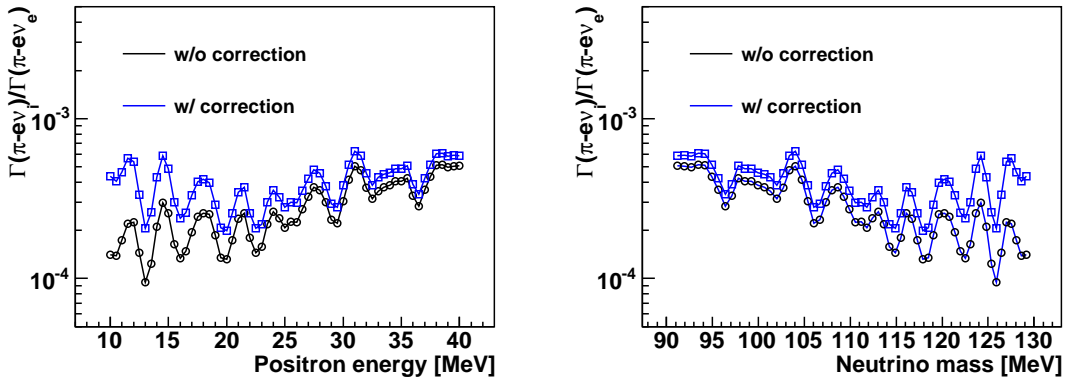


Figure 7.11: Upper limit (90% C.L.) of the branching ratio  $\Gamma(\pi \rightarrow e\nu_i)/\Gamma(\pi \rightarrow e\nu_e)$ . Black line: Before systematic correction. Blue line: After systematic correction.

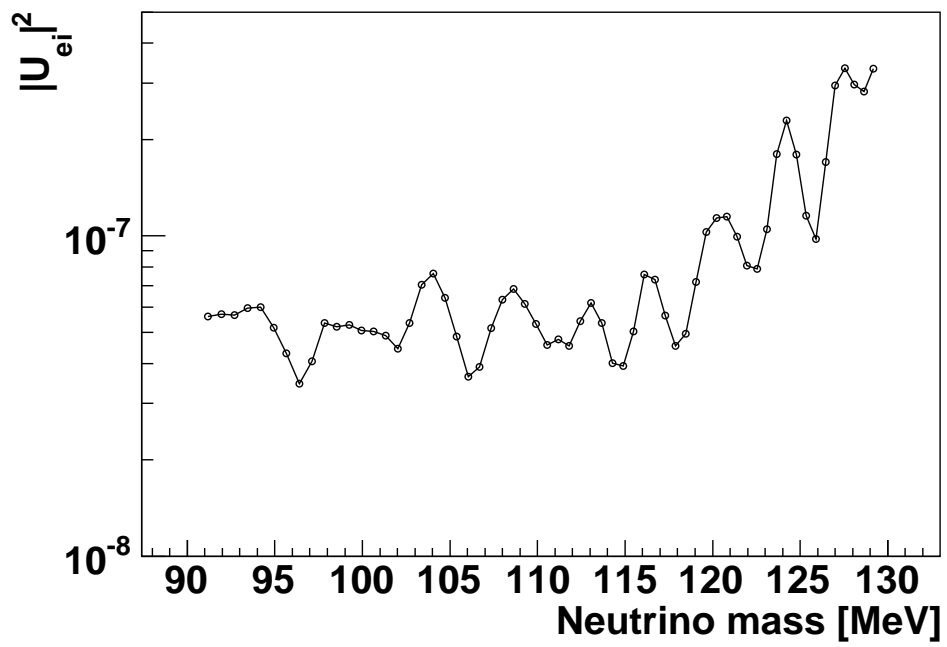


Figure 7.12: Upper limit (90% C.L.) of the mixing parameter  $|U_{ei}|^2$

## Chapter 8

# Discussions

The upper limits of  $|U_{ei}|^2$  of the massive neutrino in the mass region 90 MeV to 130 MeV are obtained in this thesis. Fig.8.1 shows the present result and the previous limit which is obtained with  $\pi^+ \rightarrow e^+\nu$  decay.[13]. The upper limits are about 1.4 times better in the mass region 90 MeV to 110 MeV and worse in the mass region 110 MeV to 130 MeV.

Basically the method of the PIENU experiment and the previous experiment is the same and the sensitivity to the massive neutrinos is linear with 'S' which is described below and also described in § 2.3.

$$S = \sqrt{N_{BG}}/N_{\pi \rightarrow e\nu_e} \quad (8.1)$$

The number of event of  $\pi^+ \rightarrow e^+\nu_e$  decay in Suppressed-Spectrum is 480k which is 4 times more than the previous experiment and the amount of the background compared to  $\pi \rightarrow e\nu_e$  decay is 6.8% which is 2.5 times smaller than the previous experiment. That is why the 'S' of Suppress-Spectrum become 3.16 times smaller than the previous experiment and it means the upper limit could become 3 time better than the previous result. However the obtained upper limits are not such good and there is 2 reason which can explain that the result is worse than expected. One is the systematic correction effect which is about 80% in the mass region 90 MeV to 110 MeV and about 50% in the mass region 110 MeV to 130 MeV. In the previous experiment, there is no systematic correction about energy dependent acceptance difference. It should have been done although there is no tracking cut and the correction is not as big as ours. The purple line in Fig.8.2 shows the upper limits without the systematic correction and it is better than previous limit in the mass region 110 MeV to 130 MeV. Another one is the way to evaluate the shape of the energy spectrum of several energy positron. In this thesis, the shape was obtained with Monte Carlo conservatively. On the other hand the shape is obtained just scale the shape of the spectrum of  $\pi^+ \rightarrow e^+\nu_e$  in the previous experiment. The way to scale the spectrum is following. The spectrum is supposed to consists from Gaussian and exponential low energy tail component and then the  $\sigma$  of the Gaussian is scaled with  $\sqrt{E}$  and the decay constant of exponential is scaled with  $1/E$ . This means the shape of the low energy tail is always the same and only Gaussian component is getting wider with decreasing the positron energy. This procedure to evaluate the spectrum shape is not consistent with the data which taken with beam positron in our experiment. The blue line in Fig.8.2 shows the upper limits with the spectrum shape obtained by the procedure of previous experiment (Pre-Method). The green line in Fig.8.2 shows the upper limits with the spectrum shape obtained by Pre-Method without systematic correction. The Green line is about 2 times better than previous limit. It is still worse than expected result but the fitting procedure is a bit different between the present work and previous experiment and it might cause the difference.

In the PIENU experiment will obtain 7 times more data and the sensitivity is expected to become about 2.5 times better. In this analysis the acceptance correction is estimated conservatively with about 10% and the positron spectrum shape is also estimated conservatively with about 10%. If the accuracy of these estimation become better the upper limits can be 20% better. And in order to search the mass region 50 MeV to 90 MeV which corresponds to 40 MeV to 60 MeV in positron energy, the shape of low energy tail of  $\pi^+ \rightarrow e^+ \nu_e$  is needed to be understood.

The upper limits of  $|U_{ei}|^2$  obtained in this thesis is not smaller than the limits from the neutrino less double- $\beta$  decay experiment. However the limit is meaningful because the neutrino less double- $\beta$  decay is sensitive only to Majorana neutrinos.

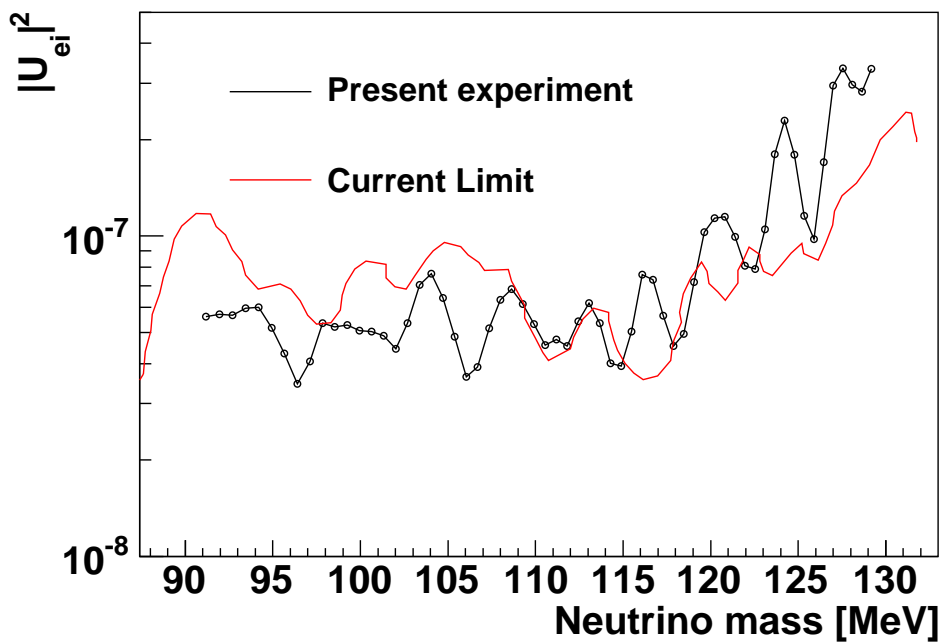


Figure 8.1: Upper limit (90% C.L.) of the mixing parameter  $|U_{ei}|^2$ . Black line shows the present result. Red line shows the previous limit.

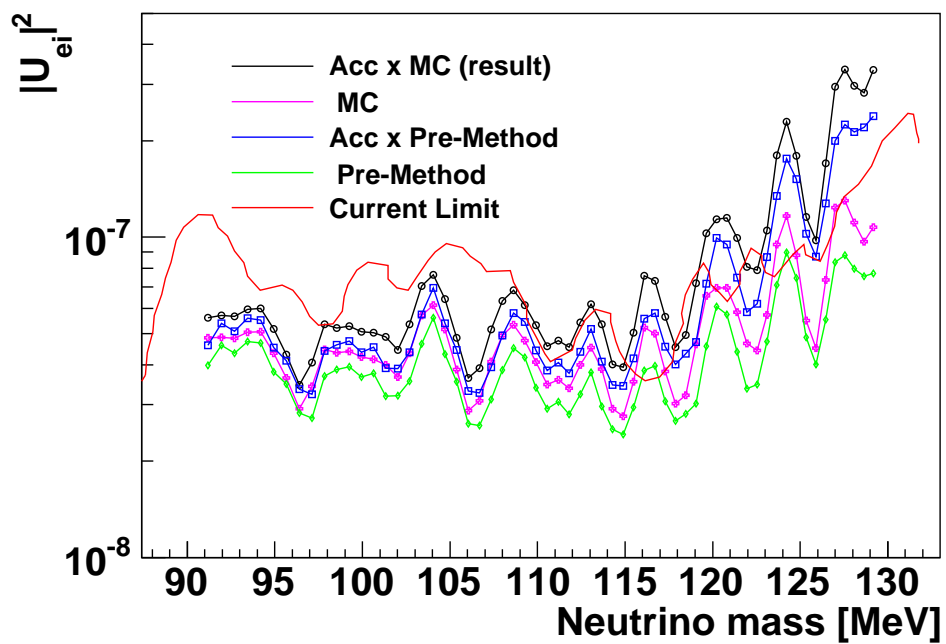


Figure 8.2: Upper limit (90% C.L.) of the mixing parameter  $|U_{ei}|^2$ . Black line shows the present result. Purple line show the upper limit without acceptance correction. Blue line show the upper limit with previous experiment method with acceptance correction. Green line show the upper limit with previous experiment method. Red line shows the previous limit.



## Chapter 9

# Conclusion

In order to search massive neutrinos in  $\pi^+ \rightarrow e^+\nu$  decay and measure the branching ratio  $R = \Gamma(\pi^+ \rightarrow e^+\nu_e[\gamma])/\Gamma(\pi^+ \rightarrow \mu^+\nu_\mu[\gamma])$ , The PIENU experiment have been performed at TRIUMF. Data taking was started in May 2009, and the data were taken till December 2009 (RUN-I and RUN-II). The data taking will continue till end of 2011 and in total about 7M  $\pi^+ \rightarrow e^+\nu_e$  event data will be obtained. In this thesis massive neutrino search is performed by searching an additional peak in the positron energy spectrum of  $\pi^+ \rightarrow e^+\nu_e$  decay. RUN-I data which has 1 M  $\pi^+ \rightarrow e^+\nu_e$  events is used for the analysis.

First, the positron energy spectrum of  $\pi^+ \rightarrow e^+\nu$  decay is obtained. The positron energy is measure by the NaI calorimeter and the  $\pi^+ \rightarrow \mu^+ \rightarrow e^+$  events are suppressed by using the timing information, the energy deposit information in the target, tracking information and waveform information of the target PMT signal. The amount of the background is 6.8% compared to  $\pi^+ \rightarrow e^+\nu_e$  decay.

Then neutrino search in the mass region 90 MeV to 130 MeV is done by fitting the positron energy spectrum. The fit is done by changing the positron energy with 0.5 MeV step. In order to fit the spectrum, the background distribution is assumed with exponential function and the energy spectrum shape of the positron from the decay with massive neutrinos are obtained by the Monte Carlo simulation. and the validity of the Monte Carlo is confirmed with the data. The probability of the fitting are enough good and there is no evidence of the existence of the massive neutrino and raw upper limits of  $\Gamma(\pi \rightarrow e\nu_i)\Gamma(\pi \rightarrow e\nu_e)$  is evaluated.

Then systematic correction to the raw upper limits is done and the upper limits (90% C.L.) of mixing parameter of massive neutrino  $|U_{ei}|^2$  are evaluated in the mass region 90 MeV to 130 MeV. The upper limits are about  $5 \times 10^{-4}$ (90%C.L) in the mass region 90 MeV to 110 MeV and  $1 \times 10^{-4}$ (90%C.L) in the mass region 110 MeV to 130 MeV.

The upper limits are 1.5 times better than current world record with  $\pi^+ \rightarrow e^+\nu_e$  in the mass region 90 MeV to 110 MeV. The PIENU experiment will obtained 7 times more data and the results are expected to be improved.



# Bibliography

- [1] W. Pauli, *Letter to the Physical Society of Tübingen* (1930), unpublished, the letter is reproduced in Brown, L.M. (1978), *Physics Today*, **31**, No. 9, 23.
- [2] F. Reines and C. L. Cowan, Jr., *Phys. Rev.* **92**, 830 (1953)
- [3] G. Danby *et al.*, *Phys. Rev. Lett.* **9**, 36 (1962).
- [4] K. Kodama *et al.* (DONUT Collaboration), *Phys. Lett.* **B504**, 218 (2001).
- [5] J. Steinberger, *Phys. Rep.* **203**, 345 (1991).
- [6] Particle Data Group <http://pdg.lbl.gov/>
- [7] R.N. Mohapatra *et al.*, arXiv:hep-ph/0510213v2.
- [8] A. Atre *et al.*, *JHEP* 05:030 (2009).
- [9] T. Appelquist and R. Shrock. *Phys. Lett. B* **548**, 204 (2002).
- [10] V. Cirigliano and I. Rosell, arXiv:0707.3439; *J. High Energy Phys.* 10 (2007) 005.
- [11] D.I. Britton *et al.*, *Phys. Rev. Lett.* **68**, 3000 (1992).
- [12] G. Czapek *et al.*, *Phys. Rev. Lett.* **70**, 17 (1993).
- [13] D.I. Britton *et al.*, *Phys. Rev. D.* **46**, R885 (1992).
- [14] Ch. Kraus *et al.*, *Eur. Phys. J. C* **40**, 447-468 (2005).
- [15] A. Aguliar-Arevalo *et al.*, *Nucl. Instrum. Meth A* **609**, 102-105 (2009).
- [16] Y. Igarashi *et al.* , A Common Data Acquisition System for High-Intensity Beam Experiments, *IEEE TNS VOL. 52,NO. 6, DECEMBER 2005*
- [17] K. Yamada *et al.* , Pion Decay-Mode Tagging in a Plastic Scintillator Using COPPER 5000-MHz FADC, *IEEE TNS VOL. 54,NO. 4, AUGUST 2007*
- [18] VF48 manual  
[http://daq-plone.triumf.ca/HR/VME/VF48/VF48%20-%20Reference%20v2.1.1\\_0c.pdf/view](http://daq-plone.triumf.ca/HR/VME/VF48/VF48%20-%20Reference%20v2.1.1_0c.pdf/view)
- [19] VT48 manual  
[http://daq-plone.triumf.ca/HR/VME/Triumf/TDC48\\_revA\\_block.pdf/view](http://daq-plone.triumf.ca/HR/VME/Triumf/TDC48_revA_block.pdf/view)
- [20] AMT-3 homepage  
<http://atlas.kek.jp/tdc/amt3/index.html>
- [21] MIDAS Home Page <http://ladd00.triumf.ca/~daqweb/doc/midas/html/>